



Technical University of Munich  
Department of Physics

MAX-PLANCK-INSTITUT  
FÜR PHYSIK



Max-Planck-Institute for Physics

Master's Thesis in Nuclear, Particle and Astrophysics

---

# Electron Backscattering on Silicon Drift Detectors and Its Impact on a Sterile Neutrino Search with KATRIN

---

Elektronenrückstreuung an Silizium-Drift-Detektoren und ihr Einfluss auf die Suche nach Sterilen Neutrinos mit KATRIN

Author: Daniela Spreng  
Submission Date: 01 March 2023

Primary reviewer: Prof. Dr. rer. nat. Susanne Mertens  
Secondary reviewer: Prof. Dr. rer. nat. Stefan Schönert  
Supervisor: Korbinian Urban, Anthony Onillon

# Acknowledgement

I want to thank everybody who supported me during my master's thesis, especially:

**Prof. Dr. Susanne Mertens** I want to thank you for the great opportunity to work with you and your excellent team. I am very grateful for your support and your guidance ever since my bachelor's thesis.

**Korbinian Urban** I want to tell you that you are a great supervisor. You could always help me with any problem, be it electronics, geometries or data analysis. Furthermore, I want to congratulate you to your very powerful electron gun without which my work would not have been possible.

**Christoph Wiesinger** I want to thank you for your very comprehensive help with Geant4 and especially for your patience with debugging my code.

**Frank Edzards** Thank you for your very pedantic feedback on my master's thesis, which not only improved my work but also my writing style in general. I promise to always keep an eye on my 'gets' and remove them as good as possible from my future works.

**Daniel Siegmann** Thank you for always answering my questions and keeping an eye on my mental health. I am also very grateful for your outstanding work with the module production which made this thesis possible in the first place.

**Christina Bruch** I want to thank you for your mental support throughout our whole studies. You are a dear friend and a great colleague. Thank you for always taking time for me to solve my mind blockages. Moreover, thank you that you helped me out with your arms to explain electron trajectories and scattering angles.

**Christian Forstner** Thank you for your help with computers and for always keeping me up to date with good papers, cheat sheets or helpful links.

**TRISTAN group** Thank you for welcoming me into your team and always helping me with advice and action.

**My Family** I want to thank you for making it possible for me to study. I am very grateful for your support, financially and emotionally.



# Contents

<b>1</b>	<b>Introduction</b>	<b>1</b>
<b>2</b>	<b>Neutrino Physics</b>	<b>3</b>
2.1	The Discovery of Neutrinos and their Properties . . . . .	3
2.2	Neutrino Oscillations and Neutrino Mass . . . . .	5
2.3	Sterile Neutrinos . . . . .	9
<b>3</b>	<b>The KATRIN Experiment</b>	<b>11</b>
<b>4</b>	<b>The TRISTAN Detector</b>	<b>15</b>
4.1	Detector Requirements and Design . . . . .	16
4.2	SDD Working Principle . . . . .	17
4.3	Detector Response to Electrons . . . . .	19
4.4	Backscattering and Backreflection in the KATRIN Experiment . . . . .	23
<b>5</b>	<b>The BERTA Experiment</b>	<b>25</b>
5.1	Experimental Setup . . . . .	25
5.1.1	Setup Components and Geometry . . . . .	25
5.1.2	Readout-Chain . . . . .	30
5.2	Measurements and Settings . . . . .	32
5.3	Data Analysis . . . . .	34
5.3.1	Iron Calibration . . . . .	34
5.3.2	Charge Sharing . . . . .	36
5.3.3	Pileup . . . . .	38
5.3.4	Incoming Electron Number Reconstruction . . . . .	39
5.3.5	Coincidence . . . . .	40
5.4	Experimental Results . . . . .	42
5.4.1	All Events . . . . .	42
5.4.2	Coincidence Events . . . . .	47
5.5	Summary . . . . .	57

---

<b>6</b>	<b>BERTA Simulation with Geant4</b>	<b>59</b>
6.1	Simulation Setup . . . . .	59
6.2	Simulation Settings . . . . .	61
6.3	Data Processing . . . . .	62
6.3.1	Comparability of Simulations and Measurements . . . . .	62
6.3.2	Heuristic Detector Model . . . . .	63
6.4	Simulation Results . . . . .	70
6.5	Summary . . . . .	75
<b>7</b>	<b>Comparison of Experiment and Simulation</b>	<b>77</b>
7.1	Uncertainty Estimation . . . . .	77
7.2	Energy Spectra . . . . .	79
7.3	Angular Distribution . . . . .	83
7.4	Backscattering Coefficients . . . . .	86
7.5	Summary . . . . .	89
<b>8</b>	<b>Conclusion and Outlook</b>	<b>91</b>
<b>A</b>	<b>Appendix</b>	<b>93</b>
A.1	Geant4 Physics List Comparison . . . . .	93
A.2	Heuristic Detector Model - Additional Fit Results . . . . .	95
A.3	Comparison of Experiment and Simulation - Additional Results . . . . .	97
	<b>List of Figures</b>	<b>99</b>
	<b>List of Tables</b>	<b>103</b>
	<b>Bibliography</b>	<b>105</b>

# Introduction

Sterile neutrinos are a natural extension of the Standard Model of Particle Physics. These particles could explain several open questions in cosmology and astrophysics. With a mass in the order of keV, they would constitute a viable Dark Matter candidate. The aim of the TRISTAN project is the development of a novel detector system for the KATRIN experiment to search for sterile neutrinos on the keV-mass scale in the entire tritium beta-decay spectrum. The TRISTAN detector will use a monolithic multi-pixel Silicon Drift Detector (SDD) system to probe the sterile neutrino parameter space up to energies of 18.6 keV and mixing angles of  $\sin^2 \Theta < 10^{-6}$ . SDDs have an excellent energy resolution of about 300 eV (FWHM) at 20 keV and are able to handle 100 kcps/pixel.

To search for sterile neutrinos in tritium beta-decay, the detector response to electrons has to be precisely understood. In this context, one major effect to be considered is detector backscattering. Electrons that backscatter from the silicon surface only deposit part of their energy and thus influence the shape of the energy spectrum. The probability for backscattering depends on the initial energy and incident angle of the electrons. An additional effect to be considered in the KATRIN experiment is backreflection. Due to the presence of electromagnetic fields, backscattered electrons can be reflected back to the SDD depending on their energy and angle. As a result, to precisely model the detector response to electrons in the KATRIN beamline, the relations between the energies and angles of the initial electrons and the backscattered electrons have to be precisely understood.

One major goal of this thesis is to study the effect of detector backscattering in detail. To this end, an experimental setup with two TRISTAN detectors was developed: One 7-pixel SDD was used as an active target, whereas the other detector, a 166-pixel SDD array, served as a backscattering detector. To extract information on backscattered electrons, a coincidence analysis between both detectors was performed. A backscattering probability of about 17% for an initial electron energy of 10 keV and an incident angle of  $0^\circ$  was observed, which is in good agreement with the theoretical expectation.

The second main goal of this thesis is the development of a GEANT4 Monte Carlo simulation of the backscattering process. In a first step, detector parameters such as the entrance window thickness were inferred via a fit of the simulation to the experimental data. In a next step, the backscattering characteristics were compared to the measured data. Here, an excellent agreement between the simulated and the measured energy and angular distributions of backscattered electrons at different initial energies and angles was obtained. Furthermore, the simulated backscattering coefficients are in agreement with the experimental backscattering coefficients. In total, it was proven that the GEANT4

simulations are suitable for the investigation of backscattering in the TRISTAN detector. The results obtained in the scope of this thesis are of major importance for a sterile neutrino search with KATRIN. They impart key inputs for the final model describing the full tritium spectrum including the detector response to electrons. In particular, this work provides for the first time an experimentally verified description of the impact of backscattering on the detector response.

# Neutrino Physics

One of the most abundant particles in the universe are neutrinos. They are electrically neutral fermions (spin-1/2) and come in three different flavours  $\nu_e$ ,  $\nu_\mu$  and  $\nu_\tau$ . They were named after their charged leptonic partners to which they couple in charged current weak interactions: The electron  $e$ , muon  $\mu$  and tauon  $\tau$ . Due to their lack of electrical or color charge they interact solely via the weak interaction or gravity. Furthermore, in contrast to the other fermions they have no right-handed partners. In the Standard Model (SM) of Particle Physics they are hence introduced as massless.

Section 2.1 will give an overview of the neutrino, starting with its postulation and discovery in the beginning of the 20th century. Furthermore, the fundamental properties of neutrinos, focusing on neutrino oscillations and how they lead to the requirement of a non-zero neutrino mass, will be described in section 2.2. In addition, the possibility of the existence of a right-handed neutrino, the so-called sterile neutrino, will be discussed in section 2.3. Especially sterile neutrinos in the keV-mass range, which constitute suitable Dark Matter (DM) candidates, are of interest in the scope of this work.

## 2.1 The Discovery of Neutrinos and their Properties

In 1914, the detection of the nuclear  $\beta$ -decay by J. Chadwick and other researchers represented a great riddle [1]. They anticipated to measure a two-body decay of a nucleus into a lighter daughter nucleus and an electron and hence expected the electron to be mono-energetic. In contrast to their expectations, they detected a continuous electron energy spectrum ranging from zero kinetic energy up to the maximum allowed energy  $Q$ . In 1930, W. Pauli postulated the existence of another non-observed particle which was emitted in the decay in order to preserve energy conservation [2]. This particle would have to be neutral to conserve electric charge, very light since the maximal observed electron energy  $E_{e,max} \approx Q$  and have spin-1/2 to satisfy angular momentum conservation. When  $Z$  denotes the atomic number and  $A$  the mass number of the nucleus, the resulting reaction is:

$$(Z, A) \rightarrow (Z + 1, A) + e^- + \bar{\nu}_e. \quad (2.1)$$

In 1956, this "ghost" particle was finally discovered in the project Poltergeist by F. Reines and C. Cowan who used the nuclear reactor at Savannah River in South Carolina as an electron anti-neutrino source [3]. They placed a detector consisting of water with dissolved cadmium chloride between layers of scintillating material next to the power plant. In the

scintillator, a positron  $e^+$  and a neutron  $n$  were produced via inverse  $\beta$ -decay:

$$\bar{\nu}_e + p \rightarrow e^+ + n. \quad (2.2)$$

With photomultipliers they observed a coincidence between the signal of the annihilation of the positron and a photon emitted in the de-excitation of cadmium after neutron capture with a delay of 200 ns.

In 1962, L. Lederman, M. Schwarz and J. Steinberger were able to prove at the Alternating Gradient Synchrotron (AGS) in Brookhaven that there is not only one type of neutrino [4]. They directed a 15 GeV proton beam onto a beryllium target to produce a beam of pions which then decayed into neutrinos. Only neutrinos could pass through the steel shield installed in front of a spark chamber. In the detector, only

$$\nu_\mu + N \rightarrow \mu^- + X \quad (2.3)$$

but almost no

$$\nu_e + N \rightarrow e^- + X \quad (2.4)$$

interactions were found, demonstrating that electron and muon neutrinos are different particles.

**Three Generations  
of Matter (Fermions) spin ½**

	I	II	III
mass →	2.4 MeV	1.27 GeV	171.2 GeV
charge →	$\frac{2}{3}$	$\frac{2}{3}$	$\frac{2}{3}$
name →	Left <b>u</b> Right up	Left <b>c</b> Right charm	Left <b>t</b> Right top
Quarks	4.8 MeV $-\frac{1}{3}$ Left <b>d</b> Right down	104 MeV $-\frac{1}{3}$ Left <b>s</b> Right strange	4.2 GeV $-\frac{1}{3}$ Left <b>b</b> Right bottom
	0 eV 0 Left <b><math>\nu_e</math></b> Right electron neutrino	0 eV 0 Left <b><math>\nu_\mu</math></b> Right muon neutrino	0 eV 0 Left <b><math>\nu_\tau</math></b> Right tau neutrino
	0.511 MeV -1 Left <b>e</b> Right electron	105.7 MeV -1 Left <b><math>\mu</math></b> Right muon	1.777 GeV -1 Left <b><math>\tau</math></b> Right tau
Leptons			

**Figure 2.1: Standard Model of Particle Physics.** The six quarks (purple) and leptons (green), separated in charged and uncharged leptons with three flavours each, are presented with their properties. Every particle exists with left- and right-handed chirality except the neutrino. It is introduced in the Standard Model as solely left-handed and massless. Figure adapted from [5].

In 2001, after the discovery of the tau lepton in 1975, the Direct Observation of Nu Tau (DONUT) experiment at Fermilab could show that there exists even a third type of neutrino [6]. The number of active neutrinos was constrained to  $N_\nu = 2.9840 \pm 0.0082$  [7] by measurements of the invisible decay width of the Z-boson at the Large Electron-Positron (LEP) Collider at CERN. Therefore, with the detection of the tau neutrino all three active neutrino flavours were discovered. Furthermore, the Goldhaber experiment showed that neutrinos only come with left-handed helicity (spin parallel to momentum) while anti-neutrinos are right-handed (spin anti-parallel to momentum) [8].

The SM arranges all known fermions via their corresponding quantum numbers and is depicted in fig. 2.1. In it, the neutrino takes its place as electrically neutral fermion coming in three flavours without right-handed partners. Nevertheless, the neutrino plays a special role as it is the only particle solely interacting via the weak interaction. In addition, since mass generation via Yukawa coupling with the Higgs field is not allowed without right-handed partner, the neutrino was introduced as massless in the SM.

## 2.2 Neutrino Oscillations and Neutrino Mass

Since the 60's, the Homestake experiment led by Raymond Davis Jr. detected solar neutrinos. Surprisingly, the observed neutrino flux was smaller than predicted by John N. Bahcall with the Standard Solar Model [9]. The result was confirmed by the GALLEX [10], SAGE [11] and Borexino [12] experiments, forming the so-called solar neutrino problem. Later, the Sudbury Neutrino Observatory (SNO) experiment was able to not only detect electron neutrinos through charged current interactions with deuterium  $d$

$$\nu_e + d \rightarrow p + p + e^- \quad (2.5)$$

but also all other flavours by neutral current interactions

$$\nu_\alpha + d \rightarrow p + n + \nu_\alpha, \quad \alpha = e, \mu, \tau. \quad (2.6)$$

By comparing the neutrino fluxes of the different flavours, SNO demonstrated that the solar neutrino flux only consists of one third of electron neutrinos at the studied energies. The total flux observed by SNO was in accordance with the theoretical predictions [13]. Thus, the experiment confirmed the disappearance of electron neutrinos and validated that they are replaced by muon and tau neutrinos.

The concept of neutrino oscillations was introduced to explain the results of the SNO experiment. It describes the phenomenon that the three flavour eigenstates ( $\nu_e, \nu_\mu, \nu_\tau$ ) are a superposition of three mass eigenstates ( $\nu_1, \nu_2, \nu_3$ ). The mixing can be described by the unitary Pontecorvo-Maki-Nakagawa-Sakata (PMNS) matrix  $U_{\text{PMNS}}$  as indicated in the following equation:

$$\underbrace{\begin{pmatrix} \nu_e \\ \nu_\mu \\ \nu_\tau \end{pmatrix}}_{\text{flavour eigenstates}} = \underbrace{\begin{pmatrix} U_{e1} & U_{e2} & U_{e3} \\ U_{\mu1} & U_{\mu2} & U_{\mu3} \\ U_{\tau1} & U_{\tau2} & U_{\tau3} \end{pmatrix}}_{\text{PMNS matrix}} \underbrace{\begin{pmatrix} \nu_1 \\ \nu_2 \\ \nu_3 \end{pmatrix}}_{\text{mass eigenstates}} \quad (2.7)$$

It can be parameterised in terms of three mixing angles ( $\Theta_{12}$ ,  $\Theta_{13}$  and  $\Theta_{23}$ ) and one physical phase (Dirac phase  $\delta$ ) if neutrinos are Dirac particles, which can cause CP violation. If neutrinos are Majorana particles, there are two additional phases ( $\alpha_1$ ,  $\alpha_2$ ). The resulting PMNS matrix is then:

$$U = \begin{pmatrix} 1 & 0 & 0 \\ 0 & c_{23} & s_{23} \\ 0 & -s_{23} & c_{23} \end{pmatrix} \begin{pmatrix} c_{13} & 0 & s_{13}e^{-i\delta} \\ 0 & 1 & 0 \\ -s_{13}e^{-i\delta} & 0 & c_{13} \end{pmatrix} \begin{pmatrix} c_{12} & s_{12} & 0 \\ -s_{12} & c_{12} & 0 \\ 0 & 0 & 1 \end{pmatrix} \begin{pmatrix} e^{i\alpha_1} & 0 & 0 \\ 0 & e^{i\alpha_2} & 0 \\ 0 & 0 & 1 \end{pmatrix} \quad (2.8)$$

with  $s_{ij} = \sin \Theta_{ij}$  and  $c_{ij} = \cos \Theta_{ij}$ .

Hence, neutrinos are produced and interact as flavour eigenstates but propagate as mass eigenstates. The probability to oscillate from a produced flavour eigenstate  $\alpha$  to the measured eigenstate  $\beta$  (simplified two-flavour case) can be calculated by the following equation [14]:

$$P_{\alpha \rightarrow \beta} = \sin^2(2\Theta) \cdot \sin^2\left(\frac{\Delta m^2}{4} \cdot \frac{L}{E}\right). \quad (2.9)$$

Here  $L$  is the travelled distance,  $E$  the energy of the neutrino,  $\Theta$  the mixing angle between the mass eigenstates and  $\Delta m^2$  the difference of the squared masses of the mass eigenstates. This equation can easily be adapted to all three neutrino flavours.

As can be deduced from equation 2.9, for neutrino oscillations to exist,  $\Delta m^2$  between two mass eigenstates must be larger than zero meaning that at least two neutrinos need to have non-zero mass. Observations of reactor, accelerator and atmospheric neutrinos confirmed neutrino oscillations [15–18]. Unfortunately, neither the absolute mass of the neutrinos nor the ordering of the mass eigenstates can be determined through neutrino oscillation experiments. The current best experimentally determined squared mass differences are [19]

$$\Delta m_{12}^2 = (5.43 \pm 0.18) \cdot 10^{-5} \text{eV}^2 \quad (2.10)$$

and

$$\Delta m_{23}^2 = (2.41 \pm 0.05) \cdot 10^{-3} \text{eV}^2. \quad (2.11)$$

The absolute mass of neutrinos must be several orders of magnitude smaller than the one of fermions as illustrated in fig. 2.2. To this date, no experiment has succeeded in performing a direct measurement of neutrino masses. In general, there are three experimental approaches to set an upper limit of the absolute neutrino mass: Cosmology, neutrinoless double  $\beta$ -decay and the kinematics of  $\beta$ -decay.

## Cosmology

Neutrinos were abundantly produced during the decoupling of the electroweak force after the Big Bang. Nowadays, the average number density of cosmological neutrinos is  $n_\nu \approx 336 \text{cm}^{-3}$  [19]. Since neutrinos do have a mass, they contribute to the cosmological matter density; but as their mass is so small, they were relativistic over a long period in the early universe. As a result, they contributed to gravitational wells for matter clustering on large scales but washed out small scale structures by carrying away matter. By measuring the structure of the universe through e.g. the cosmic microwave background, galaxy

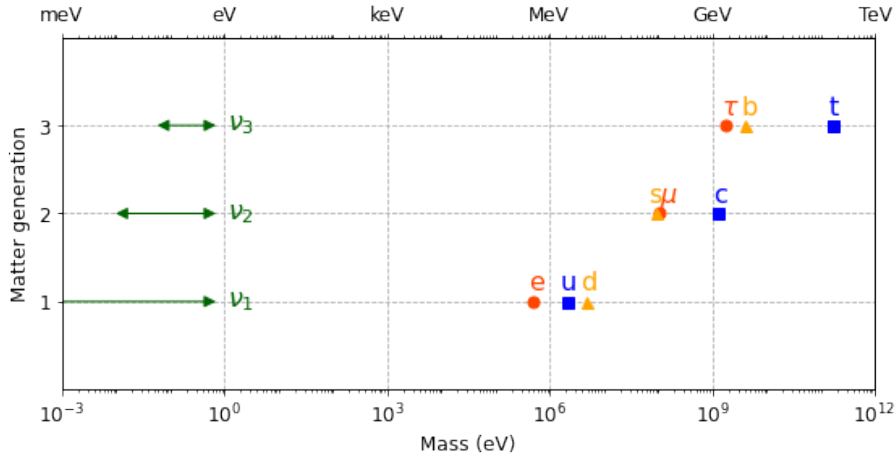


**Figure 2.2: Fermion Mass Ordering.** The masses of all fermions are shown, where for the neutrino mass a normal ordering ( $m_1 \ll m_2 < m_3$ ) is assumed. Clearly visible is the gap between the neutrinos and the other particles of more than five orders of magnitude. Plot adapted from [20].

surveys and the Lyman-alpha forest, the sum of the neutrino masses can be constrained. The most recent results by the Planck collaboration are [21]

$$m_\nu = \sum_i m_i < 0.12 - 0.54 \text{eV}, 95 \% \text{ C.L.} \quad (2.12)$$

Unfortunately, cosmological bounds are highly model-dependent and vary with the choice of included datasets.

### Neutrinoless Double $\beta$ -Decay

In nuclei where single  $\beta$ -decay is energetically forbidden, such as in  $^{48}\text{Ca}$ ,  $^{76}\text{Ge}$  and  $^{136}\text{Xe}$ , one can search for hypothetical neutrinoless double  $\beta$ -decay ( $0\nu\beta\beta$ ). In contrast to ordinary two-neutrino double  $\beta$ -decay ( $2\nu\beta\beta$ ), in  $0\nu\beta\beta$  two neutrons simultaneously decay into two protons and two electrons without neutrino emission. This process would violate lepton number conservation by two units. Hence, the detection of  $0\nu\beta\beta$  would decisively proof the Majorana nature of the neutrino, i.e. that it is its own antiparticle.

In experiments, the signature of this two-body decay is a mono-energetic peak at the kinematic endpoint of the corresponding continuous  $2\nu\beta\beta$  spectrum. The summed energy of the electrons equals the  $Q$ -value of the decay. The decay has not yet been observed and thus experiments can only set lower limits on the half-life  $T_{1/2}^{0\nu}$  of the decay. Since the half-life is correlated to the coherent superposition of the neutrino masses, one can set upper limits on the effective Majorana mass  $m_{\beta\beta}$  with

$$m_{\beta\beta}^2 = \left| \sum_i U_{ei}^2 m_i \right|^2. \quad (2.13)$$

The current best upper limits are provided by the KamLAND-Zen experiment with a decay half-life of  $T_{1/2}^{0\nu} > 2.3 \cdot 10^{26}$  y corresponding to an upper limit on the effective Majorana

mass of  $m_{\beta\beta} < 36 - 156 \text{ meV}$  [22]. Nonetheless, this approach can only provide a limit range since  $m_{\beta\beta}$  depends on the underlying calculation of the nuclear matrix element which has large theoretical uncertainties [23]. In addition, due to the complex phases  $U_{ei}$ ,  $m_{\beta\beta}$  can also cancel out in case of normal ordering which is extremely unlikely but would make an experimental observation impossible.

### $\beta$ -Decay Kinematics

The most model-independent method to probe the effective anti-neutrino mass  $m_\beta$  is the investigation of the continuous  $\beta$ -decay energy spectrum. For a non-zero effective mass of the electron anti-neutrino the endpoint of the spectrum shifts to lower energies. The maximal kinetic energy of the measured electron is the endpoint energy  $E_0$  minus  $m_\beta$ . Furthermore, the shape of the spectrum close to the endpoint changes due to the phase space factor in the Fermi theory which describes the decay. Both effects are shown for the example of tritium  $\beta$ -decay in fig. 2.3.

The resolution of former and current experiments at the endpoint is not high enough to resolve all three mass eigenstates. Therefore, they measure an effective neutrino mass which is the incoherent sum of the neutrino mass eigenstates:

$$m_\beta = \sqrt{\sum_i |U_{ei}|^2 m_i^2}. \quad (2.14)$$

In contrast to  $0\nu\beta\beta$ , this effective mass does not contain any CP-violating phases.

The current best upper limit on  $m_\beta$  is provided by the Karlsruhe Tritium Neutrino (KATRIN) experiment with  $m_\beta < 0.8 \text{ eV}$  at 90% C.L. [24]. It measures the electron energy spectrum of tritium  $\beta$ -decay. The basic concept of the KATRIN experiment will be explained in section 3.

Project 8 uses cyclotron radiation emission spectroscopy with an atomic tritium source to measure the electron energy spectrum to determine the effective electron anti-neutrino mass [25]. Other experiments as for example ECHO and HOLMES measure the electron capture spectrum of  $^{163}\text{Ho}$  to directly obtain the electron neutrino mass [26].

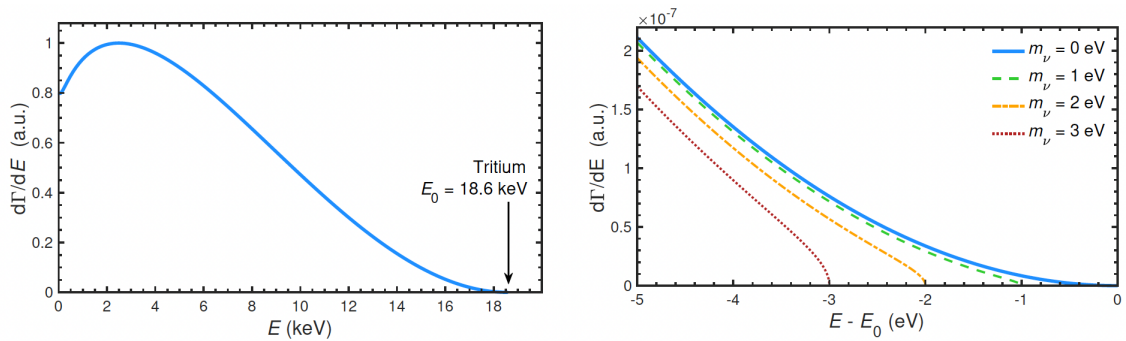


**Figure 2.3: Neutrino Mass Signature in the Tritium  $\beta$ -Decay Spectrum.** The tritium  $\beta$ -decay spectrum is shown on the left. In the zoom to the endpoint region on the right, the imprint of the effective electron anti-neutrino mass can be seen. The endpoint energy is shifted to lower energies and the spectral shape is changed close to the endpoint. The effect is shown for different effective masses. Plot taken from [27].

## 2.3 Sterile Neutrinos

In contrast to the other fermions, neutrinos do not have a right-handed partner within the SM. It therefore seems very natural to extend the SM with right-handed neutrinos and, as discussed in the following part, it is also very well-motivated. Since the weak interaction only couples to left-handed fermions, right-handed neutrinos would not interact via any SM interaction and are therefore often called sterile neutrinos  $\nu_s$ . Hence, the only possibility to search for sterile neutrinos is via their mixing with the active flavours through their mass eigenstate  $\nu_4$ :

$$\begin{pmatrix} \nu_e \\ \nu_\mu \\ \nu_\tau \\ \nu_s \end{pmatrix} = \begin{pmatrix} U_{e1} & U_{e2} & U_{e3} & U_{e4} \\ U_{\mu1} & U_{\mu2} & U_{\mu3} & U_{\mu4} \\ U_{\tau1} & U_{\tau2} & U_{\tau3} & U_{\tau4} \\ U_{s1} & U_s & U_{s3} & U_{s4} \end{pmatrix} \begin{pmatrix} \nu_1 \\ \nu_2 \\ \nu_3 \\ \nu_4 \end{pmatrix} \quad (2.15)$$

The introduction of sterile neutrinos could explain several open questions in cosmology and neutrino experiments depending on their mass, mixing angle and production mechanism. In principle they are not constrained to a certain mass range. Three mass scales are described below, each with its own scientific motivation.

### GeV-Mass Scale

The small scale of neutrino masses is often explained through a minimal type I seesaw mechanism [28]. For every Dirac neutrino mass term  $m_D$ , this model introduces an additional Majorana neutrino mass term  $m_R$  and hence assumes that neutrinos are Majorana particles. Diagonalising the resulting neutrino mass matrix for one generation leads to

$$m_1 \approx m_R \quad \text{and} \quad m_2 = \frac{m_D^2}{m_R} \quad (2.16)$$

with  $m_1$  and  $m_2$  being the physical neutrino masses. As a result, a heavy sterile neutrino with a mass in the order of GeV or more, could explain the very small active neutrino masses as the other mass eigenstate is inversely proportional to  $m_R$ .

A second motivation for GeV sterile neutrinos is that they can explain the generation of the baryon asymmetry in the early universe via leptogenesis [29]. Nevertheless, to be in agreement with the observed abundances of light elements in the universe the sterile neutrinos must have decayed before the Big Bang Nucleosynthesis (BBN). As a result, today, GeV sterile neutrinos could only be produced and searched for in accelerator experiments.

### keV-Mass Scale

Just as Weakly Interacting Massive Particles (WIMPs), axions and primordial black holes, sterile neutrinos in the keV-mass scale would constitute a good Dark Matter (DM) candidate. They are neutral, massive and their lifetime can be very long. Depending on their production mechanism, they would be either Warm (WDM) or Cold (CDM) Dark Matter. They could have been produced via oscillations at high temperatures in the early universe, but due to their low interaction strength they would not enter thermal equilibrium and thus have a very long lifetime in the order of the age of the universe.

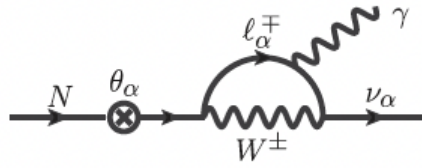


**Figure 2.4: Sterile Neutrino Two-Body Decay.** The sterile neutrino  $N$  decays via a loop into an active neutrino  $\nu_\alpha$  and a photon with energy  $E_\gamma = M_N/2$ . Figure adapted from [30].

Nonetheless, since they couple to active neutrinos, keV sterile neutrinos are not stable and could for example decay into a mono-energetic photon and an active neutrino as illustrated in fig. 2.4. A possible hint towards such a decay gave the X-ray Multi-Mirror (XMM)-Newton telescope which observed a mono-energetic X-ray line at 3.5 keV. In case of sterile neutrino decay this line would translate into a 7 keV sterile neutrino [31]. Other X-ray telescopes confirmed the detection of this line [32, 33]. Nevertheless, it could also originate from incomplete knowledge of all astrophysical lines and is still under discussion [31, 34].

The Tritium Investigations of Sterile to Active Neutrino mixing (TRISTAN) detector aims to probe the sterile neutrino parameter space up to 18.6 keV and mixing amplitudes of  $\sin^2 \Theta < 10^{-6}$  with the KATRIN experimental setup [35]. The TRISTAN detector will be explained in more detail in chapter 4.

### eV-Mass Scale

The existence of eV-scale sterile neutrinos is motivated by several experimental anomalies. The Gallium Experiment (GALLEX) [10] and the Soviet-American Gallium Experiment (SAGE) [36] detected a deficit of the expected neutrino flux in the radioactive source calibration [37]. Moreover, a significant lack of anti-neutrinos was observed in several short baseline reactor experiments [38, 39]. A way to directly search for sterile neutrinos on the eV-mass scale would be e.g. with the KATRIN experiment as their existence would lead to a kink-like distortion in the  $\beta$ -decay spectrum.

# The KATRIN Experiment

The Karlsruhe Tritium Neutrino experiment was designed to measure the effective electron anti-neutrino mass  $m_\beta$  in a mostly model-independent way by investigating the tritium  $\beta$ -decay energy spectrum close to its endpoint. Located at the Karlsruhe Institute of Technology (KIT) and partially hosted by the Tritium Laboratory Karlsruhe (TLK), it is the successor of the Mainz and Troitsk experiments which already succeeded to set an upper limit on  $m_\beta$  of 2.3 eV (95 % C.L.) and 2.05 eV (95 % C.L.), respectively [40, 41]. The KATRIN experiment aims to improve those upper limits and reach a sensitivity of 0.2 eV at 90 % C.L. after 3 years of effective measurement time [42]. If the neutrino mass is larger than 350 meV, a  $5\sigma$  discovery is possible [42]. The operation of the experiment started in 2016 with calibration sources. First measurements with tritium were taken in 2018 [43]. Already in 2019, after a measurement period of only four weeks, the previous upper limits for the neutrino mass could be improved by a factor of two to 1.1 eV (90 % C.L.) [44]. In 2021, a first upper limit in the sub-eV range of 0.8 eV at 90 % C.L. was found [24].

In the following, the experimental setup of the 70 m long KATRIN beamline, as depicted in fig. 3.1, will be explained with a focus on its two core elements, the Windowless Gaseous Tritium Source (WGTS) and the Magnetic Adiabatic Collimation combined with an Electrostatic (MAC-E) filter. If not stated otherwise, all given information are taken from the KATRIN design report [42].

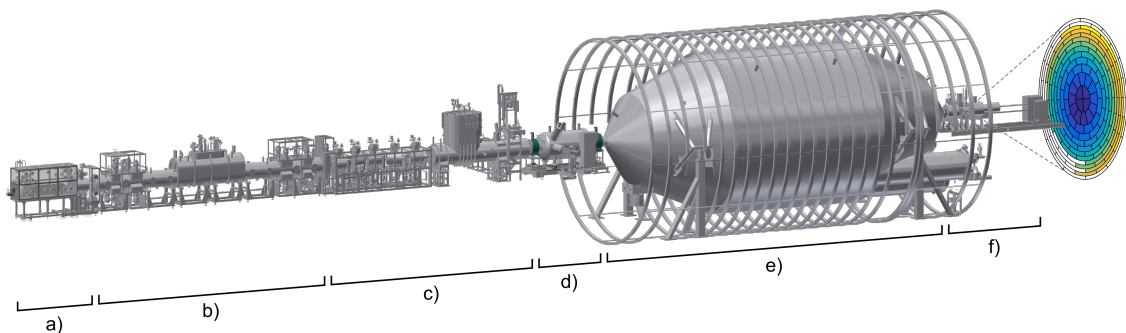


**Figure 3.1: Schematic of the KATRIN Experiment.** (a) Rear section, (b) Windowless Gaseous Tritium Source (WGTS), (c) Transport section, (d) Pre-spectrometer, (e) Main spectrometer, (f) Focal Plane Detector (FPD). Figure courtesy of the KATRIN collaboration.

### Rear Section

The rear section is located at the very beginning of the beamline and mainly consists of the rear wall and several diagnostic instruments. The rear wall is a 145 mm large stainless steel disk plated with gold. Nearly all electrons reflected in the spectrometers hit the rear wall where they recombine.

Two of the most important diagnostic tools are a mono-energetic, angular selective electron gun and a Beta-Induced X-ray Spectroscopy (BIXS) system. The electron gun is used to monitor the tritium source properties like the gas density and investigate electron transmission properties. The BIXS system consists of two silicon drift detectors which measure the X-ray spectrum from  $\beta$ -decay electrons hitting the rear wall and producing bremsstrahlung. Therefore, it is able to monitor the source activity.

### Windowless Gaseous Tritium Source

The KATRIN experiment uses molecular tritium  $T_2$  as a  $\beta$ -decay electron source



which has several advantages. Its short half-life of 12.6 years and its very low  $Q$ -value of 18.6 keV provide the needed statistics at the endpoint region of the spectrum. In addition, its simple electronic shell and molecular configuration allows a very precise correction of the interaction between the emitted electron and the daughter nucleus. Moreover, being a super-allowed decay, an energy correction of the nuclear matrix element is unnecessary since it is energy-independent.

The gaseous molecular tritium is continuously injected in the center of a 10 m long and 9 cm broad tube. During the diffusion to both sides of the tube, where it is pumped out with turbomolecular pumps, the tritium decays. About 40 g/d of tritium are circulated and held at a purity of more than 95 %. A very stable high activity of  $10^{11}$  Bq ( $\pm 0.1$  %) is achieved. Superconducting magnets then guide the  $\beta$ -decay electrons towards the transport section. To mitigate electron energy loss, the tritium source is windowless.

### Transport Section

One has to prevent the tritium from entering the spectrometer and detector section as it would contribute to the background. Therefore, the transport section is arranged in chicanes to have no direct line of sight of the tritium source with the detector. It is divided in two sections, the Differential Pumping Section (DPS) and the Cryogenic Pumping Section (CPS). In the DPS, the tritium atoms are pumped out by multiple Turbo Molecular Pumps (TMPs), whereby in the CPS they are trapped on the inner surface of the gold-plated beam tube wall which is covered by an argon frost layer. The electrons are magnetically guided through the transport section. The tritium ions are further blocked by ring and dipole electrodes. As a result, with this combination of techniques the tritium flux is reduced by more than 14 orders of magnitude.

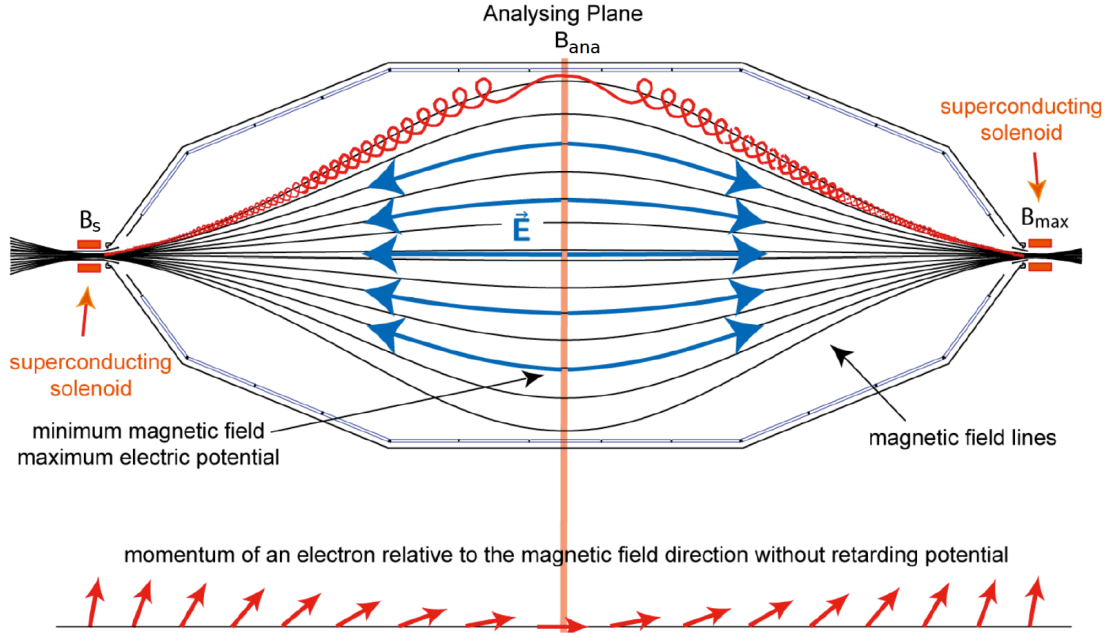


**Figure 3.2: MAC-E Filter Principle.** The electrons (red line) from the tritium source enter the spectrometer and follow the magnetic field lines (black lines) defined by two superconducting solenoids. Through the decreasing magnetic field strength towards the analysis plane (orange line), the transversal component of the electron energy is converted into a longitudinal one due to conservation of the electrons orbital magnetic momentum in an adiabatic motion. As indicated by the red arrows in the bottom, the transversal momentum component is minimal in the analysis plane where the electrons are filtered by the applied retarding potential (blue arrows). Scheme adapted from [45].

### Spectrometer Section

The spectrometer section consists of two parts, the Pre-Spectrometer (PS) and the Main Spectrometer (MS). Both filter electrons according to their energy based on the MAC-E filter principle and are connected to 1 m-long superconducting magnets. The filter principle is depicted in fig. 3.2.

The electrons coming from the transport section enter the MAC-E filter where they follow the inhomogeneous magnetic field generated by two superconducting solenoids at the entrance and at the exit. To filter the electrons by energy, a negative electrical potential, called retarding potential  $U$ , is applied. It acts like a high-pass filter, where electrons can only overcome the potential and reach the detector if their longitudinal energies are larger than  $U \cdot e$ , with  $e$  being the elementary charge. As a consequence, the residual transversal energy  $E_{\perp}$  of the electron defines the energy resolution of the filter. The electron's orbital magnetic moment

$$\mu \approx \frac{E_{\perp}}{B} \quad (3.2)$$

is conserved in adiabatic motion. Hence, the transversal momentum component is transformed into a longitudinal one when the electron travels from the strong magnetic field  $B_{\max}$  at the entrance of the MAC-E filter to the minimal field  $B_{\text{ana}}$  in the analysis plane. There-

fore, the transversal energy is smallest in the plane with the maximal retarding potential where the electrons are filtered. As a result, the energy resolution  $\Delta E$  is defined by:

$$\frac{\Delta E}{E} = \frac{B_{\text{ana}}}{B_{\text{max}}}. \quad (3.3)$$

With  $B_{\text{max}} = 6 \text{ T}$  and  $B_{\text{ana}} = 3 \cdot 10^{-4} \text{ T}$ , the main spectrometer is designed to achieve an energy resolution of  $0.93 \text{ eV}$  for electron energies near the endpoint.

Since scattering processes should be avoided, electrons which travelled a long distance through the source are reflected by the magnetic mirror effect due to their large angles. To this end,  $B_{\text{max}}$  is deployed right after the source leading to a maximal acceptance angle of

$$\Theta_{\text{max}} = \arcsin \sqrt{\frac{B_{\text{S}}}{B_{\text{max}}}} \approx 51^\circ \quad (3.4)$$

for  $B_{\text{S}} = 3.6 \text{ T}$  and  $B_{\text{max}} = 6 \text{ T}$ . Here,  $B_{\text{S}}$  denotes the magnetic field within the source. At last, the earth's magnetic field is compensated by a complex system of air coils surrounding the spectrometer.

The main purpose of the PS is to be a first potential barrier to reduce the number of electrons entering the main spectrometer to lower the background due to scattering processes. Nevertheless, the PS will be switched off from the end of the fourth measurement phase as both spectrometers build a Penning trap between them [46].

In the MS, the filtered electrons are re-accelerated after the analysis plane and then focused onto the detector with an increased magnetic field  $B_{\text{det}}$ . As a result, by varying the retarding potential, one can record an integral spectrum by counting the electrons passing the filter and reaching the detector.

### Focal Plane Detector

The Focal Plane Detector (FPD) is located at the exit of the main spectrometer and counts the electrons passing the MAC-E filter. It consists of a silicon p-i-n (positive-intrinsic-negative) diode array of 148 pixels arranged in a ring-wise structure. Through this pixel placement radial and azimuthal effects can be investigated. Each pixel has the same area of  $44 \text{ mm}^2$  to equally distribute the count rate. The maximum count rate that the detector system can handle is in the order of tens of kcps. Since the detector is designed to only count electrons, it has a rather poor energy resolution of about  $1.5 \text{ keV FWHM}$  at  $18.6 \text{ keV}$  per pixel. To lower the intrinsic detector background in the region of interest and to reduce backscattering, a post-acceleration of usually  $U_{\text{PAE}} = 10 \text{ kV}$  is applied [47].

# The TRISTAN Detector

Like the known mass eigenstates of the neutrino, also a hypothetical fourth mass eigenstate would lead to a distortion of the  $\beta$ -decay spectrum. In contrast to the active neutrino masses, the mass difference of a keV-scale state would be resolvable and would lead to a kink and a broad distortion of the spectrum. The resulting spectrum would then be the superposition of an active neutrino and a sterile neutrino part, see fig. 4.1. The shape and weighting depends on the mixing angle  $\Theta_S$  and the effective electron anti-neutrino mass  $m_\beta$  as well as the mass of the fourth mass eigenstate  $m_4$ :

$$\frac{d\Gamma}{dE} = \underbrace{\cos^2 \Theta_S \frac{d\Gamma(m_\beta)}{dE}}_{\text{Active neutrino part}} + \underbrace{\sin^2 \Theta_S \frac{d\Gamma(m_4)}{dE}}_{\text{Sterile neutrino part}} \quad (4.1)$$

With the first tritium data taken during the commissioning run of the KATRIN experiment in 2018, the KATRIN experiment was able to set an exclusion limit on the sterile-to-active mixing amplitude  $\sin^2 \Theta < 5 \cdot 10^{-4}$  (95 % C.L.) for sterile neutrinos with a mass up to 1.6 keV [48]. This result improved the existing laboratory-based bounds in the mass range of 0.1–1.0 keV. The Tritium Investigations of Sterile to Active Neutrino mixing project

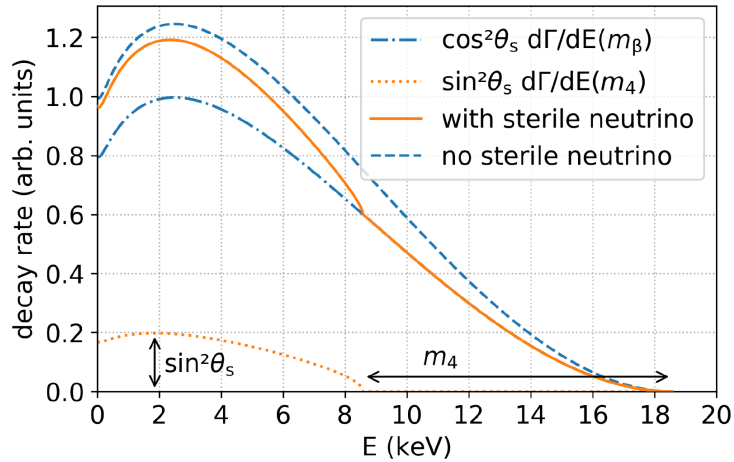


**Figure 4.1: Sterile Neutrino Signature in the Tritium  $\beta$ -Decay Spectrum.** Here, a mass of  $m_4 = 10$  keV and a mixing angle of  $\sin^2 \Theta_S = 0.2$  is assumed. The latter is unphysically high but emphasises the kink-like signature. The blue dash-dotted line and the orange dotted line show the contribution of the active and sterile neutrino, respectively. The dashed line shows the spectrum in case no sterile neutrino exists. Plot taken from [49].

develops a new detector to replace the current FPD in the KATRIN beamline to probe the sterile neutrino parameter space up to 18.6 keV and mixing angles of  $\sin^2 \Theta_S < 10^{-6}$  [35].

The detector requirements as well as the detector design will be presented in section 4.1. The working principle of the Silicon Drift Detector (SDD) technology which is used for the TRISTAN detector as well as the detector response to electrons is described in the sections 4.2 and 4.3. In section 4.4, the impact of backscattering on the electron spectrum is discussed.

## 4.1 Detector Requirements and Design

Besides an integral mode like in the currently ongoing neutrino mass measurements at the KATRIN experiment, the TRISTAN detector will be operated also in a differential mode. Here, either none or a low retarding potential is applied to the main spectrometer. The detector will not only have to count the electrons but also determine their energy. As a result, the detector has to fulfill higher spectroscopic requirements than the current detector in KATRIN.

The kink-link signature of a sterile neutrino could be located several keV away from the endpoint of the tritium spectrum. In addition, the amplitude of the signal distortion directly scales with the mixing angle  $\sin^2 \Theta_S$  which is expected to be very low at the < ppm-level. Therefore, two main features of the detector are crucial to resolve the spectral distortion:

1. The possibility to handle high count rates: Due to a lowered retarding potential, the new detector has to handle total rates of up to  $10^8$  cps over three years to reach the needed low statistical uncertainty for a ppm sensitivity [50]. Therefore, the high rate will be distributed among thousands of pixels to minimise the pileup probability. To process such a huge amount of information, a high-performance readout electronics is necessary. It needs to have a high ADC sampling rate (100 MHz) and resolution (14-16 bit) to create real-time spectra, detect pileup events and correlate simultaneous energy depositions in neighbouring pixels [51]. Therefore, the TRISTAN project also includes the development of a dedicated readout chain and Data Acquisition System (DAQ) [50, 52, 53].
2. An excellent energy resolution: An excellent energy resolution of about 300 eV Full Width at Half Maximum (FWHM) at 20 keV is required to resolve the kink-like structure [50]. Hence, the detector needs to have a low-noise performance. Furthermore, electrons lose their energy continuously when travelling through matter. Therefore, a good charge collection efficiency and thin entrance window have to be achieved in the detector.

SDDs, whose working principle is explained in section 4.2, are proven to be very suited in both respects. The TRISTAN detector will therefore consist of modular SDD pixel arrays. A pixel size of about 3 mm in diameter has been chosen to minimise the effects of charge sharing and pixel change after backscattering and backreflection [54]. The pixels

are 450  $\mu\text{m}$ -thick hexagonal cells arranged in a honeycomb structure with a continuous entrance window to minimise the dead area. Each module consists of a detector chip hosting 166 pixels glued on top of a special ceramic material called CeSiC, two front-end electronics boards and a copper support and cooling structure. To reduce electronic noise, the detector modules are cooled to a temperature of about  $-40^\circ\text{C}$  [50].

The commissioning of the TRISTAN detector system follows a staged approach. The goal of phase 0 is the integration of one TRISTAN module in the KATRIN Monitor Spectrometer and its characterisation with electrons. This phase was successfully completed in the second half of 2022 and first measurement results can be found in [55] and [56]. Phase 1 is planned for the end of 2024 with the integration of nine TRISTAN modules (see fig. 4.2) in the KATRIN beamline. It requires the decommissioning of the existing FPD and the installation of the new TRISTAN detector and DAQ system. The final TRISTAN detector will consist of 21 modules (see fig. 4.2). The final TRISTAN design will be realised in phase 2 with a renewed and optimised electromagnetic design.

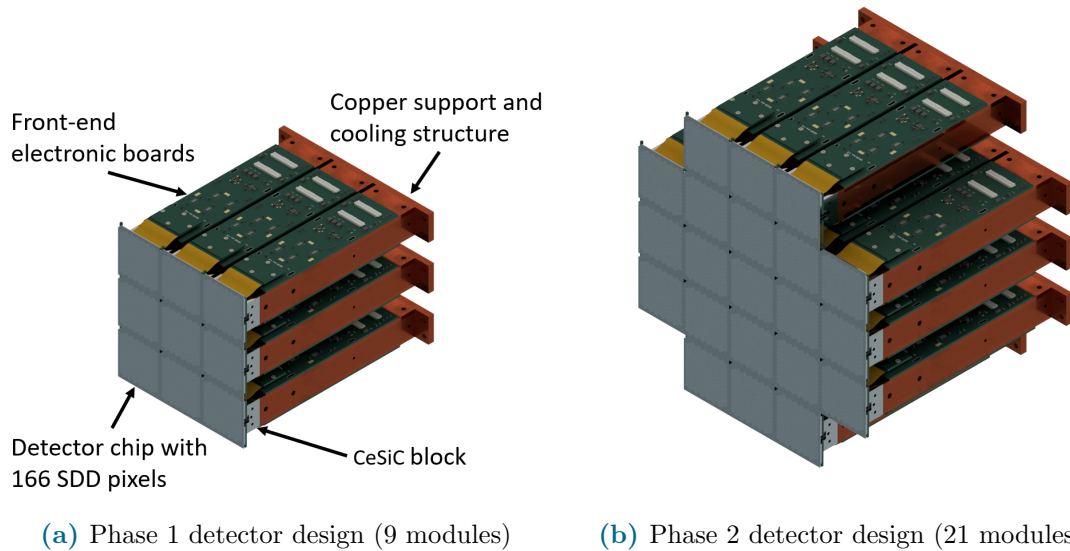


**Figure 4.2: TRISTAN Detector Design.** Each module consists of a detector chip with 166 SDD pixels (grey) glued onto a CeSiC block (light grey), which is mounted on copper blocks (orange) with two front-end electronic boards (green) on either side.

## 4.2 SDD Working Principle

SDDs are a special type of semiconductor detectors. They have a very low-noise performance due to a small anode capacitance and are characterised by a fast and effective charge collection. Therefore, they are able to detect X-rays as well as electrons at high count rates with an excellent energy resolution using the depleted volume of a silicon pn-junction. A sketch of the SDD structure is shown in fig. 4.3.

Crystalline silicon has a four-valent structure. Through the introduction of impurities in the intrinsic material (doping) its electrical properties can be modulated. At the interface

of a n-doped region, usually doped with phosphorus (5 valence electrons), and a p-doped region, usually doped with boron (3 valence electrons), a depleted area is formed. The free electrons of the n-type silicon move to the p-type region and recombine. A space charge region is build up until the resulting electric field stops the electron exchange. Inside the depletion zone no free charged particles are present any more. By applying a high enough voltage  $U_{\text{bias}}$  to the SDD the depleted area can be extended over the entire detector volume [57, 58].

The TRISTAN SDD pixel is similar to a semiconductor PIN (positive-intrinsic-negative) diode. The entrance window side (back contact) is made of  $p^+$ -doped silicon. On the opposite side of the detector, i.e. on the readout side, a small  $n^+$ -doped ring anode is placed in the centre. The depleted area forms the active detection area. If an ionising particle enters the depleted region, it creates electron-hole pairs. In the case of silicon, the average energy  $E_{\text{pair}}$  necessary for the creation of electron-hole pairs is  $E_{\text{pair}} \approx 3.65 \text{ eV}$  [59]. The number of produced charge carriers is proportional to the energy of the incoming particle.

Due to the electric field, the electrons and holes cannot recombine. They move out of the depleted region. In contrast to ordinary PIN diodes, the electrons are guided towards the very small anode by an electric field created by  $p^+$ -doped drift rings surrounding the anode. In this manner, all electrons generated in the depleted volume can be collected at the anode. The drift time depends on the distance between the anode and the interaction point of the incoming particle. The anode was designed to be very small in size which results in a small anode capacitance allowing for low noise and high rate operation of the SDD [60].

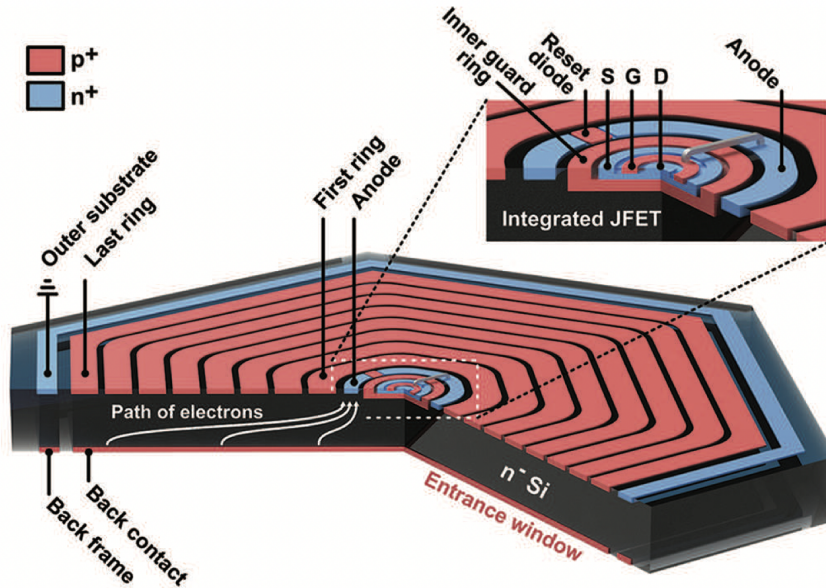


**Figure 4.3: SDD Working Scheme.** The small  $n^+$ -doped anode and the integrated FET are colored in blue. Shown in red are the back contact and the drift rings, both  $p^+$ -doped. Here, + and - indicate a high and low doping concentration. The exemplary path of the free charge carriers generated by an incoming particle is visualised as white trajectories. Figure taken from [61].

For the TRISTAN detector, a Field Effect Transistor (FET) has been integrated into the anode of each SDD pixel. It works as pre-amplifier sensitive to the charge collected at the anode and converting it to a voltage output. The smaller the capacitance of the detector, the higher the voltage change for a fixed amount of charge collected. The capacitance is minimised through this anode-FET combination due to avoiding conventional wire bonding solutions, hence ensuring maximal energy resolution [62].

The SDDs for the TRISTAN detector are designed and fabricated by the semiconductor laboratory of the Max-Planck-Society (MPG-HLL).

### 4.3 Detector Response to Electrons

In contrast to photons, which interact point-like, electrons lose their energy continuously while travelling through matter. Therefore, incomplete charge collection is much more likely for electrons compared to photons. Since the entire tritium spectrum has to be understood to a ppm level for a sterile neutrino search, a precise understanding of the detector response is imperative. The detector response of the TRISTAN SDD to mono-energetic electrons is shown in fig. 4.4. In the following, the spectral features will be discussed in more detail.

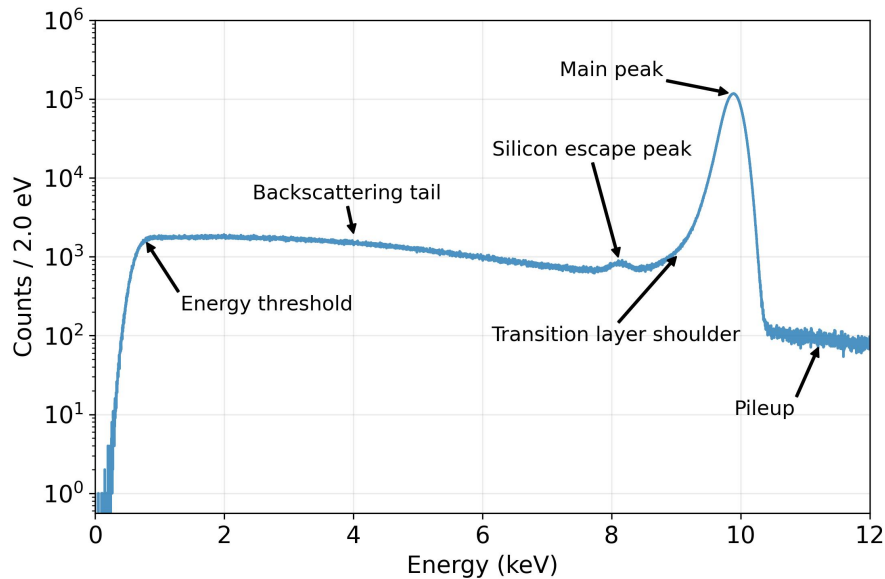


**Figure 4.4: Response of the TRISTAN Detector to Electrons.** The main peak of a 10 keV mono-energetic electron beam is slightly shifted to lower energies due to incomplete charge collection near the entrance window. The same effect leads to a transition layer shoulder at the low-energetic side of the peak. Photons emitted subsequent to electron ionisation may leave the detector leading to a silicon escape peak. Electrons being scattered-back towards the entrance window and leaving the detector lead to a backscattering tail. The detection threshold represents the border at which the detector is no longer able to distinguish between noise and a physics event. Pileup further alters the spectrum inter alia leading to counts above the actual electron energy.

### Main Peak

The variance of the determined energy of an incoming particle, and thus the energy resolution of the detection system, depends on statistical fluctuations in the charge production process, on the electronic noise of the signal readout chain and the charge collection efficiency in the detector.

Statistical fluctuations in the number of charge carriers created by the incoming particle are unavoidable and energy-dependent. They set a limit on the energy resolution for semiconductor detectors. This limit is defined by the material-dependent Fano factor  $F$ , the average energy  $E_{\text{pair}}$  necessary to create an electron-hole pair and the energy  $E$  of the incoming particle:

$$\sigma_{\text{Fano}} = \sqrt{F \cdot E_{\text{pair}} \cdot E}. \quad (4.2)$$

$F$  is slightly temperature- and energy-dependent. For the used SDDs within this work  $F$  is set to 0.117 [59] and  $E_{\text{pair}}$  to 3.65 eV [59].

The electronic noise is dependent on the capacitance and temperature of the detector as well as on the amplification and energy reconstruction of the read-out chain. Its contribution to the energy resolution can be described by an energy-independent constant  $c_{\text{el}}$ , hence:

$$\sigma_{\text{Fano+Noise}} = \sqrt{F \cdot E_{\text{pair}} \cdot E + c_{\text{el}}^2}. \quad (4.3)$$

As a result, for complete charge collection, the irradiation of the detector with mono-energetic ionising particles leads to a Gaussian peak at the initial energy  $E$  and with a width  $\sigma$ . For an ideal Gaussian peak, the energy resolution is expressed as the Full Width at Half Maximum (FWHM) of the distribution:

$$\text{FWHM} = 2\sqrt{2 \log 2} \cdot \sigma. \quad (4.4)$$

For photons, this definition is applicable. For electrons, the FWHM has to be extracted numerically. For them, incomplete charge collection due to the entrance window of the detector is much more pronounced. It leads to a distortion of the distribution towards lower energies and degrades the energy resolution. This effect will be explained further in the following paragraph.

### Transition Layer Shoulder

Incomplete charge collection is one of the most critical effects. Here, the detected events appear at lower energies compared to the actual energy of the incoming particle, resulting in a peak shift for mono-energetic sources and a reduced energy resolution. The entrance window forms a region of incomplete charge collection due to two contributions:

1. A well-defined silicon dioxide ( $\text{SiO}_2$ ) layer is added on the SDDs such that it cannot grow naturally. Hence, the detector is protected from further oxidation and can be manufactured with a controlled homogeneous layer with a thickness of 8-10 nm [57]. In this layer, any energy deposition is not detected.
2. The doping profile reaches several tens of nanometers into the detector bulk [49]. In this area close to the detector surface, not all electric field lines end up at the

detector anode. The created electrons may not drift to the anode but recombine with the holes instead. Hence, none or only a small fraction of the deposited energy is registered at the anode.

Due to their continuous energy deposition in materials, electrons are more affected by transition layer effects than point-like interacting photons. The mean free path of low-energetic electrons is smaller than the one of high-energetic electrons. Consequently, low-energetic electrons interact more often close to the surface. As a result, the transition layer effects are more pronounced at low energies.

The Charge Collection Efficiency (CCE) is difficult to predict and has to be determined via measurements. In the scope of this work, the following model is assumed:

$$\text{CCE}(z; DL, p_1, \lambda) = \begin{cases} 0 & z < DL \\ 1 + (p_1 - 1) \cdot \exp\left(-\frac{z-DL}{\lambda}\right) & z > DL \end{cases} \quad (4.5)$$

The CCE depends on the distance  $z$  of energy deposition relative to the detector surface. The detector is assumed to be completely insensitive in a dead layer of thickness  $DL$ . Hence, no charge deposited in this layer is collected by the anode. The higher the penetration depth, the higher is the charge collection efficiency. It is described by an exponential defined by the effective transition layer thickness  $\lambda$  and the detector efficiency after the dead layer  $p_1$ . This model has already been proven to be very successful in transition layer investigations of the TRISTAN SDDs [63].

In addition to worsening the energy resolution, the transition layer also introduces a detection threshold. This further reduces the information on backscattered electrons and charge sharing events in the detector. A closer investigation of the entrance window with electrons and the impact of the transition layer on the sterile neutrino sensitivity can be found in [64].

### Silicon Escape Peak

The incident radiation can ionise a shell electron of an atom in the detector material. The created hole will be filled by an inner shell electron from an outer shell, emitting a photon with an energy corresponding to the difference between the energy levels of the shells. The most prominent X-ray emission in silicon arises from the  $K_\alpha$  transition [65]. Here, a photon of 1.74 keV [65] is emitted, which can either be reabsorbed by the detector or leave it leading to an energy peak at 1.74 keV below the initial radiation energy. The escape peak amplitude depends on various parameters like the type and energy of the incident radiation, the ionisation probability and the detector geometry. In a measurement with tritium, which features a continuous electron energy spectrum, the superposition of the silicon escape peaks leads to a second tritium spectrum with smaller amplitude and endpoint energy.

### Charge Sharing

Electrons which enter the detector at or close to the border of two or more adjacent pixels lead to charge sharing. In an area of several tens of  $\mu\text{m}$  around the pixel border, the created charge is split and drifts to the respective pixel anode. The sum of the detected event

energies sums up to the initial electron energy. The effect is energy-dependent as high-energetic particles create larger charge clouds. In the TRISTAN detector design, charge sharing between up to three neighbouring pixels is possible. Within this work, charge sharing at the intersection of three pixels is neglected. Overall, charge sharing leads to a low-energy tail of the Gaussian peak and hence decreases the energy resolution. [66]

### Backscattering Tail

Backscattered electrons are another form of incomplete charge collection and have a substantial impact on the detected spectrum. Due to scattering processes, the electron undergoes a random change in its movement direction. As a result, the electron can be scattered back towards the entrance window and eventually leave the detector again. Some electrons do not even enter the sensitive volume but are reflected directly at the detector surface or scattered back in the insensitive  $\text{SiO}_2$  layer. Electrons that are reflected at the detector surface and that keep almost their entire energy are often referred to as elastic backscattering electrons, leaving no signal inside the detector. An inelastic backscattering continuum is produced by electrons entering the sensitive detection region, eventually producing secondary electrons and leaving the detector again. Moreover, the produced secondary electrons can leave the detector through scattering processes as well. In either case, the energy of the backscattered electrons is lost leading to a considerable backscattering tail over the entire electron spectrum.

Backscattering is often quantified by the backscattering coefficient  $\eta$ , which is defined as the ratio between the incoming and outgoing number of electrons:

$$\eta = \frac{N_{\text{out}}}{N_{\text{in}}}. \quad (4.6)$$

$\eta$  highly depends on the initial energy  $E_I$  and incident angle  $\Theta_I$  (see fig. 4.5) of the electrons. In general,  $\eta$  slightly decreases for higher initial energies due to a higher penetration depth. In contrast,  $\eta$  highly increases for higher incident angles. Here, the electrons interact more closely to the detector surface leading to a higher probability of the electron to escape from the detector material.

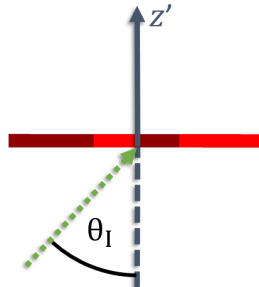


**Figure 4.5: Definition of the Incident Angle  $\Theta_I$ .**  $\Theta_I$  is the angle between the incoming electron beam (green arrow) and the  $z'$ -axis (grey arrow). The  $z'$ -axis is defined as the axis running perpendicular to the SDD (red) surface through its center.

## 4.4 Backscattering and Backreflection in the KATRIN Experiment

### Backscattering

In the KATRIN experiment, the electrons hit the detector with different incident angles and with a continuous energy spectrum. Very high incident angles, and thus very high backscattering coefficients, are mitigated by setting a maximal acceptance angle for electrons leaving the WGTS using the source and pinch magnets. Nonetheless, the incident angle still varies in the range  $0-51^\circ$  for the magnetic field configuration described in chapter 3. Furthermore, the backscattering tail is completely superimposed on the tritium  $\beta$ -decay energy spectrum. First investigations showed that the application of a post-acceleration potential after the MAC-E filter is very successful at shifting the imprint of backscattering electrons out of the region of interest [67]. An additional advantage is that at higher energies the total backscattering probability is lower.

### Backreflection

In the KATRIN beamline, there will also be the effect of detector backreflection. Depending on the energy  $E_{BS}$  and the angle  $\Theta_{BS}$  of the backscattered electrons, they can be reflected either by the magnetic fields of the detector magnet and the pinch magnet or by the electric fields of the post-acceleration potential and the retarding potential, see fig. 4.6. The latter only becomes important if it is set to a voltage higher than the post-acceleration. In the case of the search for sterile neutrinos with the TRISTAN detector in the differential mode, it does not play a major role as it will be either switched off or set to a very low voltage. As a result, only electrons with  $E_{BS}$  larger than the post-acceleration potential can escape from the detector section. Whether the backscattered electrons are reflected by the magnetic fields, depends on their  $\Theta_{BS}$ . As a rule of thumb, only electrons with small  $\Theta_{BS}$  and high  $E_{BS}$  can escape from the detector section [67].

The energy and angle of the backscattered electron also define if the backreflected electron is counted as an additional event or if it hits the same pixel again within a short time period leading to a single recorded event [67]. In the first case, the backreflected electron can also hit another pixel of the detector. In the second case, the detected electron energy will be the sum of both charge depositions. In either case, if the electron is not transmitted back to the WGTS, the energies of the backscattered electrons are not lost, but the spectral shape is highly altered by this combination of backscattering and backreflection.

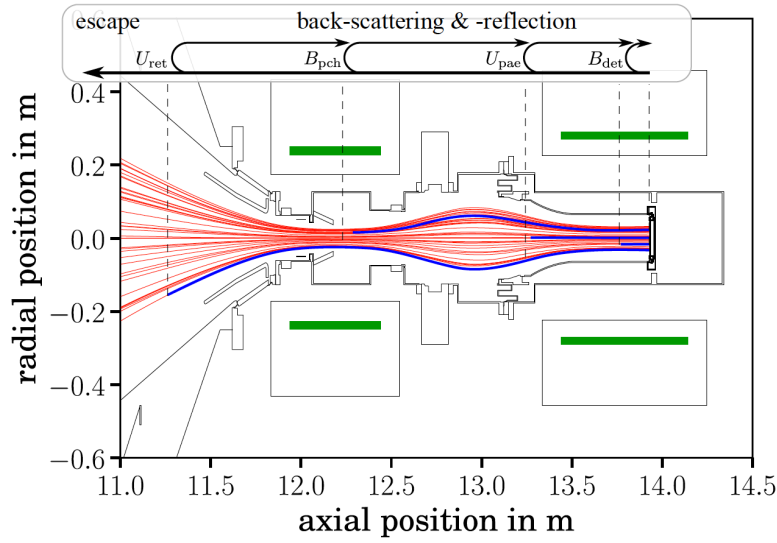


**Figure 4.6: Backscattering and Backreflection in the KATRIN Beamline.**  $\beta$ -decay electrons from the WGTS (situated on the left side of the plot) are depicted in red while backscattered electrons from the detector are colored in blue. The electrons can be either reflected by the magnetic fields of the detector, the pinch magnet, the electric post-acceleration or the retarding potential. For small angles and high energies, backscattered electrons also have the chance to escape the fields and travel back to the WGTS. Figure taken from [54].

So far, backscattering and backreflection have not yet been included in the sensitivity studies of the TRISTAN detector. To be able to fully model the tritium spectrum, the exact energy and angle dependencies of backscattered electrons have to be known. So far, only few experimental data on backscattering are available [68–70]. Hence, in the scope of this work an experimental setup with two types of TRISTAN detectors was developed. It is called the Backscattering Electrons Relations Testing Apparatus (BERTA) and its goal is to probe the relations of all four backscattering parameters: The incident angle  $\Theta_I$  (in literature often referred to as  $\alpha$ ), the initial electron energy  $E_I$ , the backscattering angle  $\Theta_{BS}$  and the backscattered energy  $E_{BS}$ . The experimental setup and the measurement results are presented in chapter 5. Since any experimental apparatus can only cover a limited parameter space, the second main goal of this thesis was the development of a dedicated Monte Carlo simulation using the GEANT4 toolkit, see chapter 6. To validate the applicability of the simulation, its results are compared to the experimental results in chapter 7.

# The BERTA Experiment

Preceding this work, simulations of electron backscattering in silicon detectors for the original KATRIN and the new TRISTAN detector were performed with KASSIOPEIA [54, 71]. KASSIOPEIA is a modular particle tracking framework which was developed to track multi-keV energy electrons for KATRIN. In addition, first steps were taken to perform sterile neutrino sensitivity studies of the TRISTAN detector with the GEANT4 simulation toolkit. In the scope of this work, an experimental setup was developed to specifically probe backscattering of electrons in and also with TRISTAN SDDs. The experimental results pose the opportunity to verify already existing as well as future simulations of electron backscattering for the modelling of the TRISTAN detector response.

The BERTA experiment was designed to probe the energy  $E_{BS}$  and angle  $\Theta_{BS}$  of electrons being backscattered of a SDD depending on their initial energy  $E_I$  and incident angle  $\Theta_I$ . Section 5.1 addresses the experimental setup, explaining all components, the electronic readout-chain and DAQ system. An overview of all measurement settings are given in section 5.2. The analysis steps, considering energy calibration, charge sharing, pileup, reconstruction of the number of incoming electrons and coincidence, are explained in section 5.3. At last, the results of the backscattering measurements are presented in section 5.4.

## 5.1 Experimental Setup

In this section the experimental setup is explained. All setup components and their arrangement are described in subsection 5.1.1, while the electronic readout-chain and the DAQ system is outlined in subsection 5.1.2.

### 5.1.1 Setup Components and Geometry

For the measurement of electron backscattering, two detectors are used: A 7-pixel prototype detector (Prod. nr. S0-7-6) in a flat design as an active target (fig. 5.3) and a 166-pixel 3D module (Prod. nr. S0-166-2) as a backscattering detector (fig. 5.4). A custom-made electron gun (fig. 5.2) is directed at the 7-pixel detector (shoot-on detector SOD). The 166-pixel module (backscattering detector BSD) is pointed at the SOD to observe backscattered electrons. Both detectors are fixated on copper holding structures and placed on the cooling plate of a cylindrical vacuum chamber. The geometry of the setup can be seen in fig. 5.1.

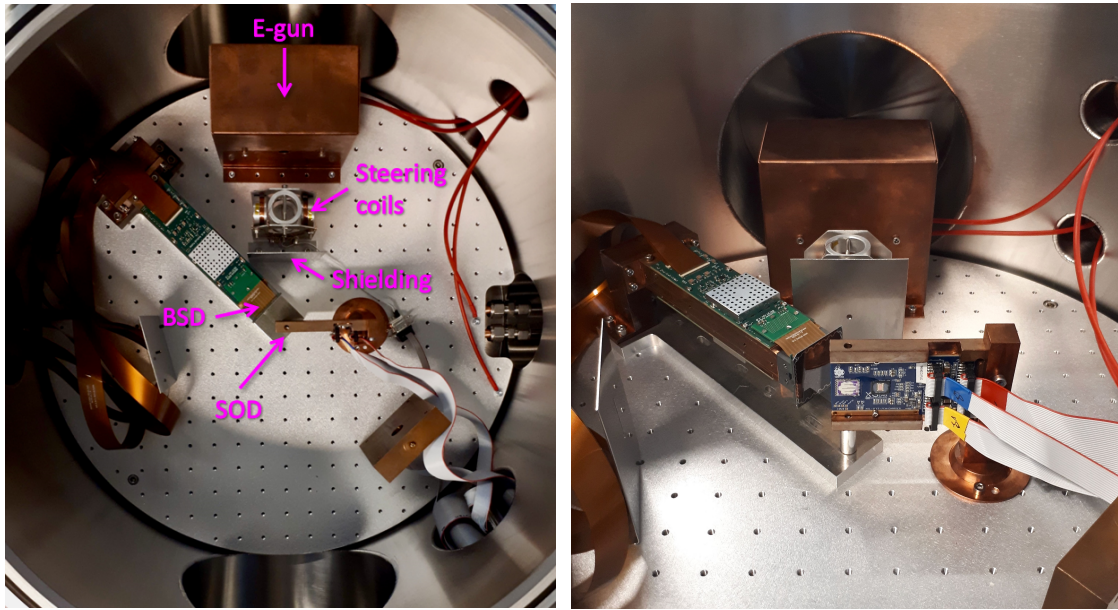


**Figure 5.1: In-Vacuum Setup.** The left picture is showing the top view, while the right picture shows the front view of the setup inside the vacuum chamber. The electron gun is situated inside a copper box and directed towards the SOD. The BSD is pointed at the SOD. Steering coils are placed in front of the electron gun. A thin shield with a small hole has been inserted between the steering coils and the SOD. The whole setup is mounted onto a cooling plate.

A good vacuum is needed since electrons have a very small free streaming length in air. In the setup, electrons have to travel several centimeters and stay undisturbed to reconstruct the correct electron path. A gas pressure in the order of  $10^{-6}$  to  $10^{-7}$  mbar is reachable through a turbo-molecular vacuum pump directly connected to the chamber.

The electron gun consists of a heated 0.025 mm thin tantalum wire. By applying a voltage, the electrons thermal energy eventually exceed the work function of the material, which is the minimal energy needed to remove an electron from a solid. The work function of tantalum is 4.25 eV [72]. The electron rate can be set in a range of 1 – 10 kcps by adjusting the wire temperature. For this, the voltage applied to the wire is controllable. A rate stability of around 10 – 30 % over several hours was achieved.

The tantalum filament is fixated between two gold wires and placed inside a pot-like structure integrated in a stainless steel plate. The glowing wire is arranged out of direct line of sight with the detector. It avoids photons, which are inevitable emitted, to exit the electron gun in the direction of the detector. An electric field is applied to the stainless steel plate to accelerate the electrons towards the SOD. Electric fields of 0 – 20 kV can be reached via a high voltage supply outside the vacuum chamber. The electron gun is fixated in a box-like copper shielding to define the electric field lines and to mount it on the cooling plate. Ceramic insulators electrically insulate the electron gun from the surrounding copper structure. The electron gun design can be seen in fig. 5.2.

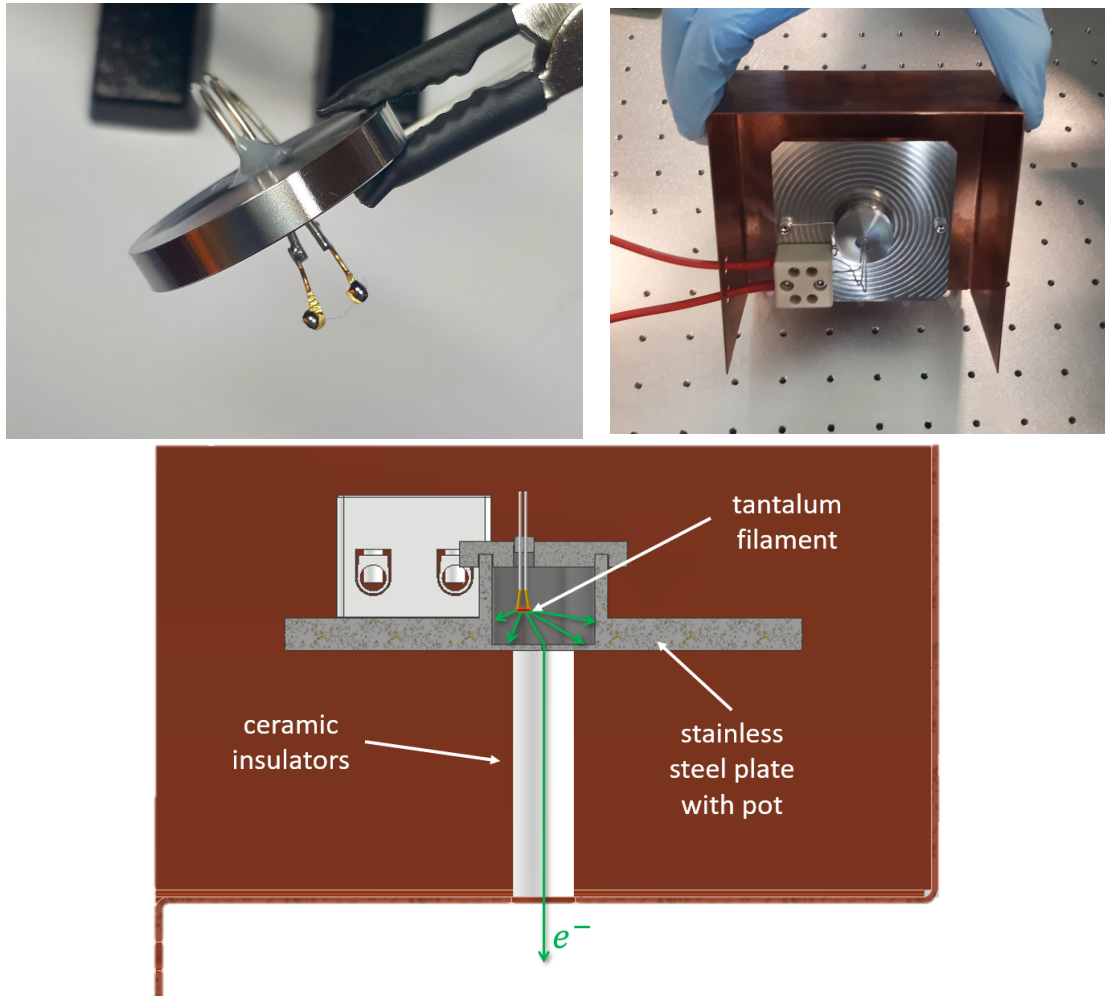


**Figure 5.2: Electron Gun Design.** Upper left: The stainless steel lid is shown with the thin tantalum filament fixated between two gold wires. Upper right: The backside view of the electron gun is depicted. The stainless steel plate inside the copper box is visible. The backside and the bottom of the copper shielding is open. Lower center: The lateral cross-section of the electron gun and its surrounding copper box is illustrated. The tantalum filament is placed off-center in the pot integrated in the stainless steel plate. The electrons (green arrows) emitted from the tantalum filament exit the pot through a small hole towards the SOD.

The resulting mono-energetic electron beam is directed on the central pixel of the SOD. Fig. 5.3 shows the PCB board which holds the 7-pixel SDD chip and the readout electronics. To probe different incident angles between the electron beam and the SOD, the copper holding structure is rotatable around an axis parallel to the center of the chip surface. Any angle between  $0^\circ$  and  $60^\circ$  can be chosen freely. Hence, every possible incident angle inside the KATRIN beamline can be probed.

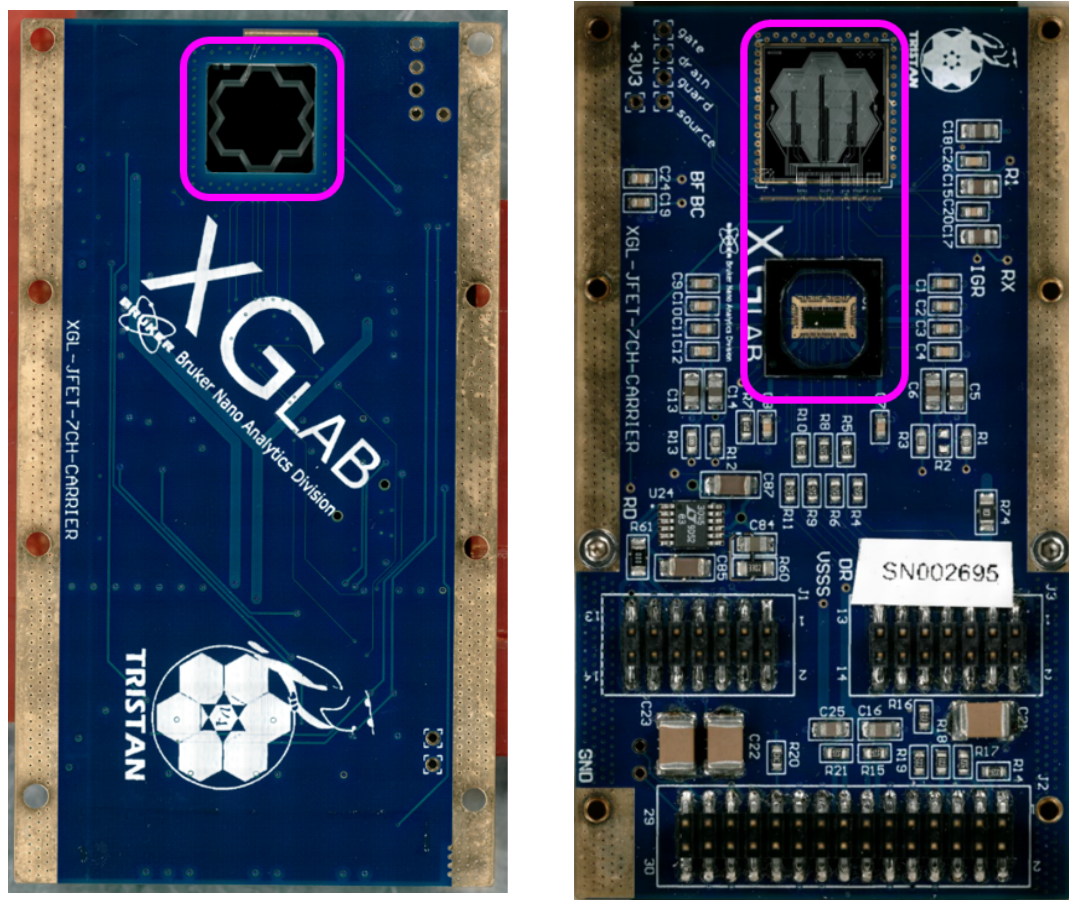


**Figure 5.3: PCB Board with the Seven-Pixel Prototype Detector.** Left: The entrance window side of the detector board is shown. The seven hexagonal pixels can be seen in the upper center. Right: The top side of the detector board is pictured, where the pixels with their readout lines and the ETTORE pre-amplifier directly beneath are visible.

The backscattered electrons are detected by the 166-pixel detector module, see fig. 5.4. The BSD is directed to the SOD, while aligning the centers of both detector chips. For this purpose, the module is mounted on a copper stand to fix the detector chip height above ground as well as on an aluminium plate for stability and fixation on the cooling plate. To probe different take-off angles in respect to the SOD, the module is rotatable around the same axis as the SOD. There is no direct line of sight between the electron gun and the BSD. The closest distance between the BSD and SOD chip amounts to about 2.4 cm. As a result, for a BSD chip size of 3.9 cm, maximal angular coverage within one measurement is guaranteed.

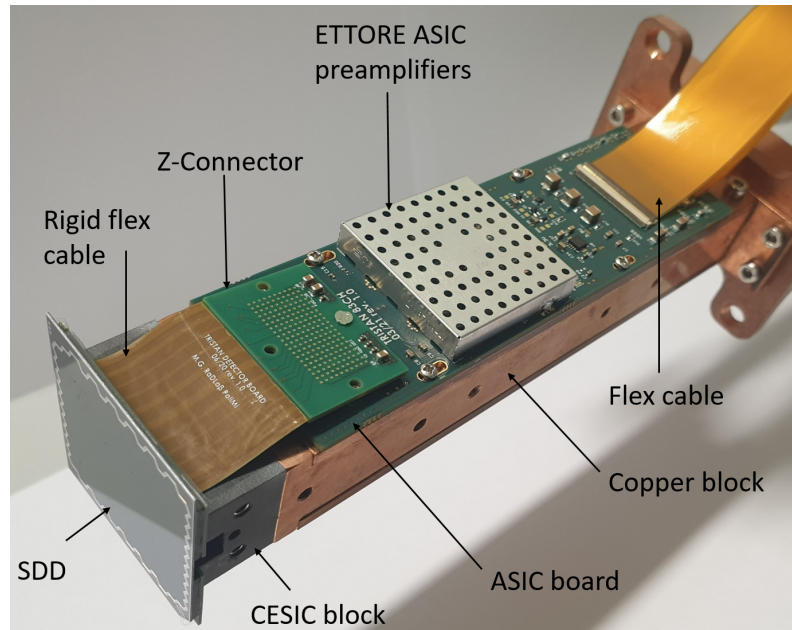


**Figure 5.4: 166-Pixel Detector Module.** The SDD chip is glued on top of a CESIC block which is further mounted onto a hollow copper block. On both sides of the copper block there is a ASIC board with ETTTORE pre-amplifiers. Rigid flex cables connect the detector chip with the detector board via a Z-connector. Flex cables also connect the ASIC boards with the power supply and the DAQ system. The copper block can be mounted on further holding structures and cooling systems. Figure adapted from [56].

The electron beam has a small angular distribution leading to a beam diameter at the SOD placement of about 1–2 cm. As a result, a stainless steel shield with a small hole of 3 mm in diameter has been inserted between the electron gun and the SOD for two reasons. First, it is supposed to protect the BSD chip. There is a small area at the module where the backside of the chip is exposed. Since, the module can be placed very close to the electron beam, the shield prevents this small area from irradiation. The second task of the shield is to avoid too much electrons hitting the PCB board of the SOD. Since the PCB material is an insulator, electrons would charge it up. Especially close to the detector chip, this should be avoided since it leads to electric fields and spontaneous discharge.

To ensure a correct alignment of the electron beam and the central pixel of the SOD, steering coils were placed in front of the electron gun. Two pairs of coils are arranged in horizontal and vertical direction respectively. Via a constant current through the coils, a constant magnetic field is generated to deflect the electrons. Moreover, the earth magnetic field, which unavoidably deflects the electrons as well, can be compensated. Nonetheless, within the measurements the steering coils were not needed due to very good alignment of the electron gun and the SOD.

Electrical noise reduction can be achieved by cooling. Therefore, the whole setup is placed on top of a cooling plate. Since copper is a good thermal conductor, the heat from the detector chips and electronics is transported via the holding structures to the cooling plate.

### 5.1.2 Readout-Chain

Fig. 5.5 shows the readout-chain exemplary for one SDD pixel. In the following, each step of the readout-chain will be explained in detail.

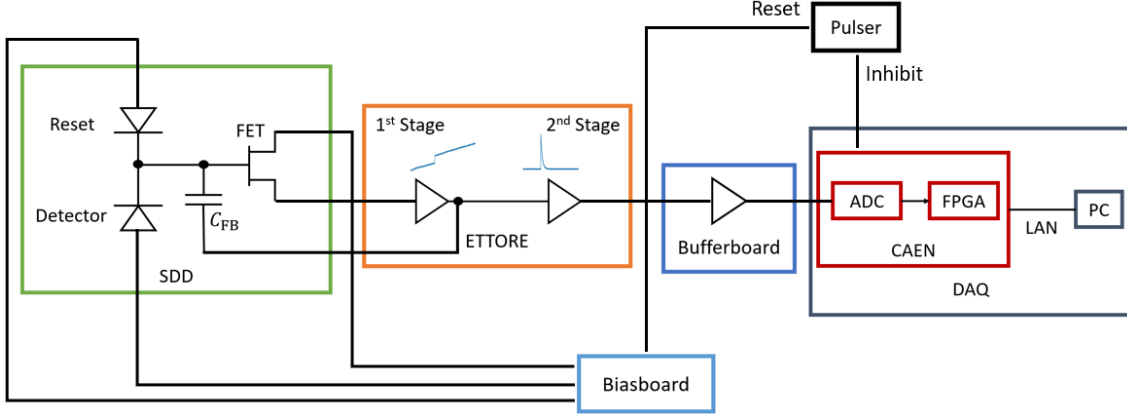


**Figure 5.5: Readout-Chain for One Pixel.** The energy deposition from the incoming particle is collected on the feedback capacitance  $C_{FB}$  in the SDD. The ETTORE ASIC processes the output signal, whereby two pre-amplification stages are provided. The buffer board further amplifies the signal before it is digitised via an ADC in the CAEN DAQ. FPGAs evaluate the energy of the particle. The result is transferred to a PC. A pulser periodically discharges the feedback capacitor with a reset signal, which is passed on to the SDD via the bias board. A second signal inhibits the ASIC during the reset. The bias board provides furthermore all voltages for the SDD.

The free charge carriers created in the SDD are collected on a capacitance  $C_{FB}$  in the feedback loop of the first signal amplifier. The output signal is the integral of the detector current. Therefore, each event leads to a step in the output signal, which height is proportional to the energy of the underlying particle. These steps have a non-zero rise time due to the detectors charge collection time and intrinsic capacitance of the SDD. The rise time is defined as the time it takes for the signal to rise from 10 to 90% of the step amplitude [73].

The signal of the SDD is read out by ETTORE ASICs (Application-Specific Integrated Circuits) [74] designed by XGLab in collaboration with Politecnico di Milano. ETTORE has two amplification stages, a DC-coupled stage (first stage) operated in periodic reset mode and an AC-coupled stage (second stage) with a time constant of  $15\ \mu\text{s}$  [49]. One ETTORE ASIC can read out 12 pixels. Therefore, the 166-pixel detector module has two ASIC boards which each host 7 ETTORE ASICs. The 7-pixel detector PCB only provides one ETTORE ASIC.

The first stage output consist of a voltage ramp. Its slope depends on the leakage current which continuously charges the feedback capacitor. For every incident particle, a steep step is superimposed on the ramp. The second amplification stage is a high-pass filter of first order using a RC circuit to keep fast signals as events while filtering out slow signals as the ramp. As a result, a step caused by an event is followed by an exponential decrease with a characteristic time constant of  $15\ \mu\text{s}$  [49]. An additional gain between 5 and 10

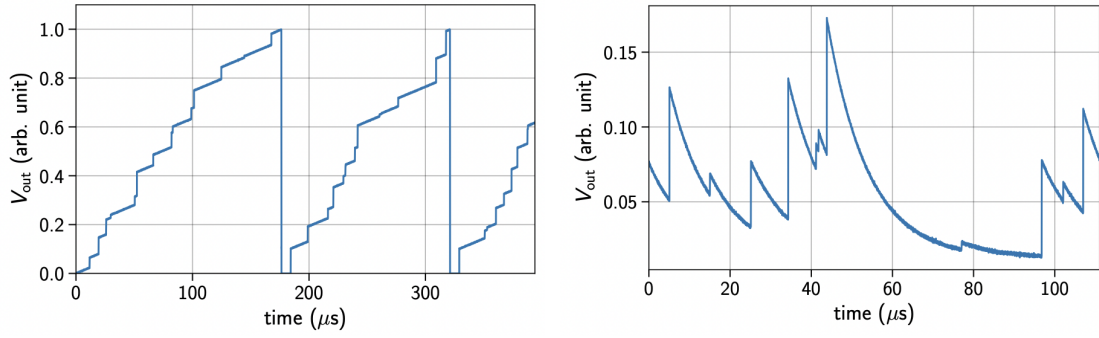


**Figure 5.6: Waveform Samples for First and Second Stage Amplification.** Left: First stage waveform as a function of time with active resets. The slope of the ramp corresponds to the leakage current. The events are step steps. Right: Second stage waveform as a function of time without active resets. Event steps are followed by exponential tails with a characteristic time constant. Plot taken from [73].

can be chosen. To prevent the saturation of the first stage output, the capacitor has to be discharged by an active reset through an additional circuit. The reset can be either set periodically by external electronics or triggered if the signal crosses a preset voltage threshold. An exemplary first and second stage waveform can be seen in fig. 5.6.

After the ETTORÉ ASICs, the signal is passed on to the buffer boards outside the vacuum chamber via a flange. The buffer boards increase the voltage signal by a factor of two, hence providing a third amplification. Two separate buffer board systems exist, one for the SOD and one for the BSD.

The signals from both buffer board systems are forwarded to the CAEN DAQ system, which consists of 3 cards with 64 channels each. Here, the analog signal is converted to a digital one by means of a 16-bit Analogue-to-Digital Converter (ADC) with a sampling rate of 125 MHz [75]. In the subsequent Field Programmable Gate Arrays (FPGAs), the energies of the observed particles are evaluated by a trapezoidal filter, which is illustrated in fig. 5.7.

With the trapezoidal filter, the step signal is turned into an isosceles trapezoid with defined width and the same height as the step signal. It averages the sampled signal over a given range within the shaping time  $t_{\text{shape}}$  and subtracts two of such regions separated by the gap time  $t_{\text{gap}}$ . This operation is then repeated for each sample point. The gap time has to be at least as long as the signal rise time. Through averaging, noise is smoothed leading to an improved energy resolution. On the one hand, the higher  $t_{\text{shape}}$ , the better is the energy resolution. On the other hand, short shaping times are required for the minimisation of pileup and the dead time. A fast filter marks possible events above a preset threshold, while a second filter precisely determines the energy of those events.

Two additional devices are needed to operate the system: The bias board and the pulser. The bias board provides all detector biases. There are two bias boards, one for each detector. Therefore, the detector voltages can be set independently for both detectors. The pulser provides the reset signal for the discharge of the SDD capacitors and an inhibit signal which inhibits the ASIC during the reset. The reset signal is passed on to the

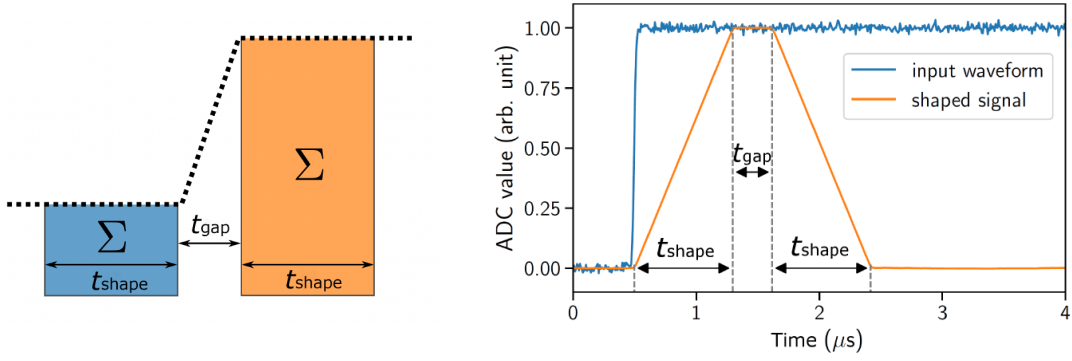


**Figure 5.7: Trapezoidal Filter Principle.** Left: The black dots resemble the signal waveform. The average of the samples in the orange time window is subtracted by the average of the samples in the blue one. The time windows are defined by the shaping time  $t_{\text{shape}}$  and separated by the gap time  $t_{\text{gap}}$ . Right: The resulting trapezoid-shaped signal is illustrated. The height of the trapezoid matches the step height from the input signal. The width is defined by  $t_{\text{shape}}$  and  $t_{\text{gap}}$ . Figures adapted from [73].

detector via the bias boards and is applied to each channel in the setup simultaneously. The inhibit signal is sent to the DAQ system.

## 5.2 Measurements and Settings

A set of nine measurements was taken for different initial energies and incident angles of the electron.  $E_I$  was varied between 5 keV and 10 keV in 2.5 keV steps. For each initial energy, data was taken for an incident angle of  $0^\circ$ ,  $31^\circ$  and  $59^\circ$  (see fig.4.5). The measurement parameters for each run can be looked up in table 5.1. For every measurement, the included angle between the BSD plane and the SOD plane was set to  $45^\circ$ .

**Table 5.1: Overview of the Measurement Settings.** For each measurement its name, the date on which it was recorded, the initial electron energy, the incident angle of the electron beam, the effective run time and the approximate count rate in the central pixel of the SOD are listed.

Name	Date	$E_I$	$\Theta_I$	Effective run time	Rate in CC
BS1	17.10.2022	10.0 keV	$0^\circ$	5100 s	5 – 6 kcps
BS2	17.10.2022	5.0 keV	$0^\circ$	7200 s	4 – 5 kcps
BS3	18.10.2022	7.5 keV	$0^\circ$	3600 s	6 – 7 kcps
BS4	19.10.2022	10.0 keV	$31^\circ$	3600 s	3 – 4 kcps
BS5	19.10.2022	5.0 keV	$31^\circ$	4200 s	2 – 3 kcps
BS6	19.10.2022	7.5 keV	$31^\circ$	3600 s	3 – 4 kcps
BS7	20.10.2022	10.0 keV	$59^\circ$	3900 s	2.5 – 3.5 kcps
BS8	20.10.2022	5.0 keV	$59^\circ$	4200 s	1.5 – 2 kcps
BS9	20.10.2022	7.5 keV	$59^\circ$	3600 s	2 – 2.5 kcps

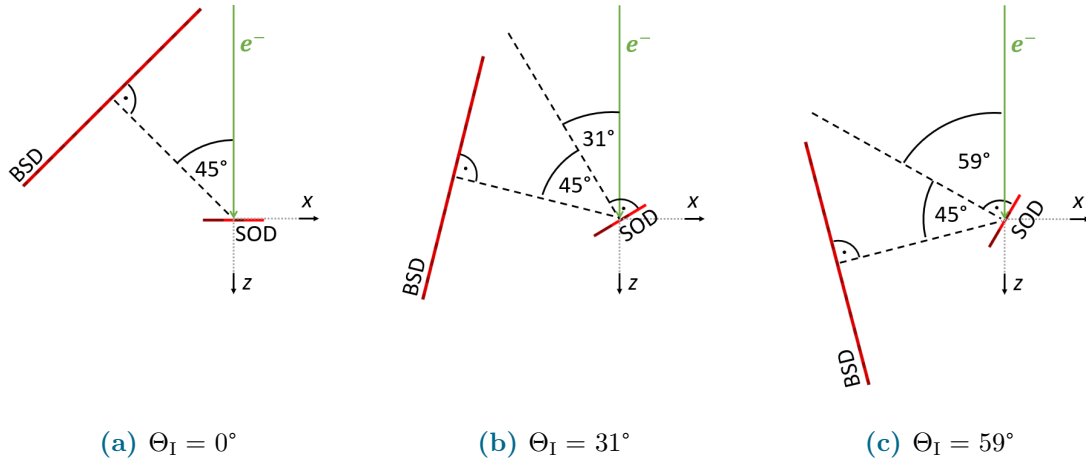
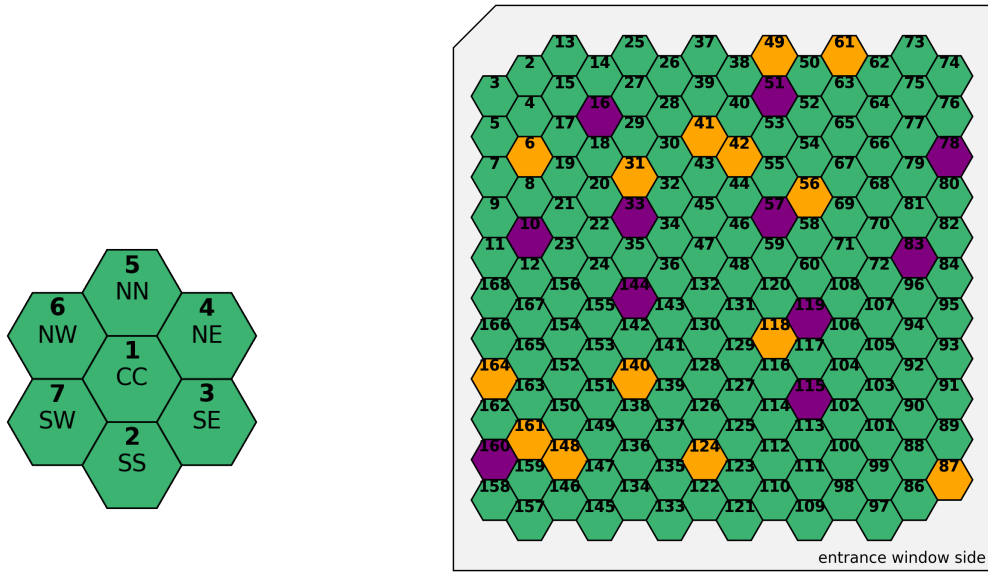


**Figure 5.8: SOD and BSD Positioning for Different Incident Angles.** The experimental setup is sketched in a top-view. The electron beam is drawn in green, the SDDs are illustrated in red. The dashed lines indicate the planes perpendicular to the detectors.



**(a) 7-Pixel SDD.** The pixels are numbered from 1 to 7 and additionally enumerated by compass directions **N**orth, **E**ast, **S**outh and **W**est. The **C**entral pixel is defined as **CC**. In the setup, the chip is rotated counterclockwise by  $90^\circ$ , hence the west side of the detector chip points towards the cooling plate.

**(b) 166-Pixel SDD.** The pixels are numerated consecutive from 2 to 84 in the northern and from 86 to 168 in the southern hemisphere of the detector chip. The green pixels are included in the following analysis. Orange pixels were already switched off during the data taking and purple ones were excluded during the data analysis.

**Figure 5.9: Pixel Nomenclature of the SOD and BSD.** For the SOD the backside and for the BSD the entrance window side of the detector chip is shown.

The vacuum chamber has to be reopened for every chosen incident angle to rearrange the detectors. Before the cooling can be switched on, a reasonable vacuum pressure has to be reached. Hence, to reduce the waiting time between the measurements, the temperature was set only to  $-10^{\circ}\text{C}$ . This leads to an effective temperature at the detector chips of around  $0^{\circ}\text{C}$ . The vacuum pressure was in the order of  $10^{-6}$  mbar for all measurements.

In each measurement run, listmode data (energy and timestamp of the event) was recorded for each pixel. To identify an event, a fast filter threshold of 100 lsb was chosen. The energy was extracted by a trapezoidal filter with  $t_{\text{shape}} = 2 \mu\text{s}$  and  $t_{\text{gap}} = 0.4 \mu\text{s}$ . The nomenclature of every pixel as used in the following analysis is depicted in fig. 5.9. A few of the pixels of the backscattering detector had connection issues or very high noise signals and were therefore switched off during the data taking or excluded later from the analysis.

### 5.3 Data Analysis

To investigate backscattered electrons, several analysis steps have to be taken. First, the detector system has to be calibrated like explained in subsection 5.3.1. Furthermore, the influence of charge sharing on the spectral shape is addressed and corrected in subsection 5.3.2. Pileup is considered in subsection 5.3.3 as a major uncertainty in the correct determination of the number of initial electrons, which in return is addressed in subsection 5.3.4. In addition, the coincidence analysis, as the main tool for backscattering identification, is explained in subsection 5.3.5.

#### 5.3.1 Iron Calibration

In order to translate the height of the trapezoidal filter of the DAQ in units of lsb (least significant bit) into energies in units of keV, the detector system has to be calibrated. Theoretically, a calibration with mono-energetic electrons or photons is possible, but photons are preferred. Their interaction is point-like and very probable in the sensitive volume of the SDD. Therefore, the peak position in the energy spectrum is barely effected by the transition layer. The photon peak is fitted with a Gaussian function to extract its mean position in lsb. The lsb value is then related to the known photon energy. Two photon peaks are used for a linear energy calibration [76].

For this purpose, an  $^{55}\text{Fe}$  source was inserted in the setup before the backscattering measurements, which can be seen in fig. 5.10. It has a half-life of 2.74 y [77] and decays via electron capture into  $^{55}\text{Mn}$  emitting X-rays [78]. The  $K_{\alpha}$  peak at 5.9 keV and  $K_{\beta}$  peak at 6.5 keV were fitted for the calibration [78]. Since both peak energies are relatively close together, an increasing calibration error for higher or lower energies is expected. It was assumed that the calibration curve parameters stay constant over time, therefore, only one calibration per pixel for all backscattering measurements was performed.

The calibrated  $^{55}\text{Fe}$  spectrum can be seen in fig. 5.11. Additional photon peaks were observed in the spectra which differ for both detectors. Their origin is still inconclusive and under investigation. For the SOD, additional peaks were observed approximately at 1.7 keV, 2.6 keV, 3.7 keV and 4.1 keV. The first peak is most probable the fluorescence

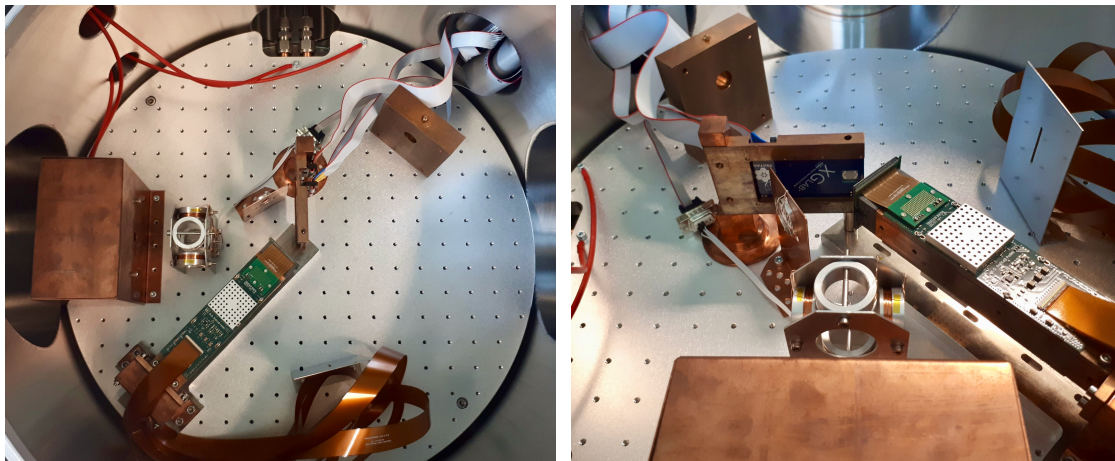


**Figure 5.10:  $^{55}\text{Fe}$  Source Positioning.** An  $^{55}\text{Fe}$  source was fixated onto a copper holding structure to lift it to the height of the detectors. The structure was placed as close as possible to the detector chips without the danger of touching them. Both detectors were illuminated simultaneously within one calibration measurement.

line of silicon at 1.74 keV. These photons could originate from the large silicon detector chip of the BSD. The other three peaks, which are also visible in the BSD, probably are fluorescence peaks from materials inside the iron source. Elements fitting by energy would be chlorine and calcium [65]. The two peaks at around 4.5 keV and 4.8 keV, visible only in the BSD iron spectrum, might originate from fluorescence of materials around the SOD chip.

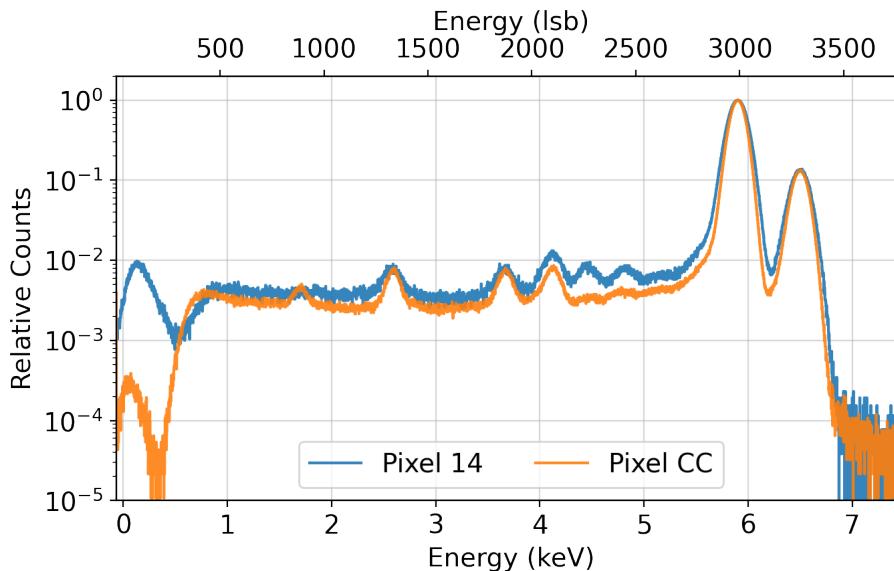


**Figure 5.11:  $^{55}\text{Fe}$  Spectra for One Exemplary Pixel per Detector.** Both spectra are scaled to the height of the 5.9 keV peak. Additional fluorescence lines besides the  $K_\alpha$  peak and  $K_\beta$  peak from the iron source are visible. The BSD has a higher noise peak at energies below the DAQ energy threshold and a worse energy resolution.

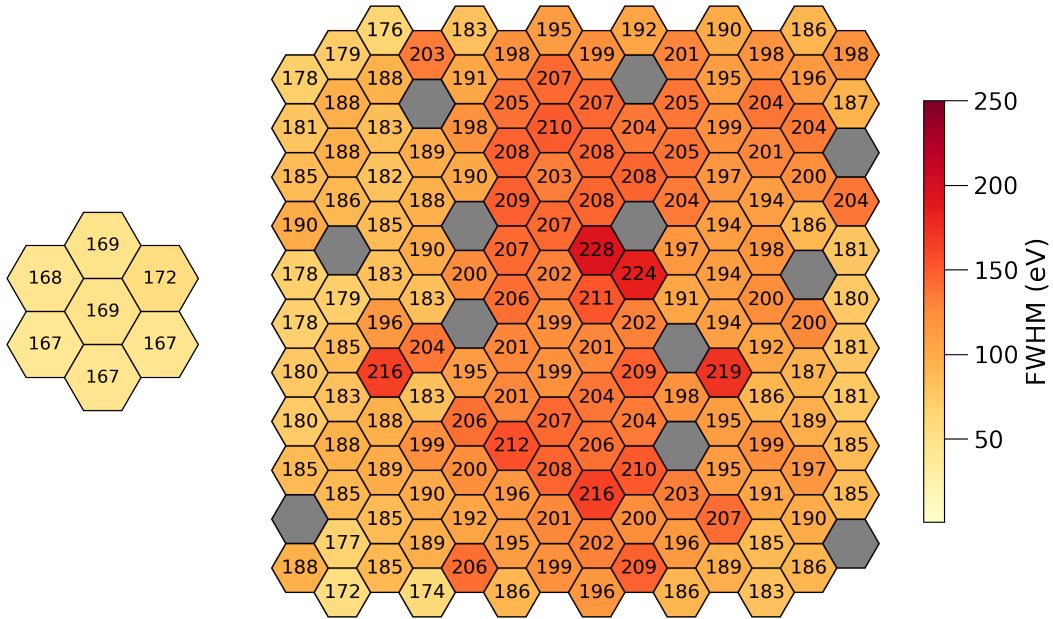


**Figure 5.12: Energy Resolution of Both Detectors at 5.9 keV.** The mean energy resolution is 168 eV FWHM for the SOD and 195 eV FWHM for the BSD at 5.9 keV. The energy resolution has a higher variation for the BSD than for the SOD. Grey pixels have been switched off during data taking due to cable or noise issues.

Some pixels in the BSD show additionally nonphysical behaviour close to the energy threshold or an excessive noise peak at low energies. They are excluded in the next analysis steps. The affected pixels are indicated in fig. 5.4.

From the fit, the energy resolution of the detectors can be determined. In fig. 5.12, the FWHM of the  $K_\alpha$  peak for every pixel is shown. The SOD has a mean energy resolution of 168 eV (FWHM) at 5.9 keV. With 195 eV (FWHM) at 5.9 keV, the energy resolution is worse for the BSD. For the SOD, the energy resolution is very homogeneous, while the BSD has a higher variation in resolution. In total, the BSD has more electrical noise, which can also be seen at the higher noise peak at energies below the DAQ energy threshold in fig. 5.11.

### 5.3.2 Charge Sharing

As explained in section 4.3, charge sharing between pixels has an impact on the shape of the electron energy spectrum. Charge sharing events can be identified to some extent via their time stamp. They can be defined as events that triggered two or more adjacent pixels within a selected small time window. Those events are then erased from the data, which is called a multiplicity or charge sharing cut (CSC). In order to not discard too many random coincidence events, the size of the time window has to be optimized. In fig. 5.13, the amount of identified coincidence events in the SOD as a function of the time

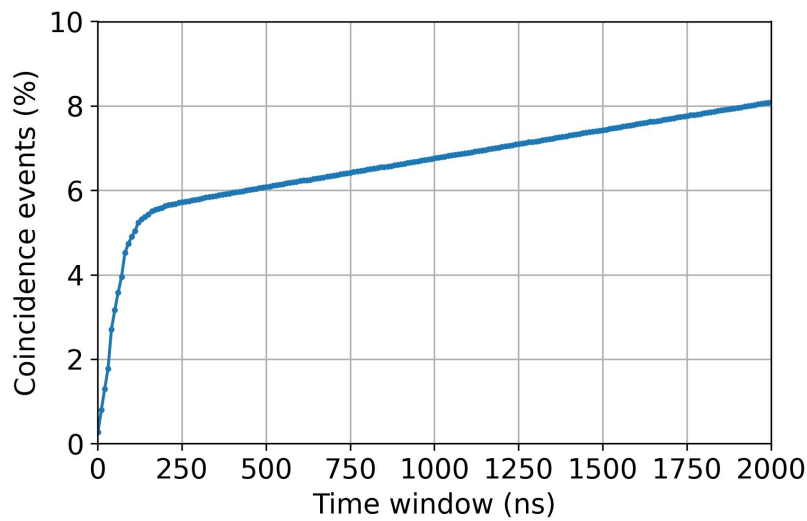


**Figure 5.13: Amount of Coincidence Events in the SOD as a Function of the Time Window.** The larger the time window, the more events are tagged as charge sharing events. The amount of random coincidence constantly increases for larger time windows. The optimal time window is at the point where the slope changes.

window is shown. The optimal time window is at the point where the slope changes. Here, one stops identifying coincidence between charge sharing events and starts mainly tagging random coincidence. As a result, an ideal time window of 200 ns was selected.

For the electron backscattering measurements, a CSC was applied for the SOD. The difference in the spectral shape before and after the cut can be seen in fig. 5.14. Especially the transition layer shoulder and the beginning of the backscattering tail are affected. The spectral shape without charge sharing events cannot fully be determined, as charge sharing events are not identified if one of the charge cloud partitions is too small to be detected. As a result, especially the original transition layer shoulder is not fully reconstructable.

Backscattered electrons are not mono-energetic. Hence, charge sharing in the BSD was assumed to have a much smaller effect on the shape of the detected continuous energy spectrum and was neglected. Furthermore, a CSC is much more complicated for the BSD due to the highly increased number of pixels.

The tagged charge sharing events are additionally used to correctly reconstruct the number of incident electrons. Therefore, events identified as charge sharing are counted as half an event. Uncertainties arise from random coincidence events falsely identified as charge sharing or unidentified charge sharing events. Therefore, an uncertainty on the calculated total number of incident electrons due to charge sharing is estimated to be about 1 %.

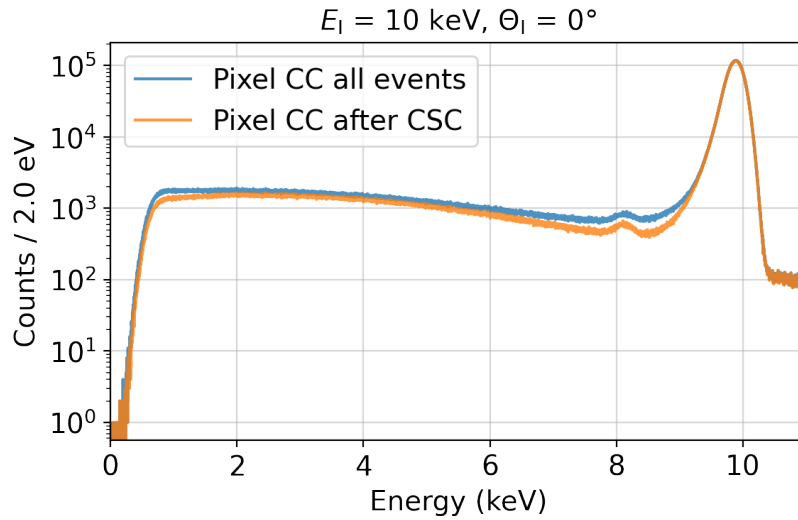


**Figure 5.14: Spectral Effect of Charge Sharing.** The electron energy spectrum of the central pixel of the SOD is shown before (blue) and after (orange) the CSC. The influence on the spectral shape especially at the transition layer shoulder and the beginning of the backscattering tail are visible.

### 5.3.3 Pileup

If two (or more) events are separated in time by less than the trapezoid filter duration, the trapezoids overlap, which is called pileup [75]. For very small overlaps, the DAQ can still separate the events, but the energy of the second event cannot be reconstructed correctly. For larger overlaps either both event energies are determined wrong or the events are registered as only one at about the sum of both energy depositions. Hence, pileup affects both the spectral shape and the reconstruction of the number of incoming electrons. For higher rates, there is more pileup.

In fact, the DAQ system can flag possible pileup events based on their timestamp. Nonetheless, this option has never been tested in respect of reliability, and therefore, was not used in this analysis. Instead, it is further assumed that the effect on the spectral shape is small at the given rates of kcps in the SOD. In the BSD, with rates in the order of cps, pileup is hardly present, and therefore, assumed to have no considerable effect on the observed number of backscattered electrons.

In terms of incoming electron number reconstruction, complete pileup of two or three events resulting in one event at higher energies is accounted for by multiplying such events by respectively a factor of two or three depending on their energy. For this, energy thresholds are set as depicted in fig. 5.15. Events falling in the orange area are multiplied by a factor of two, events in the red one by a factor of three. Pileup events below the first threshold and above the third threshold are neglected. The energy of each threshold for the different measured initial electron energies are summarized in table 5.2. An uncertainty of 1% on the incoming electron number reconstruction due to pileup is assumed.

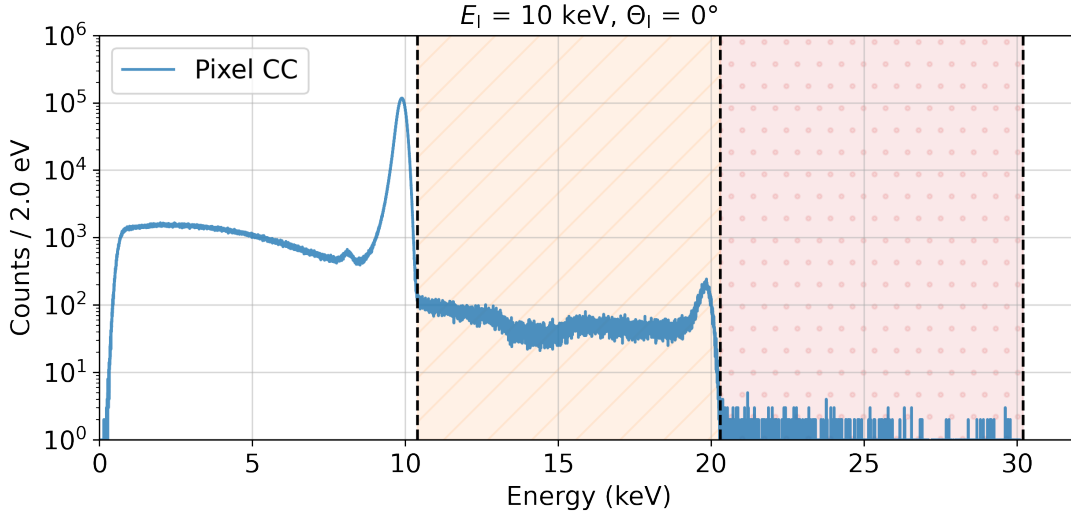


**Figure 5.15: Energy Thresholds for Pileup Considerations.** The energy spectrum of the central pixel of the SOD is shown. The energy thresholds (black dashed lines) are set at the falling edge of the Gaussian peaks. For the total event number reconstruction, events falling in the orange dashed area are multiplied by a factor of two, events in the red dotted one by a factor of three.

**Table 5.2: Pileup Thresholds for the Chosen Initial Electron Energies.** For every initial energy, the three energy thresholds for the pileup considerations, as illustrated by black dashed lines in fig. 5.15, are listed.

$E_I$	Threshold 1	Threshold 2	Threshold 3
5.0 keV	5.2 keV	10.0 keV	14.8 keV
7.5 keV	7.8 keV	15.2 keV	22.5 keV
10.0 keV	10.4 keV	20.3 keV	30.2 keV

### 5.3.4 Incoming Electron Number Reconstruction

For the comparability with later simulations, energy thresholds of  $E_{\text{SOD,T}} = 0.8$  keV for the SOD and  $E_{\text{BSD,T}} = 1$  keV for the BSD are set for the calculations of the number  $N$  of detected electrons per pixel. They are chosen to be above the energy threshold of the DAQ. Since there is higher noise in the BSD, its threshold is set higher than for the SOD.

For the SOD, the number of counts has to be corrected for charge sharing and pileup events, as previously described, to calculate the number of initial electrons. As a result, for each pixel  $i$  of the SOD:

$$N_{\text{SOD},i} = \frac{1}{2} \cdot \left\{ n_{\text{SOD},i} [E_{\text{SOD,T}} < E < E_{\text{PU,T1}}] + n_{\text{CSC},i} [E_{\text{SOD,T}} < E < E_{\text{PU,T1}}] \right\} \quad (5.1)$$

$$+ n_{\text{SOD},i} [E_{\text{PU,T1}} < E < E_{\text{PU,T2}}] \cdot 2 + n_{\text{SOD},i} [E_{\text{PU,T2}} < E < E_{\text{PU,T3}}] \cdot 3.$$

Here,  $E$  is the energy of the events measured in the SOD. For a pixel  $i$  of the SOD,  $n_{\text{SOD},i}$  denotes the number of all detected events, and  $n_{\text{CSC},i}$  the number of the remaining events

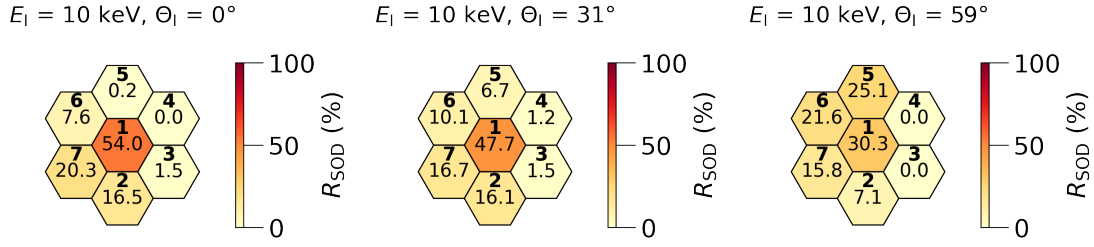


**Figure 5.16: Relative Number of Counts in the SOD for Different Incident Angles at  $E_I = 10$  keV.** Mainly the central pixel is irradiated by the electron beam at  $\Theta_I = 0^\circ$ . For higher incident angles, increasingly also the pixels 2, 5, 6 and 7 are hit.

after the charge sharing cut.  $E_{PU,T1}$ ,  $E_{PU,T2}$  and  $E_{PU,T3}$  are the energy thresholds for pileup as described in table 5.2. A combined uncertainty of 1.41 % on  $N_{SOD}$  per pixel is assumed, 1 % each for incomplete (or incorrect) charge sharing and pileup identification.

The relative number of counts  $R_{SOD}$  per pixel in the SOD can be seen in fig. 5.16 exemplary for  $E_I = 10$  keV.  $R_{SOD}$  varies between 2–4 % for different initial energies at fixed incident angle.

Mainly the central pixel is irradiated by electrons at  $\Theta_I = 0^\circ$ . In the geometry of the setup with the stainless steel shield, the maximal electron beam diameter at the plane of the SOD is about 5 mm. Hence, for a pixel diameter of about 3 mm, it is expected to hit more than one pixel. For higher incident angles, the other pixels are hit more and more since the effective area of the pixel facing the electron gun is smaller. In addition to the central pixel, especially the pixels 2, 5, 6 and 7 are hit, thus the pixels directed towards the cooling plate. The number of electrons hitting the SOD chip next to the sensitive area or the PCB can be assumed to be negligible. In conclusion, the backscattering electron energy spectra and angular distribution are a superposition from backscattering of all involved SOD pixels.

### 5.3.5 Coincidence

To extract the properties of backscattered electrons originating from only one pixel of the SOD, a coincidence cut can be applied. It is possible to filter coincidence events between two pixels also for different detectors by their timestamp. For this, as for the investigation of charge sharing, it is possible to define a coincidence time window. The identified coincidence events are especially interesting as they contain the information on backscattering. They likely originate from electrons which first hit one pixel of the SOD, were backscattered and then hit a pixel of the BSD.

The time the electron needs to propagate from one detector to the other is in the order of ns or below for the observed energies and the detector distances and is therefore negligible. The propagation time is even smaller than the sampling frequency of the DAQ. In contrast, the coincidence time window is highly dependent on the charge collection time of the SDD itself. The incident electron and the backscattered electron most likely hit the pixels at

different distances to the respective pixel anode. The difference in time that the created charge clouds need to travel to the respective anode can in the most extreme case be up to about 500 ns [79]. This can also cause backscattered electrons being recorded before the initial electron.

The amount of coincidence events between the CC pixel of the SOD and any pixel of the BSD is depicted in fig. 5.17 as a function of the time window. To avoid to trigger on noise events, all events inside the BSD with energies below 0.6 keV have been discarded, also for the following data analysis. The optimal time window was chosen to be 500 ns. The amount of random coincidence is very small. Therefore, the number of falsely classified coincidence events is assumed to be negligible.

Nevertheless, if one of the events falls below the detection threshold, the other one cannot be identified as a coincidence event. This happens for elastic backscattering where the initial electron is reflected at the detector surface, or for inelastic backscattering in the entrance window. These electrons are not detected in the SOD. Moreover, especially secondary electrons being produced and backscattered towards the BSD are affected, as they are mostly low-energetic, and therefore, very likely fall under the detection threshold of the BSD. This emphasises how important a low energy threshold is for the investigation of incomplete charge collection.

The energy spectra recorded by the SOD and the BSD are in the following investigated with and without coincidence cut.

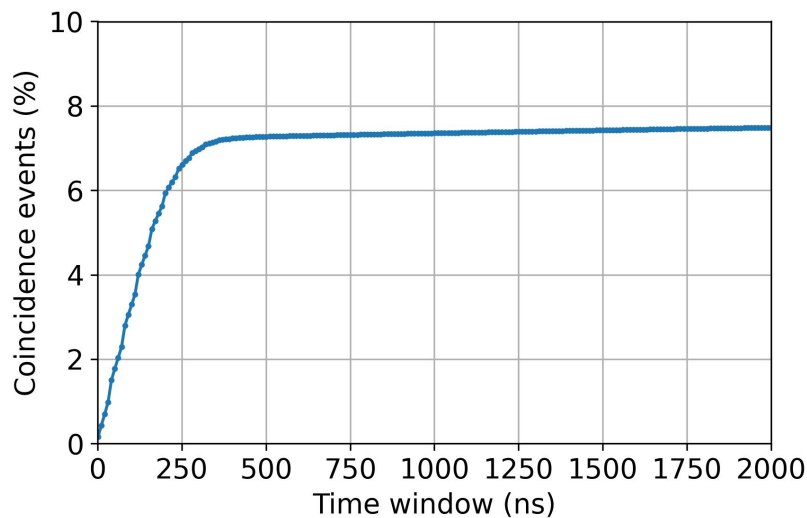


**Figure 5.17: Amount of Backscattering Coincidence Events as a Function of the Time Window.** The coincidence between the CC pixel of the SOD and any pixel of the BSD is shown. For small time windows mainly real coincidence events are tagged. For large time windows only random coincidence leads to a small increase. An ideal time window of 500 ns was chosen.

## 5.4 Experimental Results

This section presents the experimental results for the different measurement settings. Subsection 5.4.1 covers the results regarding all measured events per run, while subsection 5.4.2 deals with events tagged as coincidence events. Both subsections are divided in three parts. The first part is presenting the observed electron energy spectra of the incident and backscattered electrons. The second part is investigating the angular distribution of the measured backscattered electrons. In the third part, the backscattering coefficients are evaluated and investigated.

### 5.4.1 All Events

#### Energy Spectra

On the left side of fig. 5.18, the initial electron energy spectra of the CC pixel of the SOD are shown. At low initial energies, more energies are deposited in the entrance window of the SOD. At high incident angles, the path through the entrance window is longer. As a result, the main peak position is shifted towards lower energies and the transition layer shoulder is more pronounced at high incident angles and low initial energies. The silicon escape peak is only clearly visible for high initial energies and low incident angles. In the other cases, it is lost inside the transition layer shoulder or the backscattering tail.

All backscattering tails show a decrease in counts towards higher energy depositions in the SOD. For each  $E_I$  setting, the tail is steeper at low energy depositions for increasing incident angles, reaching an exponential decrease over the whole spectrum for  $\Theta_I = 59^\circ$ . The same trend but less pronounced can be observed for decreasing initial energy at fixed incident angle. As a result, for high  $\Theta_I$  and low  $E_I$  values, the energy deposition in the SOD is smaller and the energy of the backscattered electron is larger.

In fig. 5.18 on the right, the backscattered electron energy spectra for all pixels of the BSD combined are depicted. As the backscattering tail in the SOD indicates, the energy spectrum of backscattered electrons is continuous, and therefore, all effects like the transition layer and charge sharing effects are smeared out and thus lead to less spectral distortion. For high  $E_I$  and small  $\Theta_I$  values, a small photon peak at 1.7 keV is visible. It originates from photons being emitted after electron ionisation in the SOD.

The energy spectrum is very constant over the whole energy range at  $\Theta_I = 0^\circ$  for all initial electron energies. For larger  $\Theta_I$  values, the observed counts increase towards higher backscattering electron energies. Hence, at large incident angles, backscattered electrons have lost less energy in the SOD. The backscattered electrons in the area close to the endpoint of the backscattering spectrum are those which were backscattered near the detector surface of the SOD, and therefore, fell under the detection threshold of the SOD.

As a result, the energy spectrum of backscattered electrons coincides with the conclusions drawn from the backscattering tail of the SOD energy spectrum.

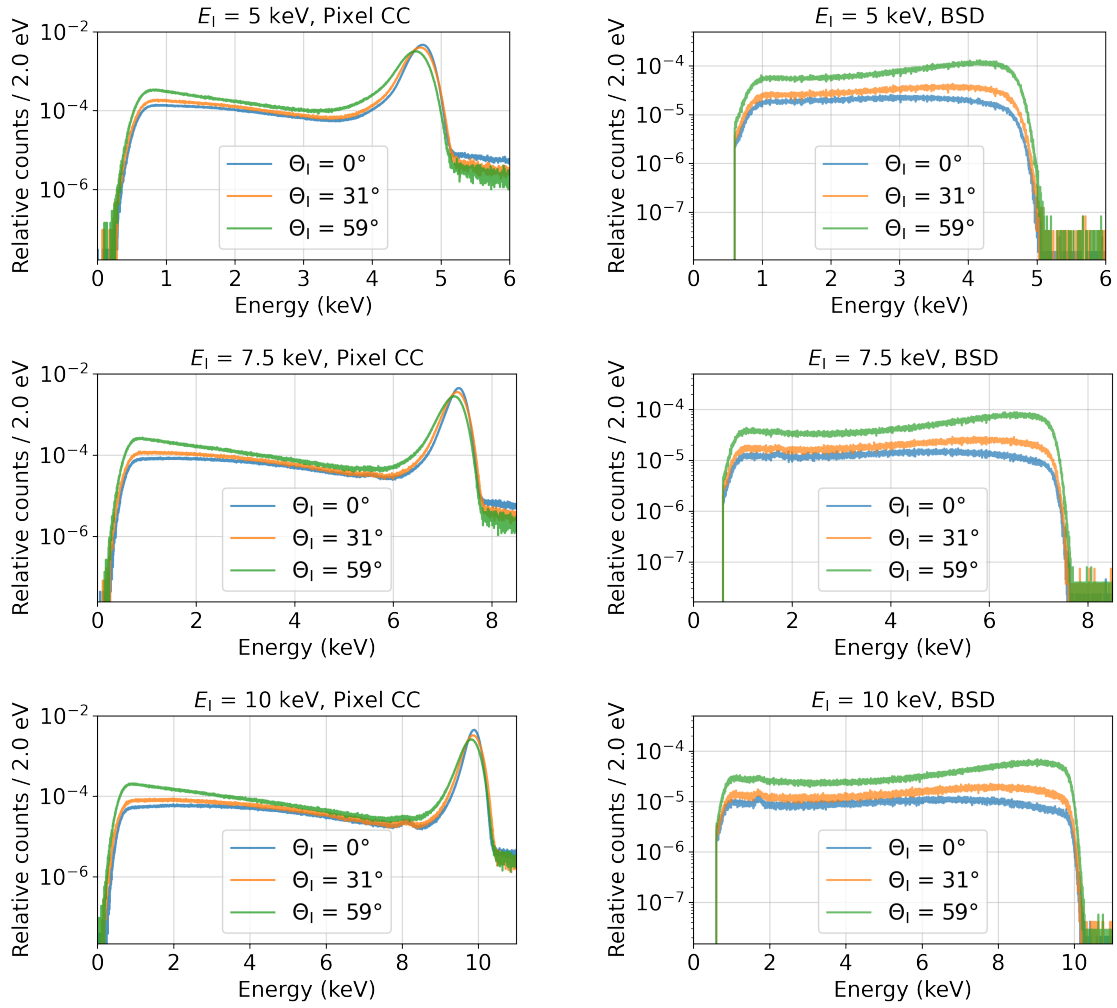


**Figure 5.18: Electron Energy Spectra Comparing Different Measurement Settings.** Left: The electron energy spectra measured in the CC pixel of the SOD are shown after the CSC. The counts per bin are divided by  $N_{\text{SOD,CC}}$  (eq. 5.1). Right: The electron spectra of backscattered electrons measured by all pixels of the BSD are shown. The counts per bin are divided by  $\sum_i N_{\text{SOD},i}$  (eq. 5.1). Counts below 0.6 keV have been discarded, as they originate predominantly from noise. For each setting, a spectral distortion especially at low energies in the SOD and consequently at high energies in the BSD is visible for increasing incident angles.

### Angular Distribution

For the number  $N_{\text{BSD},j}$  of backscattered electrons per pixel  $j$  in the BSD, charge sharing and pileup events are neglected, resulting in:

$$N_{\text{BSD},j} = n_{\text{BSD},j} [E > E_{\text{BSD,T}}]. \quad (5.2)$$

The number of events in pixel  $j$  of the BSD is denoted by  $n_{\text{BSD},j}$ , and  $E$  is the energy of the events measured in the BSD.

The direction of backscattered electrons can be defined in terms of two angles: The polar

backscattering angle  $\Theta_{\text{BS}}$  and the azimuthal backscattering angle  $\phi_{\text{BS}}$ . Both angles are illustrated in fig. 5.19. The resulting angles for each pixel of the BSD at the given take-off angle is depicted in fig. 5.20.

In fig. 5.21,  $N_{\text{BSD}}$  per pixel is depicted. The detected distribution of backscattered electrons is the result of mapping the 3D backscattering distribution onto a skewed 2D plane. For each setting, the angular distribution has a maximum around  $\phi_{\text{BS}} = 0^\circ$ . The number of backscattered electrons decreases towards the edges of the detector chip. The distribution is approximately symmetric to the  $x'$ -axis, and its maximum wanders to higher  $\Theta_{\text{BS}}$  for larger incident angles. Furthermore, the shape of the distribution changes from approximately circular to elliptic. As a result, for increasing incident angles the electrons are more backscattered towards higher  $\Theta_{\text{BS}}$  and more and more concentrated towards one direction. For different initial energies, the angular distribution stays majorly unchanged.



**Figure 5.19: Definition of the Backscattering Angles.** Left:  $\phi_{\text{BS}}$  is the angle included by the electron track (green arrow) and the negative  $x'$ -axis in the plane of the SOD (red area). The SOD is depicted from the entrance window side. Right:  $\Theta_{\text{BS}}$  is the angle between the electron trajectory and the negative  $z'$ -axis, the axis running perpendicular to the SOD surface.

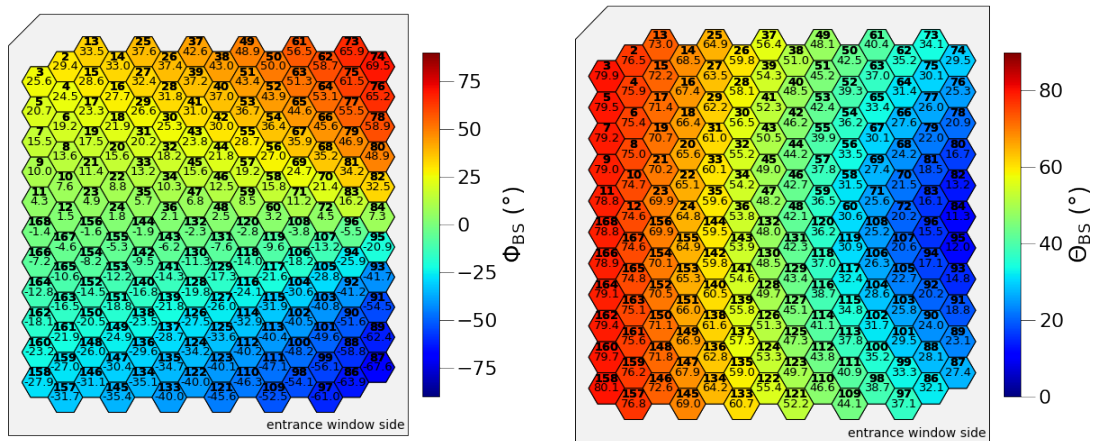


**Figure 5.20: Backscattering Angles for Each Pixel of the BSD.** For simplification, the beginning of the backscattered electron track is set to be at the center of the SOD and the ending at the respective BSD pixel center.

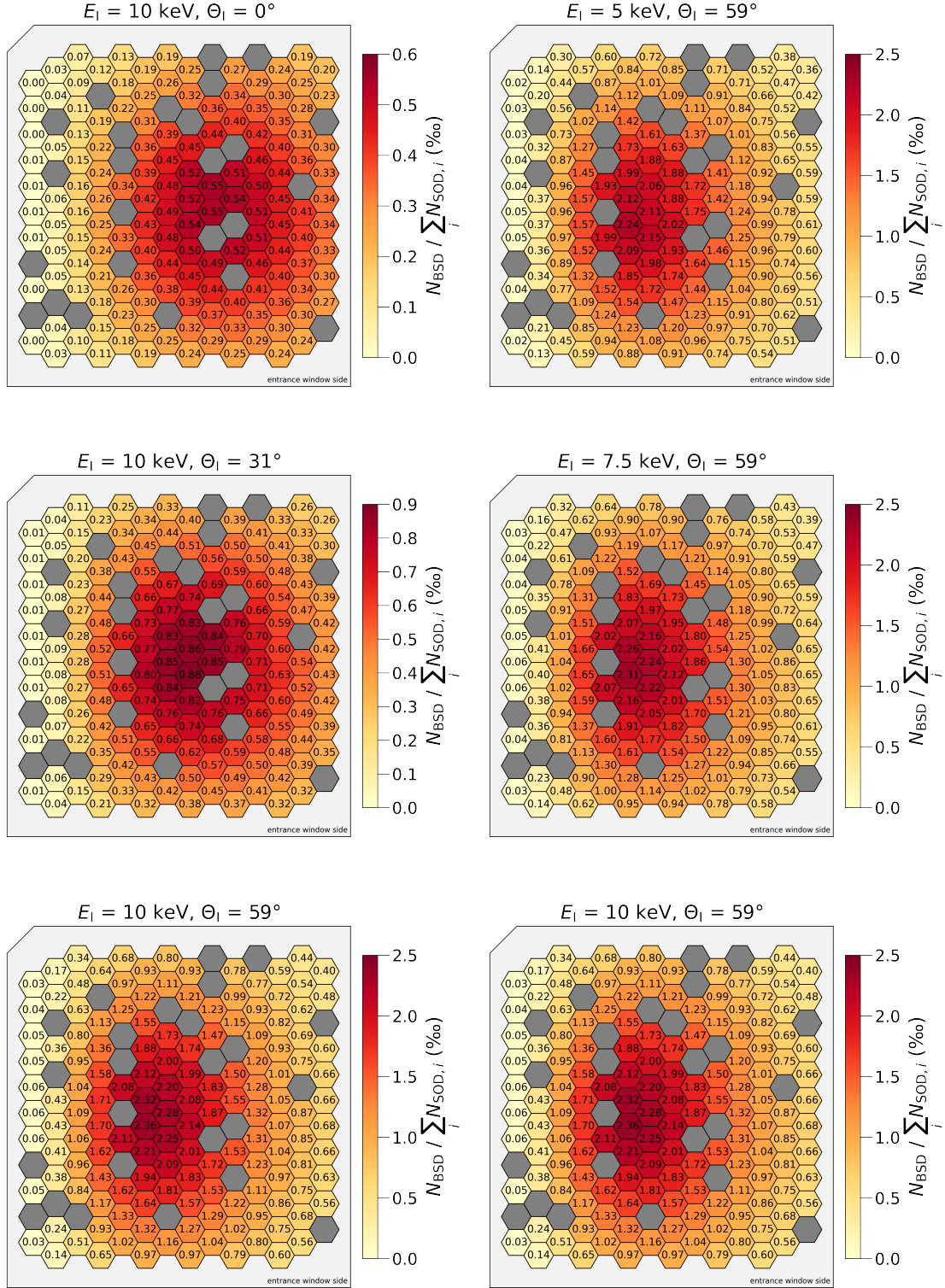


**Figure 5.21:** Number of Backscattered Electrons in the BSD for Different Measurement Settings. Left: The pixel maps are shown for increasing incident angles at  $E_1 = 10$  keV. Right: The pixel maps are shown for increasing initial energies at  $\Theta_1 = 0^\circ$ . The number of backscattered electrons per pixel in the BSD is divided by  $\sum_i N_{\text{SOD},i}$  (eq. 5.1). For each setting, the angular distribution is symmetric around  $\phi_{\text{BS}} = 0^\circ$ . The larger the incident angle, the higher is the polar backscattering angle.

### Experimental Backscattering Coefficient

To relate the number of detected backscattered electrons to the number of measured initial electrons, the experimental backscattering coefficient is calculated as:

$$\eta_{\text{exp}} = \frac{\sum_{j=1}^{166} N_{\text{BSD},j}}{\sum_{i=1}^7 N_{\text{SOD},i}}. \quad (5.3)$$

It depends on the energy thresholds set for each detector, the geometry of the setup including the size of the BSD, the charge collection efficiency inside the SDDs and the efficiency with which charge sharing and pileup events can be identified. The resulting coefficients for each measurement run are depicted in fig. 5.22 as a function of the incident angle directly comparing the different initial electron energies.

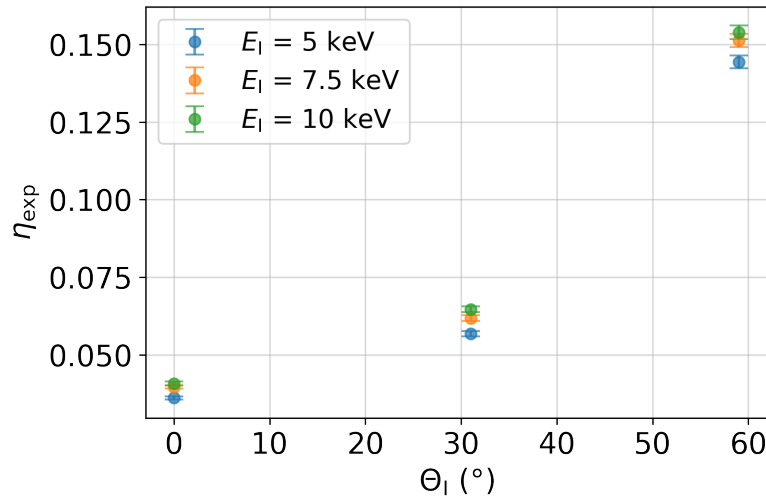


**Figure 5.22: Experimental Backscattering Coefficient as Function of the Incident Angle.** The experimental backscattering coefficient  $\eta_{\text{exp}}$  is calculated by equation 4.6. A total uncertainty of 1.41% on  $N_{\text{SOD}}$  of every SOD pixel is assumed. The coefficient highly increases for increasing incident angle, and it slightly decreases for decreasing initial energies.

The experimental backscattering coefficient highly increases from around 4% at  $\Theta_I = 0^\circ$  to about 14–16% at  $\Theta_I = 59^\circ$ . Therefore, there is in total more backscattering at higher incident angles. Nonetheless, it has to be noted that for larger incident angles more electrons are backscattered towards the direction of the BSD, and their energy is higher. As a result, the detection efficiency in respect to the total amount of backscattered electrons is higher at larger incident angles.

The experimental backscattering coefficient also slightly decreases for smaller initial electron energies. However, an increase in the backscattering coefficient for lower initial energies is expected. A hard energy threshold for the SOD was applied. The backscattering tail in the SOD is the highest at low energy depositions and low initial energies. Therefore, the number of included initial electrons in the SOD is lowered especially for small  $E_I$  values at a given threshold. Hence, under the applied conditions the relation between the initial electron energy and the backscattering coefficient is reversed.

### 5.4.2 Coincidence Events

#### Energy Spectra

In fig. 5.23, the energies of the coincidence events selected as described in section 5.3.5 are depicted in a 2D-histogram for  $E_I = 10$  keV and  $\Theta_I = 0^\circ$ . As expected, the energies of both events sum up to almost the initial electron energy leading to a diagonal in the plot. Since there are energy losses due to the transition layers of the detectors, not the whole initial energy can be reconstructed. Events falling below this diagonal are either random coincidence events or events where not all backscattered electrons were detected. Since the initial electron can produce several secondary electrons inside the SOD, more than one electron can be backscattered, but eventually only one is detected by the BSD, while the others might propagate in different directions.

Furthermore, there is a event concentration at 1.74 keV in the BSD and  $E_I - 1.74$  keV in the SOD. It arises from mono-energetic photons being generated in the SOD and escaping towards the BSD. It leads to the silicon escape peak in the energy spectrum of the SOD and a photon peak in the energy spectrum of the BSD. Next to the actual coincidence events, there is a second diagonal parallel to the first one but shifted by about  $E_I$  towards higher energies in the SOD. This structure arises from coincidence between the detection of a backscattered electron in the BSD and a pileup event in the SOD. The energy thresholds of both detectors can be seen as almost blank stripes on the left and bottom side of the histogram. Events besides the explained structures and also the vertical line at  $E_I$  are from random coincidence.

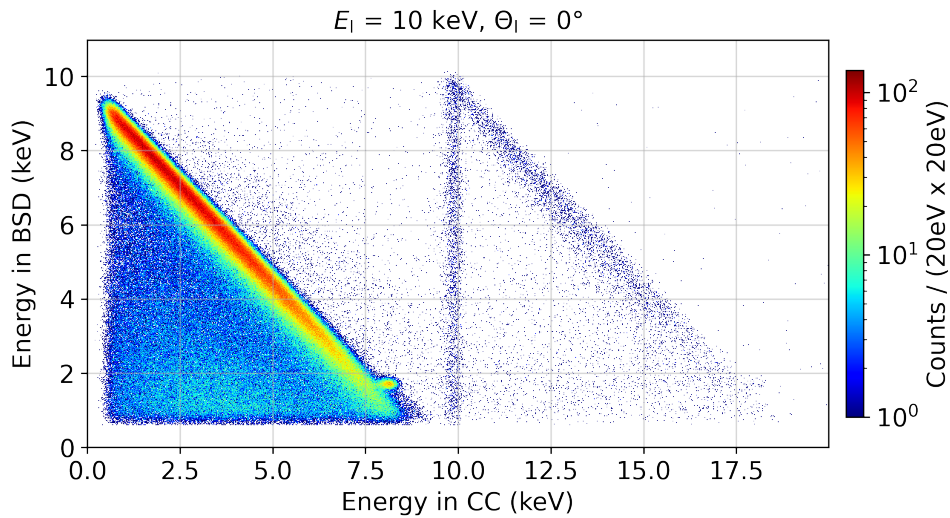


**Figure 5.23: 2D-Histogram for Identified Backscattering Coincidence Events.**

The energies of both events almost sum up to  $E_I$ , leading to a diagonal. For events falling below the diagonal, not all backscattered electrons were detected. The silicon escape peak in the SOD or rather the photon peak in the BSD is visible. A second diagonal arises from coincidence between a backscattered electron in the BSD and a pileup event in the CC pixel. Events besides the explained structures arise from random coincidence. The energy thresholds are visible as almost blank stripes on the left and bottom side.

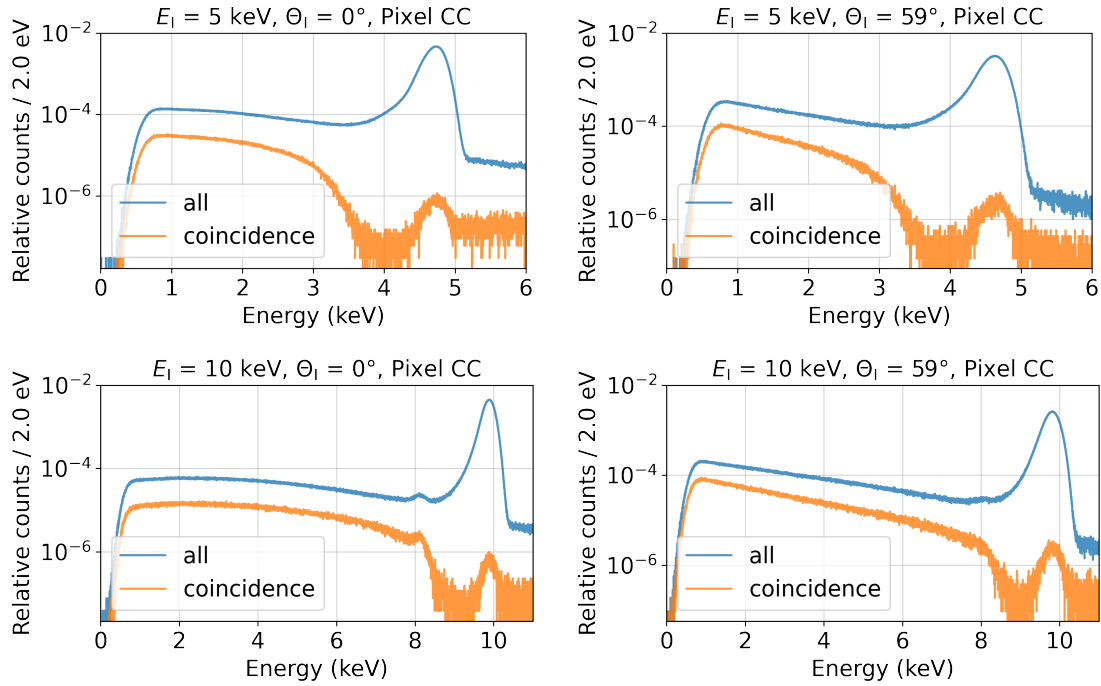


**Figure 5.24: Electron Energy Spectra of the CC Pixel Comparing All and Coincidence Events.** The counts per bin are divided by  $N_{\text{SOD,CC}}$  (eq. 5.1). The spectral shape of the backscattering tail can be mainly reconstructed by extracting coincidence events with the BSD. The energy spectrum of coincidence events is cut off at high energies due to the detection threshold of the BSD and its amplitude depends on the backscattering detection efficiency. Random coincidence leads to a small peak at  $E_1$ .

Relating an event in the SOD to one in the BSD, it is possible to extract the backscattering tail in the SOD energy spectrum. In fig. 5.24, the initial electron energy spectra of the CC pixel for the identified coincidence events in comparison to the energy spectrum of all events for four different measurement settings are shown.

The shape of the spectrum from coincidence events in the SOD resembles the shape of the backscattering tail of the energy spectrum of all events. The tail is cut off at high energies. Due to the detection threshold of the BSD, the corresponding high-energetic electrons in the SOD cannot be extracted by the coincidence cut. A lower energy threshold in the BSD can help to reconstruct the shape of the entire backscattering tail. Also a small peak at about  $E_1$  is visible, which arises from random coincidence. In total, this possibility to extract the tail shape can help to improve existing models of the detector response.

The heights of both spectra differ since the BSD has not full angular coverage and the angular backscattering distribution varies between the measurement settings. Additionally, a larger amount of backscattered electrons falls below the energy threshold of the BSD for lower  $E_1$ . This discrepancy in height provides the possibility to estimate the backscattering detection efficiency at a given setting. For this, the ratio of the counts of the coincidence events and all events between 1 keV and  $E_1 - 2.5$  keV is taken. The resulting backscattering detection efficiencies for each measurement are plotted in fig. 5.25 as a function of the incident angle. There is a linear increase in the detection efficiency

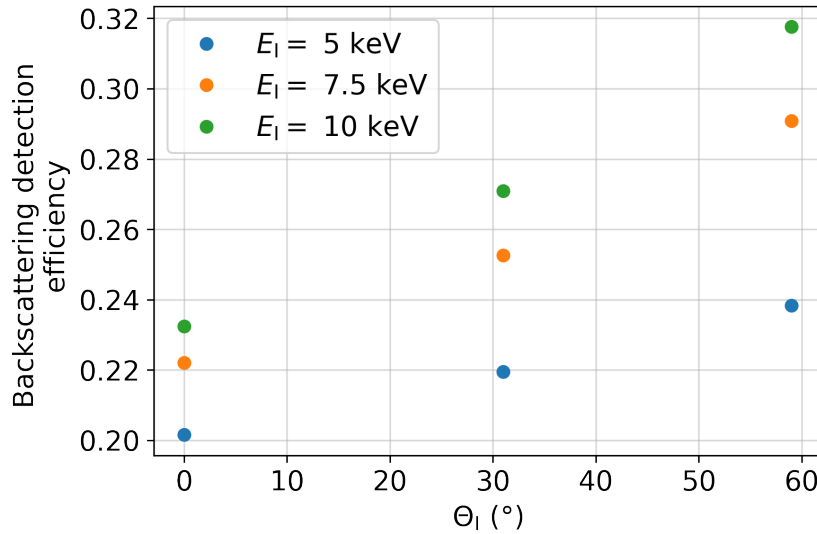


**Figure 5.25: Backscattering Detection Efficiency as a Function of the Incident Angle.** For this estimation of the efficiency, the amount of coincidence events with energies between 1 keV and  $E_1 - 2.5$  keV is related to the total amount of events in the same energy regime. The uncertainty on the counts in the investigated energy region is assumed to be negligible for this rough estimation of the efficiency. Therefore, no error bars are provided. The efficiency linearly increases with the incident angle and is larger for higher initial electron energies.

for increasing incident angles. The slope of the increase is higher for larger initial electron energies. In total, the higher  $E_1$  and  $\Theta_1$ , the more backscattered electrons can be detected.

The same comparison of coincidence events to all detected events can be done for the energy spectra of the BSD, as shown in fig. 5.26 for different measurement settings.

The spectral shape for coincidence events resembles the one for all events, but the spectrum is cut off at high energies. Backscattered electrons in this energy regime were not detected by the SOD, as they only deposit very little energy in the SOD, and therefore, fall below the energy threshold of the SOD. The effect is most prominent at small initial electron energies. The remaining backscattered electrons detected at high energies are random coincidence events.

The height difference of the spectra depends on the relative number of electrons hitting the central pixel of the SOD. By comparing the counts between 1 keV and  $E_1 - 2$  keV, it is possible to reconstruct how much percent of the electrons actually hit the CC pixel and not the surrounding insensitive area before they are backscattered. An approximate agreement with the numbers provided in fig. 5.16 was achieved, as can be seen in fig. 5.27. The highest discrepancy was found for large  $\Theta_1$ . Here, it is expected that the probability of the electron beam hitting the area next to the sensitive detector is the highest.

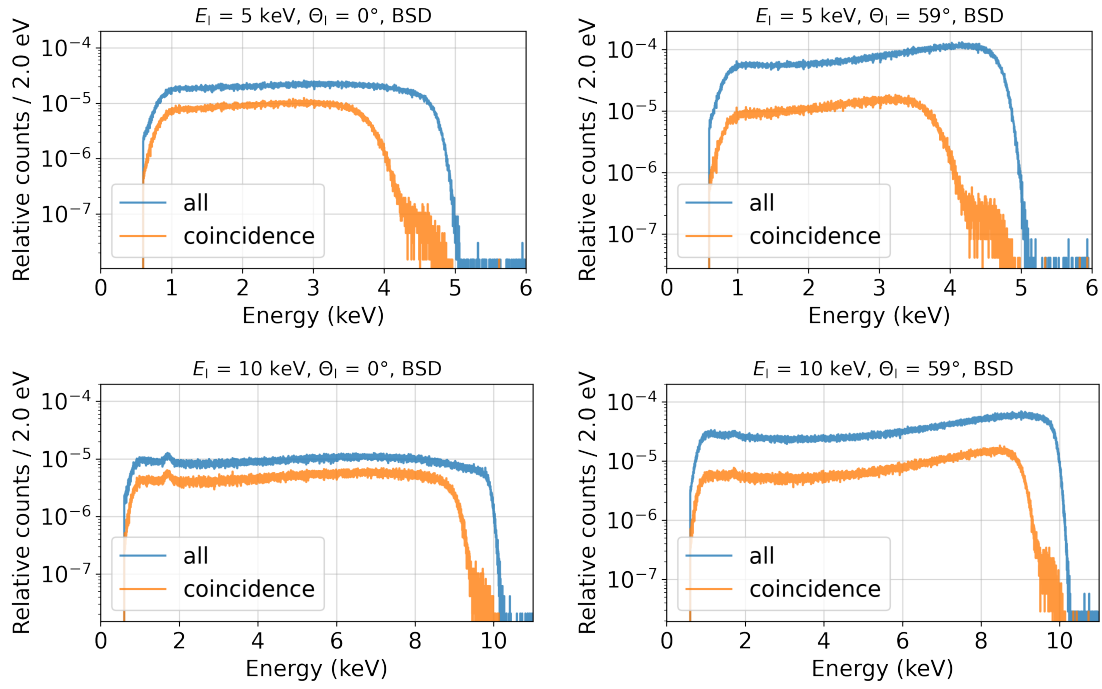


**Figure 5.26: Backscattered Electron Energy Spectra Comparing All Events and Coincidence Events.** The energy spectra from all BSD pixels were combined. The counts per bin are divided by  $\sum_i N_{\text{SOD},i}$  (eq. 5.1). The energy spectrum of the coincidence events is cut off at high energies due to the energy threshold of the SOD. Its amplitude depends on the relative number of initial electrons in the CC pixel. The events at high energies originate from random coincidence.

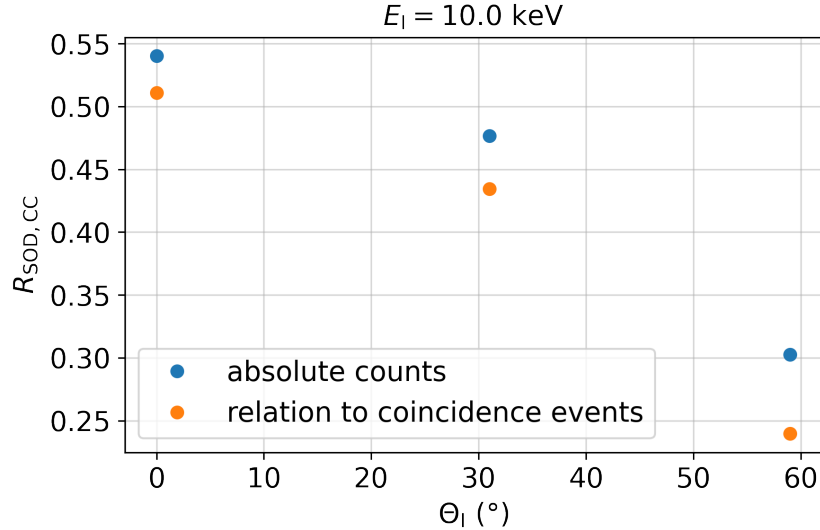


**Figure 5.27: Relative Number of Counts in the CC Pixel as a Function of the Incident Angle at  $E_I = 10 \text{ keV}$ .**  $R_{\text{SOD,CC}}$  is extracted by two means. For the blue data,  $N_{\text{SOD,CC}}$  is divided by the total number of detected initial electrons in the SOD. For the orange data,  $R_{\text{SOD,CC}}$  was estimated from the relation of the energy spectra for all and coincidence events in the BSD between 1 keV and  $E_I - 2 \text{ keV}$ .

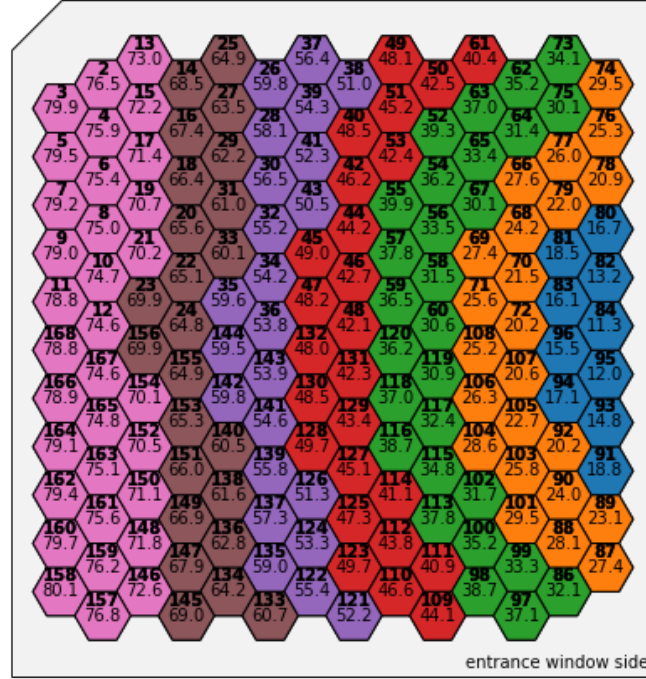


**Figure 5.28: BSD Pixel Grouping by  $\Theta_{BS}$ .** Group 0 (blue):  $0-20^\circ$ , Group 1 (orange):  $20-30^\circ$ , Group 2 (green):  $30-40^\circ$ , Group 3 (red):  $40-50^\circ$ , Group 4 (purple):  $50-60^\circ$ , Group 5 (brown):  $60-70^\circ$ , Group 6 (rose):  $70-90^\circ$ .

So far, only the total energy spectra of backscattered electrons summed over all backscattering angles were investigated. Furthermore, of interest are the energy spectra at different  $\Theta_{BS}$ . For this, the pixels are grouped based on their  $\Theta_{BS}$  as shown in fig. 5.28.

In fig. 5.29, the backscattering electron energy spectra for group 0 and group 5 are opposed comparing different measurement settings. For low  $\Theta_{BS}$ , as in pixel group 0, the spectral shape is very similar for different incident angles and initial electron energies. The spectrum approximately stays constant over the entire energy range. Hence, each electron energy is equally probable. A very similar spectrum shape can also be observed for higher  $\Theta_{BS}$  at  $\Theta_I = 0^\circ$ . At larger  $\Theta_{BS}$ , the spectra differ at large energies. In general, it can be observed that high-energetic backscattering electrons are predominantly backscattered at high  $\Theta_{BS}$ . This effect highly increases for large incident angles. Moreover, the higher the initial electron energy, the more pronounced is the shape distortion at high energies towards higher counts.

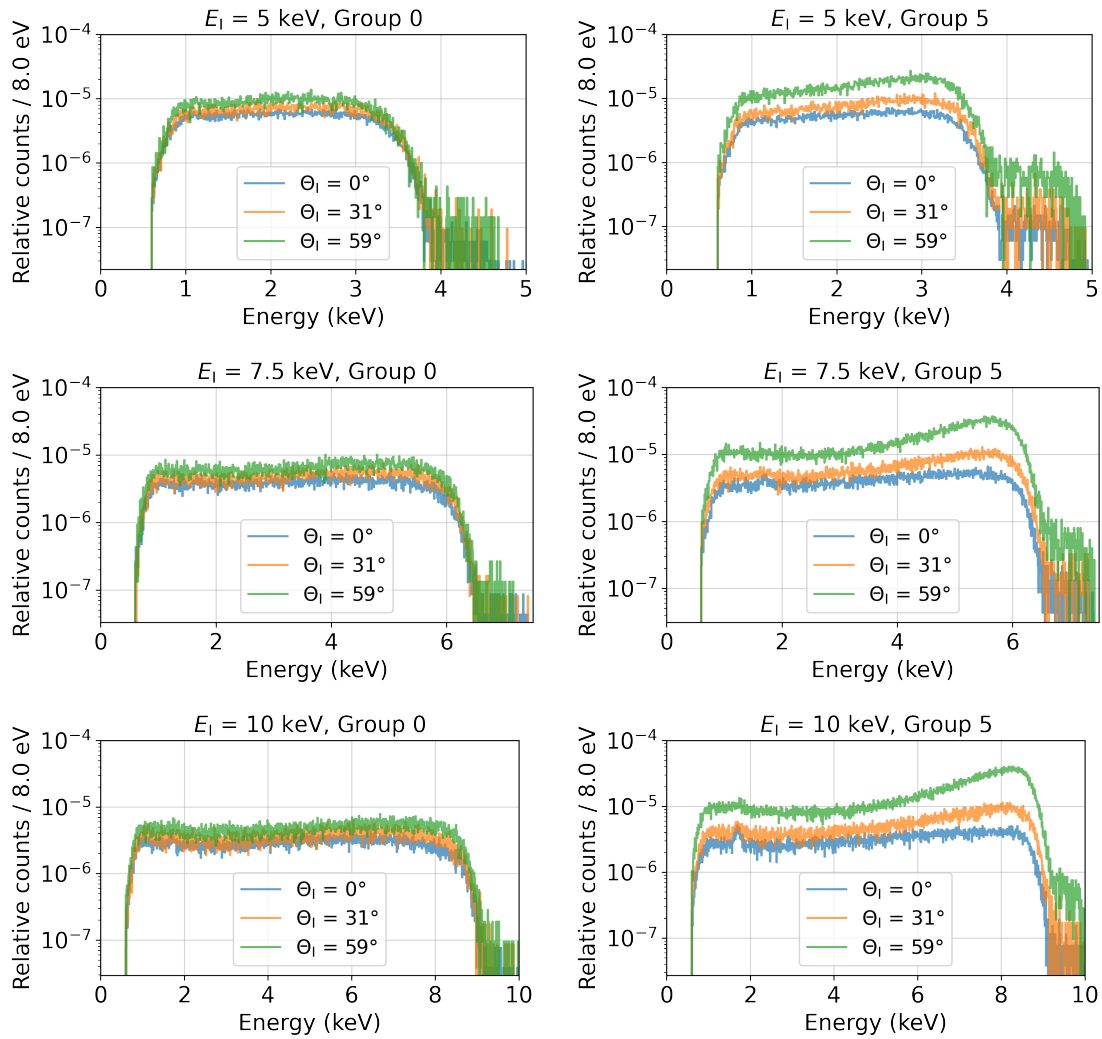


**Figure 5.29: Backscattered Electron Energy Spectra for Pixel Group 0 and 5 Comparing Different Measurement Settings.** The counts per bin are divided by  $N_{\text{SOD,CC}}$  (eq. 5.1). For small  $\Theta_{\text{BS}}$ , the spectra stay approximately constant over the entire energy range. At high  $\Theta_{\text{BS}}$ , the spectrum is distorted at high energies, especially for high incident angles and initial electron energies.

### Angular Distribution

For coincidence events, the absolute number of backscattered electrons per pixel  $j$  of the BSD is defined by:

$$N_{\text{coinc},j} = n_{\text{coinc},j} [E_{\text{SOD}} > E_{\text{SOD,T}} \ \& \ E_{\text{BSD}} > E_{\text{BSD,T}}]. \quad (5.4)$$

Here,  $E_{\text{SOD}}$  is the energy of the event in the SOD, and  $E_{\text{BSD}}$  the energy of the respective coincidence event in the BSD. The number of identified coincidence events for pixel  $j$  of the BSD is denoted by  $n_{\text{coinc},j}$ .

In fig. 5.30 and 5.31,  $N_{\text{coinc}}$  is depicted once for varying incident angle at  $E_{\text{I}} = 10 \text{ keV}$  and once for different initial electron energies at  $\Theta_{\text{I}} = 59^\circ$ . In addition, the difference between  $N_{\text{coinc}}$  and  $N_{\text{BSD}}$  is shown for each setting to compare the angular distribution of backscattered electrons before and after the coincidence cut.

The angular distribution of coincidence events at  $E_{\text{I}} = 10 \text{ keV}$  for different incident angles is very similar to those of all events. It can be seen that for increasing  $\Theta_{\text{I}}$  values the maximum of the distribution is shifted to higher  $\Theta_{\text{BS}}$ . The shape of the distribution remains mainly the same.

The difference in the number of backscattered electrons before and after the coincidence cut in the upper right area of the detector chip is smaller than in the lower left. Besides the CC pixel, the half of the SOD pointing towards the cooling plate was mainly irradiated by the electron beam. As a result, also the lower half of the BSD is more hit by backscattered electrons for the observation of all events. Furthermore, it was already observed that for high incident angles, the backscattered electrons at large  $\Theta_{\text{BS}}$  are predominantly high-energetic. The most high-energetic backscattered electrons cannot be filtered by a coincidence cut, as the respective event in the SOD is below the energy threshold. As a result, the difference in the number of backscattered electrons before and after the coincidence cut is higher at high  $\Theta_{\text{BS}}$ . Moreover, the difference is the highest at low initial electron energies and large incident angles. Here, the relative amount of electrons with energies below the detection threshold of the SOD which cannot be related to an event in the BSD through a coincidence analysis is the highest.

The leftmost two pixel columns in the BSD show a very high discrepancy between all and coincidence events. Those pixels are partly shaded by the PCB board of the SOD and should be excluded for comparisons with simulations.

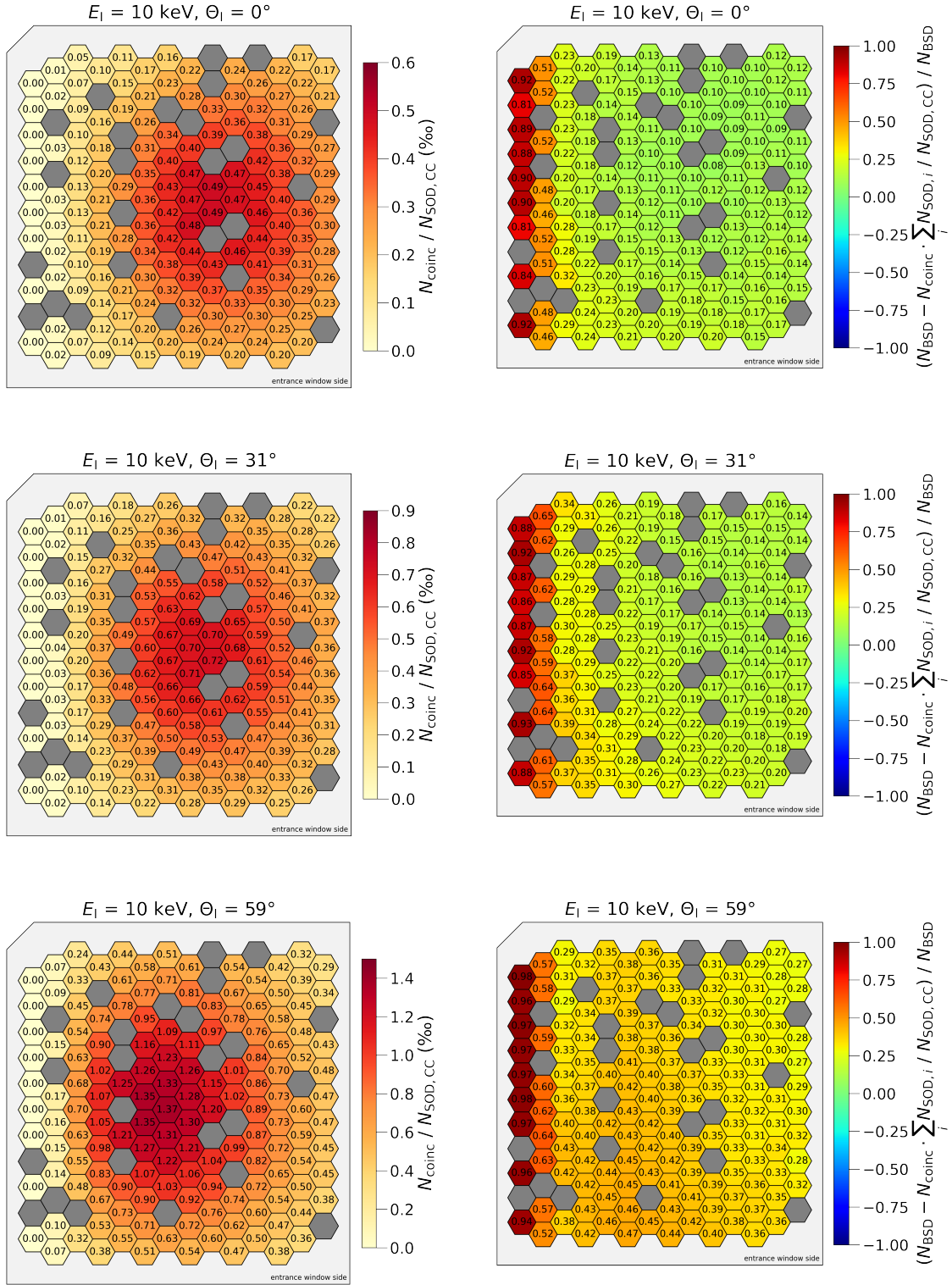


**Figure 5.30:** Number of Backscattered Electrons with Coincidence with the CC Pixel and Difference to  $N_{\text{BSD}}$  for Different  $\Theta_I$ . On the right,  $N_{\text{coinc}}$  is scaled to the relative number of initial electrons in the CC pixel. The difference in the number of backscattered electrons before and after the coincidence cut is higher at high  $\Theta_{\text{BS}}$  and the smallest in the upper right corner of the BSD. The difference is higher at larger  $\Theta_I$ .

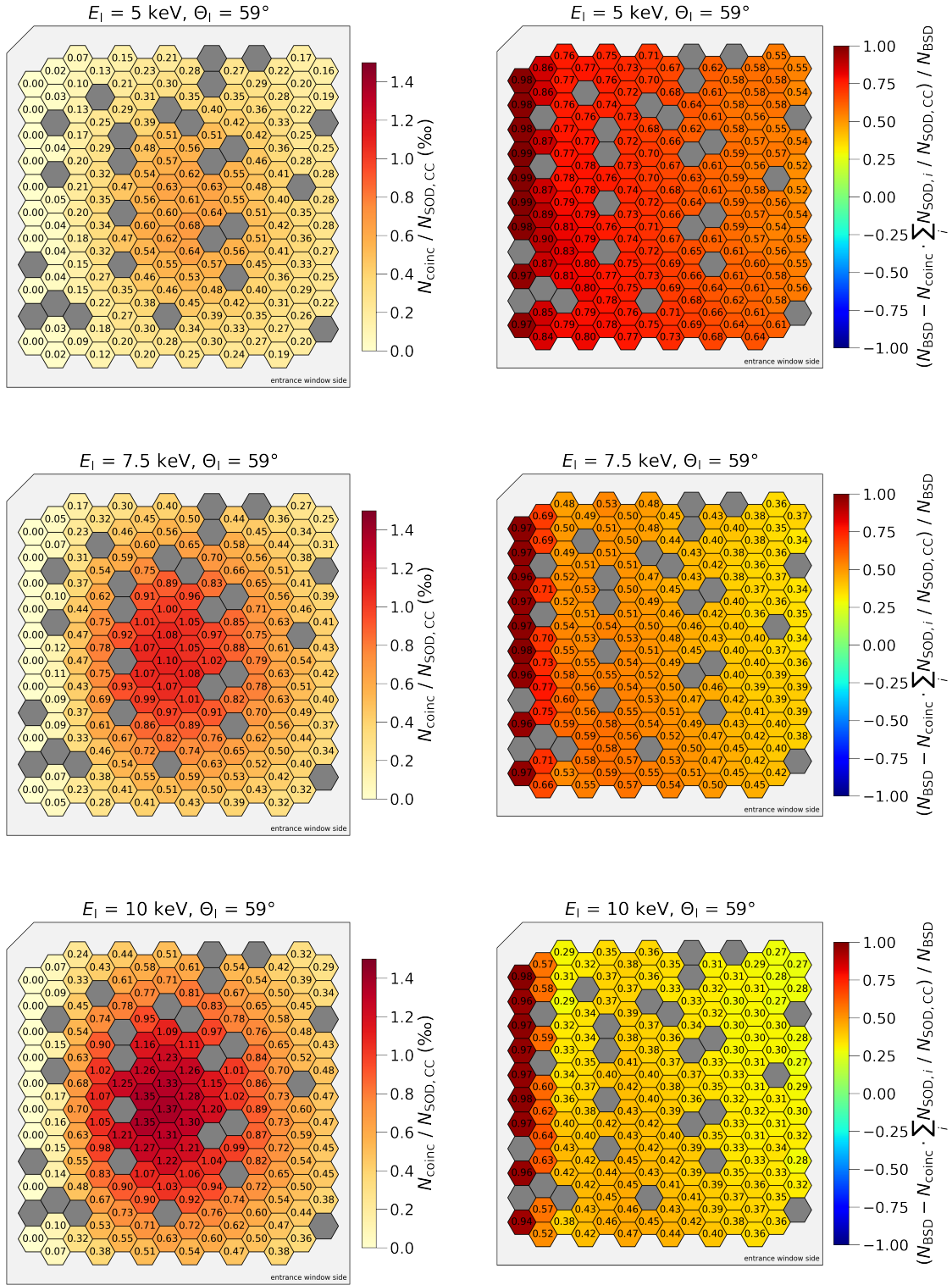


**Figure 5.31:** Number of Backscattered Electrons with Coincidence with the CC Pixel and Difference to  $N_{\text{BSD}}$  for Different  $E_I$ . On the right,  $N_{\text{coinc}}$  is scaled to the relative number of initial electrons in the CC pixel. The difference in the number of backscattered electrons before and after the coincidence cut is higher at high  $\Theta_{\text{BS}}$  and the smallest in the upper right corner of the BSD. The difference is higher at smaller  $E_I$ .

### Backscattering Coefficients

Offsetting the 23% detection efficiency with  $\eta_{\text{exp}} = 4\%$  for  $E_I = 10\text{ keV}$  and  $\Theta_I = 0^\circ$ , a total backscattering coefficient of about 17% can be evaluated. This is in agreement with literature values which state a backscattering coefficient of around 17–21% [69].

The backscattering coefficient can also be calculated for coincidence events as:

$$\eta_{\text{coinc}} = \frac{\sum_j N_{\text{coinc},j}}{N_{\text{SOD,CC}}} \quad (5.5)$$

The resulting coincidence backscattering coefficients can be seen in fig. 5.32 as a function of the incident angle comparing different initial electron energies. An uncertainty of 1.41% on the rate in the CC pixel was assumed. The coefficient shows the same trends as  $\eta_{\text{exp}}$  but a smaller increase with  $\Theta_I$  and a vastly higher decrease with  $E_I$ . Moreover, the coefficients are smaller than  $\eta_{\text{exp}}$ . The difference is due to the energy threshold of the SOD, decreasing the amount of identifiable coincidence events in the BSD especially for low initial energies and high incident angles.

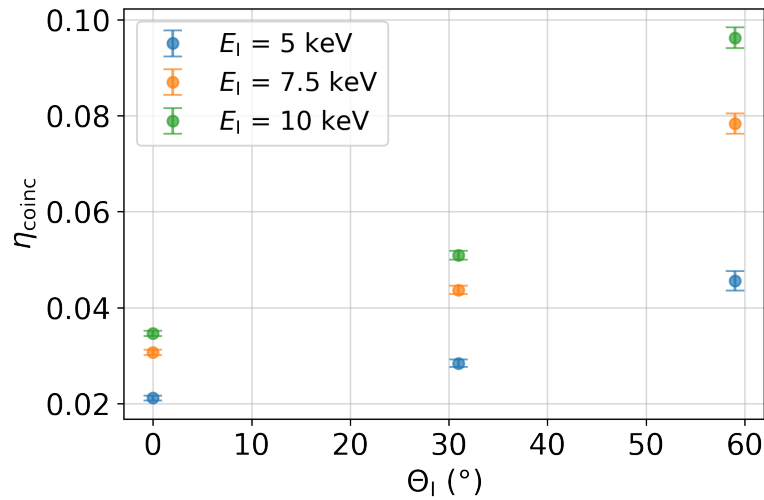


**Figure 5.32: Coincidence Backscattering Coefficient as a Function of the Incident Angle.** An error of 1.41% on the rate in the CC pixel was assumed. The coefficient increases for increasing  $\Theta_I$  and  $E_I$ .

## 5.5 Summary

The BERTA experimental setup was presented, which successfully probed the properties of backscattered electrons and their relations to the initial electron energy and incident angle. The energy spectra of the SOD and BSD were shown for nine configurations of the initial electron energy and the incident angle with and without a coincidence cut. In addition, the angular distribution of the backscattered electrons was investigated. It was observed that high-energetic backscattering electrons are predominantly backscattered at high azimuthal backscattering angles. Moreover, different experimental backscattering coefficients were extracted from the measurements. After an estimation of the backscattering detection efficiency, a total backscattering coefficient of 17% at  $E_I = 10$  keV and  $\Theta_I = 0^\circ$  was calculated. This is in agreement with literature values which state a backscattering coefficient of around 17–21% [69].

Even though all observed relations can be fundamentally understood and are reasonable, a quantitative assessment of the measured values is only possible in comparison with a GEANT4 simulation, which will be described in the following chapter.



# BERTA Simulation with Geant4

GEANT4 (GEometry ANd Tracking) is a toolkit for Monte-Carlo simulations to study the interaction of particles with matter. It offers a wide range of particles, materials and includes different interaction mechanisms. Of major importance for the work presented in this thesis, the toolkit offers the opportunity to study scattering processes of electrons in silicon detectors. In particular, GEANT4 (G4) was used to set up a simulation of the BERTA experiment to investigate the effect of detector backscattering. The implementation of the TRISTAN detectors in the simulation will be presented in section 6.1. An overview of the simulation settings and of the simulated data is provided in section 6.2. All analysis steps required to make the simulation comparable to the measurements are explained in section 6.3. Finally, the simulation results are presented and compared to the measurement results in section 6.4 and chapter 7, respectively.

## 6.1 Simulation Setup

### General G4 Settings

A physics list in G4 is a class which collects all the particles, physics processes and production thresholds needed for the simulation. Since for the observation of backscattering especially single scattering processes are of interest, the `G4EmStandardPhysicsSS` physics list was used for all simulations. The difference to the default physics list is that it does not combine several single scattering processes to one multiple scattering process. A detailed description of the list is given in [80]. A comparison of the simulated electron energy spectra of the SOD for different physics lists can be found in appendix A.1. For the following analyses, no uncertainty on the simulation results was assumed due to a particular choice of a physics list.

Several physics processes have very high cross sections at low energies. Therefore, it is necessary to implement a production cut. All particles with energies below the cut are not generated, but their energy is accounted for as an energy deposition inside the detector. In the simulations, the production cut was set to 100 eV. Below about this value, the physics models implemented in G4 are not validated to work appropriately. Hence, for lower production cuts, G4 simulations can only be used for qualitative studies.

### Detector and Experimental Setup Simulation

The experimental setup in the simulation is implemented in a simplified way. Two silicon detectors are situated in a world sphere of 0.5 m radius. A vacuum environment was

simulated with the `G4-Galactic` material, providing a gas pressure of  $3 \cdot 10^{-20}$  mbar. Hence, the pressure is much lower than in the experiment. Nonetheless, for the distances the electrons have to travel in the setup, this difference has no notable effect on the results.

Both detectors (shoot-on detector SOD and backscattering detector BSD) are implemented in the simulation and oriented in the same manner as in the experiment, see fig. 6.1. For simplicity, only the single pixels are simulated without any holding structures or readout electronics. One pixel is defined as a hexagon with a thickness of  $450 \mu\text{m}$  and a diameter of  $2.856 \text{ mm}$ . The first  $10 \text{ nm}$  of the entrance window are implemented as a silicon dioxide layer, while the rest of the detector consists of pure silicon, cf. chapter 4. No doping profiles or drift fields inside the pixels are simulated. A detailed study on the charge drift for TRISTAN SDDs can be found in [79].

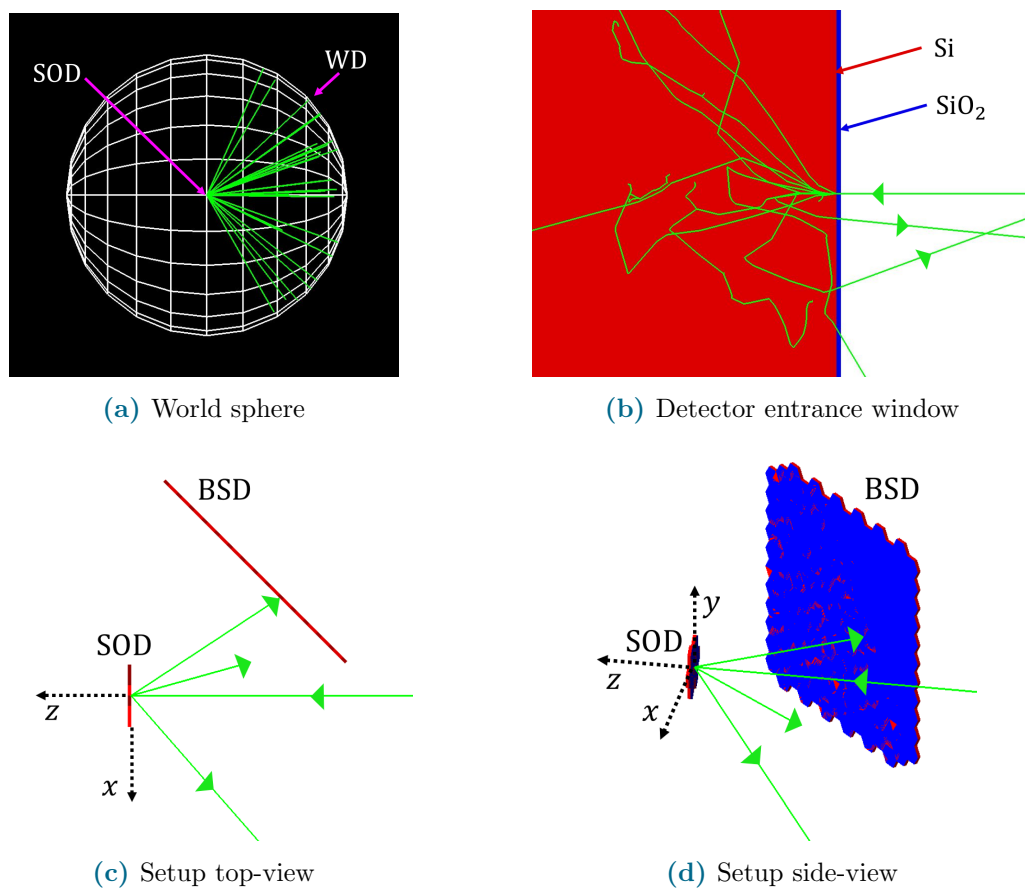


**Figure 6.1: Simulation Setup.** The setup is located in a spherical volume as shown in (a). An electron beam (green) is directed in  $z$ -direction towards the center of the SOD. The pixels consist of a  $10 \text{ nm}$ -thick silicon-dioxide layer (blue) at the entrance window side and a silicon bulk (red), see (b). Only the actual pixels were simulated, the surrounding structures were neglected. The SOD and BSD are arranged as in the experiment with the same relative distance and angle. The backscattered electrons, if not detected by the BSD, are stopped when they leave the world sphere. The coordinate system is indicated in figure (c) and (d).

A mono-energetic electron source without angular spread was implemented. It is situated 10 cm from the SOD and points towards the center of the SOD. In the simulation, the production and acceleration mechanism of the electrons has been neglected. Moreover, the electron gun itself has not been implemented.

Finally, other setup components such as the vacuum chamber, the module shielding, the front-end boards, the copper holding structure, the steering coils, etc. have not been simulated. Their impact on the recorded electron energy spectra and the angular distribution of backscattered electrons on the BSD is assumed to be negligible.

## 6.2 Simulation Settings

For each generated electron, the energy deposition in every pixel of the SOD and BSD is recorded. The total energy deposition per pixel is the sum of each single energy deposition inside the pixel volume. To account for incomplete charge collection at the entrance window, each energy deposition is weighted by the charge collection efficiency calculated according to eq. 4.5.

For every event, an event number is stored. First, every generated electron gets an event number. Secondary electrons obtain the same event number as their mother electrons. Hence, just as in the experiment, no differentiation between a backscattered initial electron and backscattered secondary electron is possible in the BSD. The event number can be used to filter coincidence between the SOD and BSD in the simulation.

If a backscattered electron leaves the world sphere, its tracking is stopped. The energy of the electron as well as the  $(x, y, z)$ -coordinates of its border crossing are recorded. Therefore, the world sphere serves as an additional detector, in the following referred to as the world detector (WD).

The SOD and BSD are implemented in such a way that the electron energy spectra can be recorded with and without a silicon-dioxide layer at the detector surface. This makes it possible to observe the impact of the silicon-dioxide layer on backscattering by comparing simulations with and without the layer. Moreover, the effect of incomplete charge collection can be studied by adjusting or switching off the transition layer model. In addition, simulations can be executed without the BSD. With only the WD being active, it is possible to observe all backscattered electrons, their energies as well as the angular distribution.

For reasons of comparability with the experimental investigations, all nine measurement configurations were simulated with the respective initial energies and incident angles. For each run,  $N_{\text{in}} = 10$  million electrons were generated. This is approximately in the order of number of electrons measured in the CC pixel in the experiment per measurement setting. Each simulation was repeated without the BSD to investigate the entire backscattering spectrum and distribution. In addition, for the initial energies  $E_{\text{I}} = 5 \text{ keV}$  and  $E_{\text{I}} = 10 \text{ keV}$  at  $\Theta_{\text{I}} = 0^\circ$ , simulations without the transition layer model and without a silicon-dioxide entrance window were performed.

## 6.3 Data Processing

Due to the simplicity of the implemented detection system in G4, several data processing steps have to be done to allow for a comparison between the simulated and experimental data. In subsection 6.3.1, the analysis procedure taken for the experimental data analysis (sec. 5.3) is discussed. Additionally, the detector-dependent CCE parameters need to be evaluated. Furthermore, effects such as electronic noise and statistical fluctuations in the charge production process have to be taken into account. Therefore, in subsection 6.3.2, the method to fit the simulated to the experimental data to extract all needed parameters for an effective detector model is explained.

### 6.3.1 Comparability of Simulations and Measurements

**Energy Calibration** An energy calibration of the simulated detector system is not required. Only the energy depositions of electrons in silicon are simulated. The charge carrier production mechanism in the SDD as well as the detector readout chain and the DAQ system have been neglected in the simulations. Therefore, the system can be regarded as perfectly calibrated. An uncertainty on the calibration of the experimental data is accounted for by the introduction of a gain and an offset in the simulated data as explained in the following subsection.

**Charge Sharing** The effect of charge sharing is not present in the simulation in the SOD. This is due to the fact that the simulated electron beam has no angular spread and therefore solely hits the central pixel of the SOD. Assuming that almost all charge sharing events in the experiment are rejected by the charge sharing cut, see section 5.3.2, the simulated and experimental energy spectra of the SOD are comparable in terms of charge sharing effects. The number of detected initial electrons does not need to be corrected for charge sharing in the simulation. For the BSD, charge sharing effects in the simulation have been neglected just as in the experiment.

**Pileup** Since no DAQ system and thus no energy reconstruction filter such as a trapezoidal filter was taken into account in the simulation, no pileup events are present in the simulated data. The number of pileup events in the SOD are small at the low electron rates in the order of 1–7 kcps (see section 5.3.3) in the experiment. Therefore, in the scope of this work, no pileup correction was applied to the simulated data. The uncertainty arising from this simplification was assumed to be small and was therefore neglected in the further analysis. Additionally, the number of detected initial electrons does not need to be corrected for pileup in the simulation due to this simplification.

**Coincidence** As opposed to the measurements (see section 5.3.5), coincidence events in the simulation are not identified via a coincidence time window of a chosen length. Instead, the event number of each electron is used. Additionally, the same energy thresholds have to be applied for the experiment and the simulation. In the simulation, there is no energy threshold, but in the experiment, there is one due to the DAQ system. Some artificial

energy thresholds were set above the actual energy threshold from the DAQ system in the experiment. Since the overall electronic noise is higher in the BSD in the experiment, the threshold for the BSD had to be set higher than in the SOD. As a result, for an event in the SOD, the corresponding event in the BSD has to have an energy  $E_{\text{BSD}}$  larger than  $E_{\text{BSD,T}} = 1 \text{ keV}$ . For an event in the BSD, the same applies vice versa with  $E_{\text{SOD,T}} = 0.8 \text{ keV}$ .

### 6.3.2 Heuristic Detector Model

In general, for every experimental setup and SDD, the electronic noise contribution  $c_{\text{el}}$  (eq. 4.3) to the energy resolution is different. Theoretically,  $c_{\text{el}}$  could be extracted from the energy resolutions evaluated from the  $^{55}\text{Fe}$  calibration measurement. Nevertheless, first investigations showed that those extracted  $c_{\text{el}}$  values are too small to explain the observed electron energy spectrum with simulations. Additionally, the charge collection efficiency can vary from detector to detector as it depends on the doping profile of the SDD. As a result, the simulated electron energy spectrum detected in the CC pixel was fitted to the experimental one to determine the CCE parameters and  $c_{\text{el}}$  for the detector used in the experiment. The Nelder-Mead method was used to minimise the reduced chi-square parameter. After having determined the CCE and  $c_{\text{el}}$  parameters, they can be implemented in later simulations or rather applied on the simulated data to compare the measurements and simulations with regards to backscattering.

The following steps were taken:

1. Implementation of a simplified setup geometry for the fitting procedure.
2. Fit of the simulated data to the experimental energy spectrum of the CC pixel to determine the CCE model parameters for each measurement setting.
3. Implementation of the CCE model parameters in the default simulation.
4. Fit of the simulated data to the experimental energy spectrum of the CC pixel to determine the remaining detector model parameters for each measurement setting.

In the following, each step will be explained in more detail.

#### 1. Simplified Simulation Setup Geometry

For the fit, a separate simulation setup was implemented in G4. Specifically, only the central pixel of the SOD was simulated for the electron detection. Here, the pixel consists of thirty 10 nm-thick layers at the entrance window side and a 449.7  $\mu\text{m}$ -thick detector bulk. The first layer at the detector surface consists of silicon-dioxide. The remaining layers and the detector bulk are composed of pure silicon. An illustration of the pixel structure is shown in fig. 6.2. For every single layer as well as for the detector bulk, each single energy deposition per interaction is summed up. Hence, for one incoming electron, thirty-one summed energy depositions are recorded. This setup configuration was chosen following the fit procedure presented in [63].

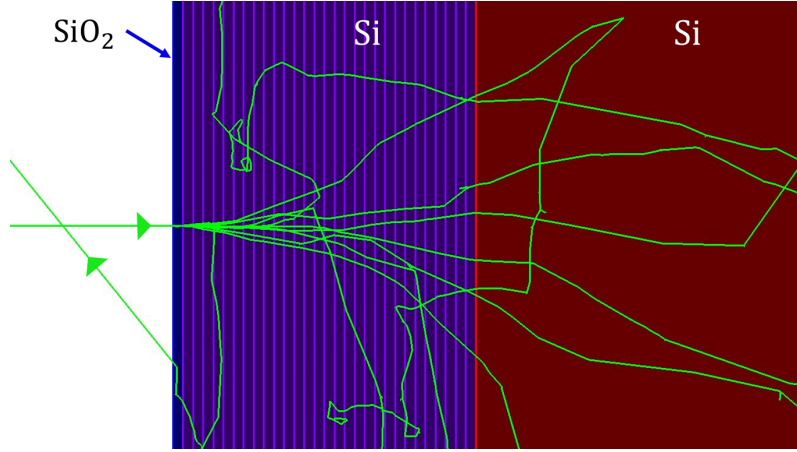


**Figure 6.2: Detector Segmentation for a CCE Model Fit.** The pixel detector consists of a 10 nm-thick silicon-dioxide layer (blue) at the entrance window side followed by 29 10 nm-thick silicon layers (purple) and a 449.7  $\mu\text{m}$  thick silicon bulk (red). The single energy depositions of an incoming electron (green) are summed for each detector segment. For this illustration, ten initial electrons with  $E_I = 10$  keV were simulated.

## 2. Fitting Procedure

Seven fit parameters were defined to obtain the desired energy spectrum  $H_{\text{sim}}$  of the SOD in the following steps:

1. CCE parameters ( $DL$ ,  $p_1$  and  $\lambda$ ) as defined in eq. 4.5: The total energy deposition  $E_{\text{tot}}$  in the detector per electron is the sum of all energy depositions  $E_i$  in the layers and in the detector bulk  $E_{\text{bulk}}$ :

$$E_{\text{tot}} = \sum_{i=0}^{29} E_i \cdot w_i + E_{\text{bulk}}. \quad (6.1)$$

The energy depositions in the layers are weighted by the mean CCE  $w_i$  of the respective layer  $i$ . The detector surface is situated at  $z = 0$  nm.

2. Calibration parameters (gain  $g$  and offset  $o$ ): No DAQ system was included in the simulation, and therefore no energy calibration was required. In the experiment, the detector was calibrated with an  $^{55}\text{Fe}$  source (see section 5.3.1). To account for possible uncertainties of the calibration in the experiment,  $E_{\text{tot}}$  in the simulation is multiplied by a gain  $g$ , and an offset  $o$  is added:

$$E_{\text{calib}} = g \cdot E_{\text{tot}} + o. \quad (6.2)$$

3. Electronic noise parameter ( $c_{\text{el}}$ ) as defined in eq. 4.3: Electronic noise from the readout chain and statistical fluctuations in the charge production process are not simulated in G4. Therefore, a random sample  $X$  from a normal distribution with a Gaussian width  $\sigma_{\text{Fano+Noise}}$  is added to every energy deposition. This gives the detected energy deposition  $E_{\text{det}}$ :

$$E_{\text{det}} = E_{\text{calib}} + X. \quad (6.3)$$

**Table 6.1: Fit Parameter Start Values and Bounds.** For the CCE, calibration, electronic and electron number parameters, the start value for the fit as well as the upper and lower bound of the parameter range are listed.

Fit parameter	Start value	Lower bound	Upper bound
$DL$	10 nm	0 nm	$\infty$
$\lambda$	70 nm	0.0001 nm	$\infty$
$p_1$	0.85	0.0	1.0
$g$	1.01	0.8	1.2
$o$	-0.1 keV	-2 keV	2 keV
$c_{el}$	80 eV	0 eV	$\infty$
$A$	2	0	$\infty$

4. Electron number parameter (amplitude  $A$ ): The electron energy spectrum  $H_{sim}$  can be obtained with the detected electron energies  $E_{det}$ . For this, the same binning as the experimental energy spectrum has to be used to be able to compare the counts per energy region which is defined by one bin. Since the total amount of generated electrons in the experiment and the simulation differ, the spectrum of the simulation is scaled with an amplitude  $A$  yielding an effective spectrum  $H_{eff}$ :

$$H_{eff} = A \cdot H_{sim}. \quad (6.4)$$

The start value as well as the lower and upper boundary for each parameter are listed in table 6.1. The start values were defined based on the results of a preceding grid search and a visual comparison of the experimental and simulated data.

The fit is designed to minimise the reduced chi-square:

$$\chi_{red}^2 = \frac{\chi^2}{B - dof} \quad (6.5)$$

with  $dof$  being the number of free parameters and  $B$  the number of bins. The parameter  $\chi^2$  is defined as:

$$\chi^2 = \sum_i^B \frac{H_{exp,i} - A \cdot H_{sim,i}}{A \cdot \sqrt{H_{sim,i}}} \quad (6.6)$$

with  $H_i$  the number of counts per bin  $i$ . The experimental electron energy spectrum measured in the central pixel of the SOD after the charge sharing cut is denoted by  $H_{exp}$ . Since only the experiment is subject to an energy threshold and pileup effects related to the DAQ system, the spectra are only compared for energies  $E > E_{SOD,T}$  and  $E < (E_I + 0.2 \text{ eV})$ .

### 3. CCE Model Implementation

First, a fit with all seven fit parameters was performed with a simulation for each  $E_I/\Theta_I$  setting in the experiment. For this, the simulated data were processed as explained above and the resulting simulated energy spectrum was compared to the experimental energy

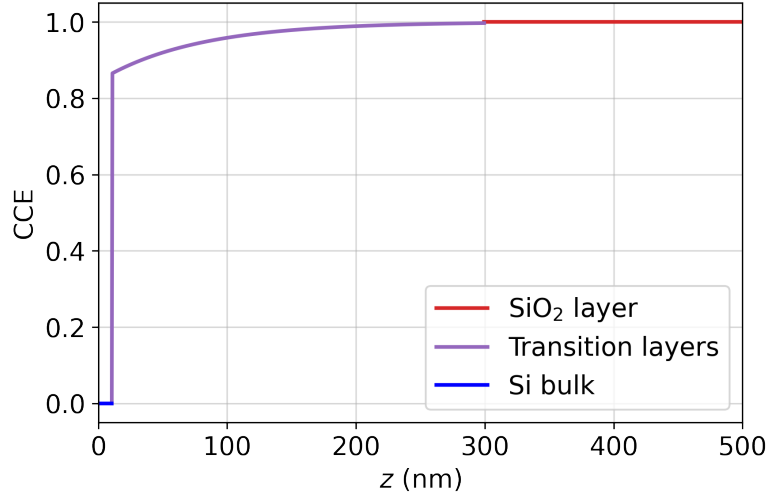


**Figure 6.3: Mean Charge Collection Efficiency.** The mean CCE parameters are  $DL = 10.7$  nm,  $p_1 = 85.6\%$  and  $\lambda = 75.7$  nm. In the plot, the color-code shows the detector areas as defined in fig. 6.2.

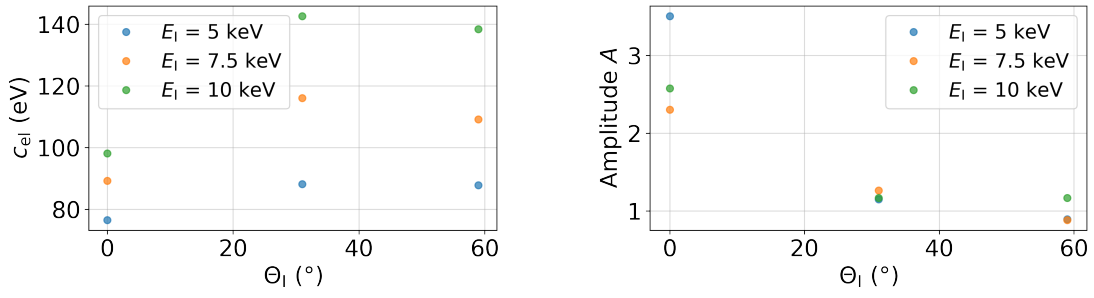
spectrum of the CC pixel after the charge sharing cut. By means of the Nelder-Mead method, the reduced chi-square was minimised.

The parameters  $DL$ ,  $p_1$ ,  $\lambda$  and  $c_{el}$  are only dependent on the doping profile of the detector and on the noise performance of the readout chain in the experiment, but not on  $E_I$  or  $\Theta_I$ . Unfortunately, the fits did not converge, i.e. no set of CCE parameters could be determined. Therefore, a further investigation and development of the CCE model e.g. via a crosscheck with other TRISTAN detectors is necessary.

In the scope of this work, the mean values of all nine fits for the CCE parameters were calculated. A mean dead layer thickness of  $10.7^{+2.8}_{-6.7}$  nm was evaluated. This is in agreement with a design value of 8–10 nm for the thickness of the silicon-dioxide layer. The mean detection efficiency behind the dead layer is about  $85.6^{+4.2}_{-9.1}\%$  and the mean effective transition layer thickness is  $75.7^{+25.1}_{-26.2}$  nm. The resulting CCE can be seen in fig. 6.3. The CCE model is for the following analysis implemented in the default simulation setup without segmented energy depositions in layers. Therefore, the energy depositions are now weighted by the CCE model and summed to  $E_{tot}$  within the simulation.

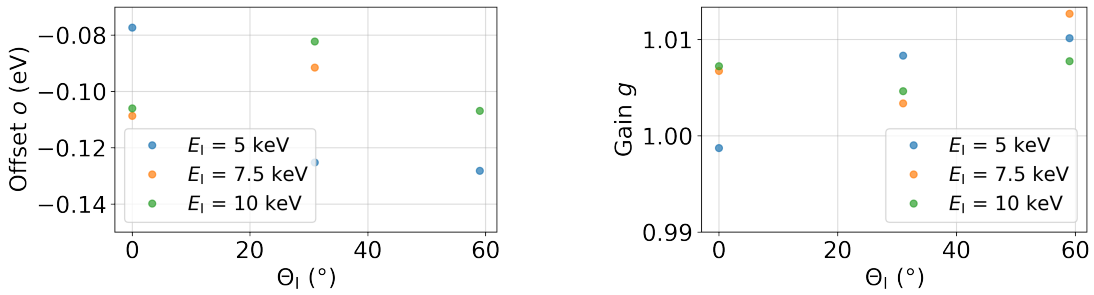
#### 4. Final Fit Results

A second set of simulations was performed with the CCE model implemented in the default simulation setup. A new fit was performed without the summation of the weighted energy depositions, as it is now done within the simulation. The energies  $E_{tot}$  simulated in the CC pixel were compared to the experimental energy spectrum of the CC pixel after the charge sharing cut. For the remaining four fit parameters, the same start values and parameter bounds as in the first fit round were applied. The fit results for each parameter and every  $E_I/\Theta_I$  setting are shown in fig. 6.4.



(a) The noise parameter is up to three times higher than expected from an  $^{55}\text{Fe}$  calibration measurement, especially at higher  $E_I$  and  $\Theta_I$ .

(b) The amplitude decreases with increasing  $\Theta_I$ . It correlates with the count rates and the effective measurement time in the experiment.



(c) The offset parameter is negative, therefore the main peak in the simulation was originally detected at higher energies than in the experiment.

(d) The gain parameter is (almost) always slightly above 1. Therefore, the simulated spectra were stretched to fit to the experimental ones.

**Figure 6.4: Fit Parameter Results.** The results for the four remaining fit parameters are depicted as a function of the incident angle and for the different initial electron energies. The mean CCE parameters were implemented within the default simulation.

It should be noted that the results for  $c_{el}$  are not in agreement with the  $^{55}\text{Fe}$  calibration, from which a value of  $c_{el} \approx 52$  eV is expected. The fit results show up to three times higher values and also large variations of  $c_{el}$ , although it is predicted to stay constant for all measurement settings. Here,  $c_{el}$  is higher for higher incident angles and initial energies. This indicates that the deployed CCE model is not fully suitable. As a result, the applied data processing can only be regarded as an effective model for the detector.

Despite the shortcomings mentioned above, a reasonable agreement of the fitted simulated data and the experimental data was achieved. A comparison of both energy spectra is shown in fig. 6.5 exemplary for the initial energies  $E_I = 5$  keV and  $E_I = 10$  keV at zero incidence ( $\Theta_I = 0^\circ$ ). The spectra comparison of the energy spectra for the remaining values of  $\Theta_I$  and  $E_I$  are shown in appendix A.2.

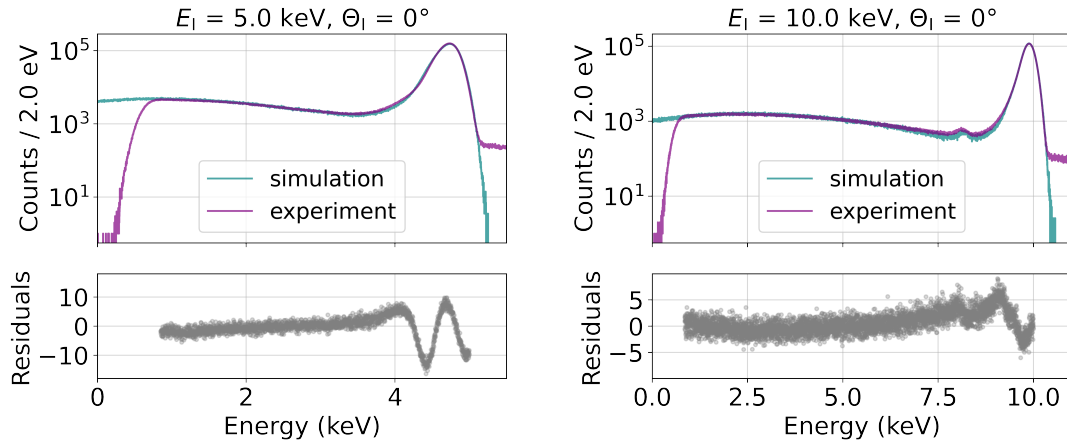


**Figure 6.5: Comparison of Simulated and Measured Energy Spectra of the CC Pixel.** The simulated fitted energy spectra are compared to the experimental energy spectra for  $E_I = 5$  keV and  $E_I = 10$  keV at  $\Theta_I = 0^\circ$ . The residuals are calculated for energies between  $E_{\text{SOD,T}}$  and  $E_I + 0.2$  eV. Some structures in the residuals at high energies hint towards a not fully suitable detector model. In total, good spectral agreement was achieved.

Fig. 6.6 shows the  $\chi_{\text{red}}^2$  for the different parameter settings. A  $\chi_{\text{red}}^2$  of 1 is aimed for. For values  $< 1$ , the model is too complex. For values  $\gg 1$ , the model is inappropriate to describe the data. With values of  $\chi_{\text{red}}^2 < 20$ , the defined effective detector model is therefore well-suited to describe the experimental energy spectra of the SOD, and therefore, for the investigation of backscattering. Overall, the spectral shape is best reproducible for higher  $E_I$  values. For  $E_I = 5$  keV where the transition layer has a strong impact on the electron spectrum, the fit showed the poorest performance.

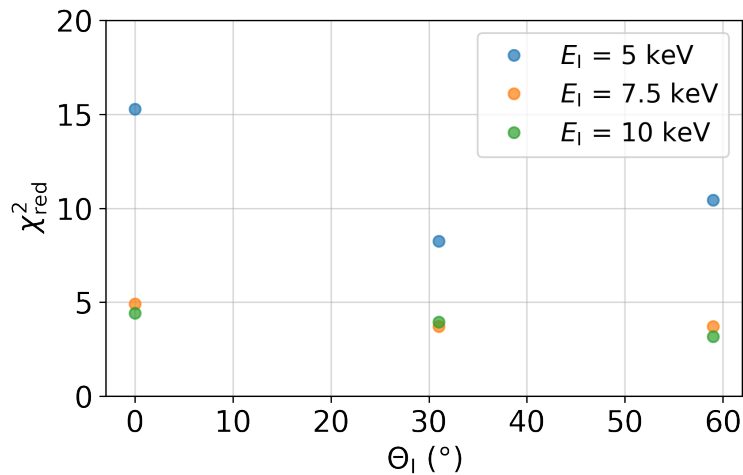


**Figure 6.6: Fit Performance in Terms of  $\chi_{\text{red}}^2$ .** The best fit performance was achieved for  $E_I = 7.5$  keV and  $E_I = 10$  keV with  $\chi_{\text{red}}^2 < 5$ . With in total  $\chi_{\text{red}}^2 < 20$ , the effective detector model is well-suited to describe the experimental data.

---

For the following investigations, the fit parameters will also be used for the energy spectra of the BSD. Since both detector chips are produced in the same manner with reproducible doping profiles, the CCE parameters should not change for the BSD. In addition, the BSD was calibrated in the same measurement as the SOD. Therefore, the calibration parameters should not need to be modified. The count rate in the BSD scales with the count rate in the SOD. Consequently, there is also no reason for the amplitude to vary. The electronic noise parameter for the BSD should be higher compared to the SOD as observed in the energy resolution extracted from the calibration measurement with an  $^{55}\text{Fe}$  source. Nonetheless, the BSD observes a continuous energy spectrum, therefore electronic noise does not have such a prominent effect on the spectral shapes as in the SOD. Furthermore, the applied data procedures are only an effective detector model. As a result, to first approximation, the detector model is assumed to be identical for every pixel in the setup. The uncertainty this simplification introduces is assumed to be small and therefore neglected in the comparison of experiment and simulation.

## 6.4 Simulation Results

### Energy Spectra

The simulated energy spectra of the CC pixel of the SOD for  $E_I = 5$  keV and  $E_I = 10$  keV at  $\Theta_I = 0^\circ$  are shown in fig. 6.7. To illustrate the effect of the silicon-dioxide layer, the CCE and the noise, they are included successively.

If the detector only consists of a pure silicon bulk, the main peak and the silicon escape peak are delta-shaped. In addition, the energy spectrum also shows a small peak close to 0 keV arising from elastically backscattered electrons. It is not detectable in the experiment due to the energy threshold and electronic noise. The introduction of a silicon-dioxide layer only leads to small changes close to the main peak. A small peak at about 0.5 keV below the initial electron energy arises from the ionisation of oxygen atoms. Photons emitted during the rearrangement of the electron shell leave the detector. For oxygen, the photon emitted from the  $K_\alpha$  transition has an energy of 0.525 keV [65].

After introducing the CCE model according to eq. 4.5 and the fit results in section 6.3.2, the peaks have now a large tail towards lower energies. For an initial energy of  $E_I = 5$  keV, the introduction of a not fully sensitive transition layer suffices to wash out the silicon escape peak as well as the peak arising from oxygen ionisation. The introduction of electronic noise according to eq. 4.3 and the fit results in section 6.3.2 leads to a normally-distributed main and silicon escape peak with a transition layer shoulder. The backscattering tail mainly remains unaffected when the CCE and noise models are included. Only the part of the backscattering tail close to the initial electron energy is affected since it overlaps with the transition layer shoulder.

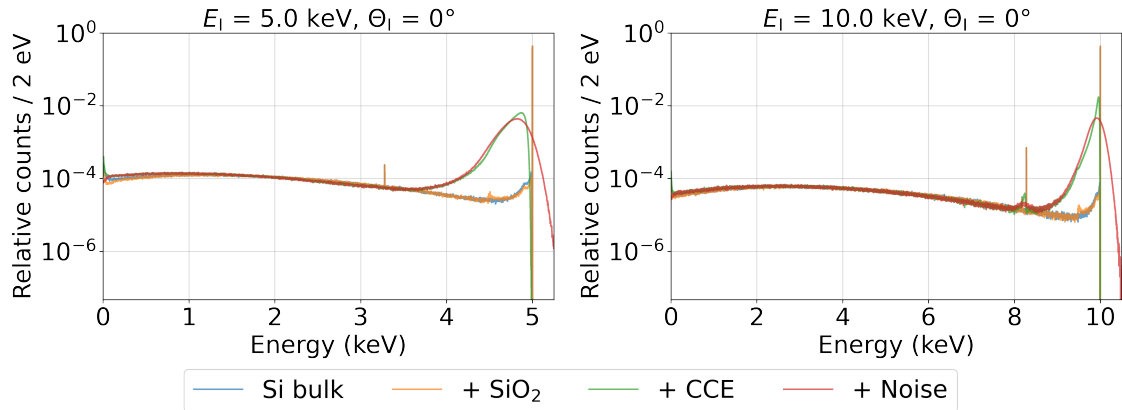


**Figure 6.7: Simulated Energy Spectra of the CC Pixel.** The counts per bin are divided by the number of initially generated electrons. The main peak at about  $E_I$ , the silicon escape peak at  $E_I - 1.74$  keV and the elastic backscattering peak close to 0 keV are visible. As soon as the CCE model and the noise model are included, the delta-shaped peaks are normally-distributed and have a transition layer shoulder. The backscattering tail is mainly unaffected by the inclusion of CCE and noise effects besides in the region where it overlaps with the transition layer shoulder.

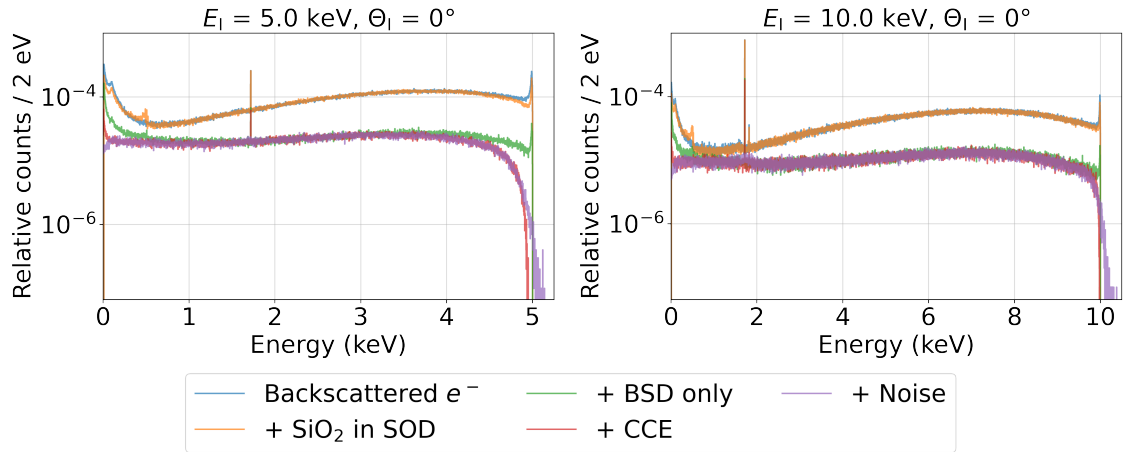


**Figure 6.8: Simulated Energy Spectra of the Backscattered Electrons.** The counts per bin are divided by the number of generated electrons. The secondary electron peak at low energies, the  $K_\alpha$  peak of silicon at 1.74 keV and the elastic backscattering peak close to the initial electron energy are visible. The introduction of the spatially-limited BSD detector lowers the backscattering continuum and flattens the spectrum. If the CCE model and noise model are included, the peaks are mostly washed out and the spectral shape close to the endpoint is altered.

Fig. 6.8 shows the respective simulated energy spectra of the backscattered electrons. Detecting all backscattered electrons with the WD provides the opportunity to observe a peak at the initial electron energy. It corresponds to electrons which are reflected at the SOD detector surface, losing hardly any energy. Photon peaks from the  $K_\alpha$  transition of silicon and oxygen are visible. For an initial energy of  $E_1 = 10 \text{ keV}$ , also a photon peak from the  $K_\beta$  transition of silicon at 1.84 keV becomes observable [65]. Due to the small intensity of this peak and its proximity to the  $K_\alpha$  peak of silicon at 1.74 keV, it is not resolvable in experiments. Moreover, an increase in the number of counts towards smaller energies due to the detection of many low-energetic secondary electrons is visible.

The introduction of the BSD detector lowers the backscattering continuum due to its limited spatial coverage. Furthermore, the spectrum is flattened, particularly at higher energies. The inclusion of a CCE almost washes out the peak from secondary electrons. Furthermore, it alters the spectral shape at the endpoint, especially for electrons with lower initial energy. The elastic backscattering peak is not visible anymore. The photon peaks are hardly affected by the transition layer due to the point-like interaction of photons in matter. Electronic noise further alters the spectrum at very low and very high energies and broadens the photon peaks or even washes them out for low  $E_1$ .

Nonetheless, the introduction of a CCE model and electronic noise only has a small effect on the energy spectrum. Since the experiment has an energy detection threshold, effects of the CCE and noise on low-energetic backscattered electrons are not observable. Only at high energies, differences between the fitted CCE in the SOD and the actual CCE in the BSD would be visible to a very small extent.

### Angular Distribution

Using the WD and no BSD, the total angular distribution of all backscattered electrons can be observed. Fig. 6.9 shows the number of backscattered electrons  $N_{\text{out}}$  per solid angle  $\Omega$  for different  $\Theta_I$  at  $E_I = 10$  keV.

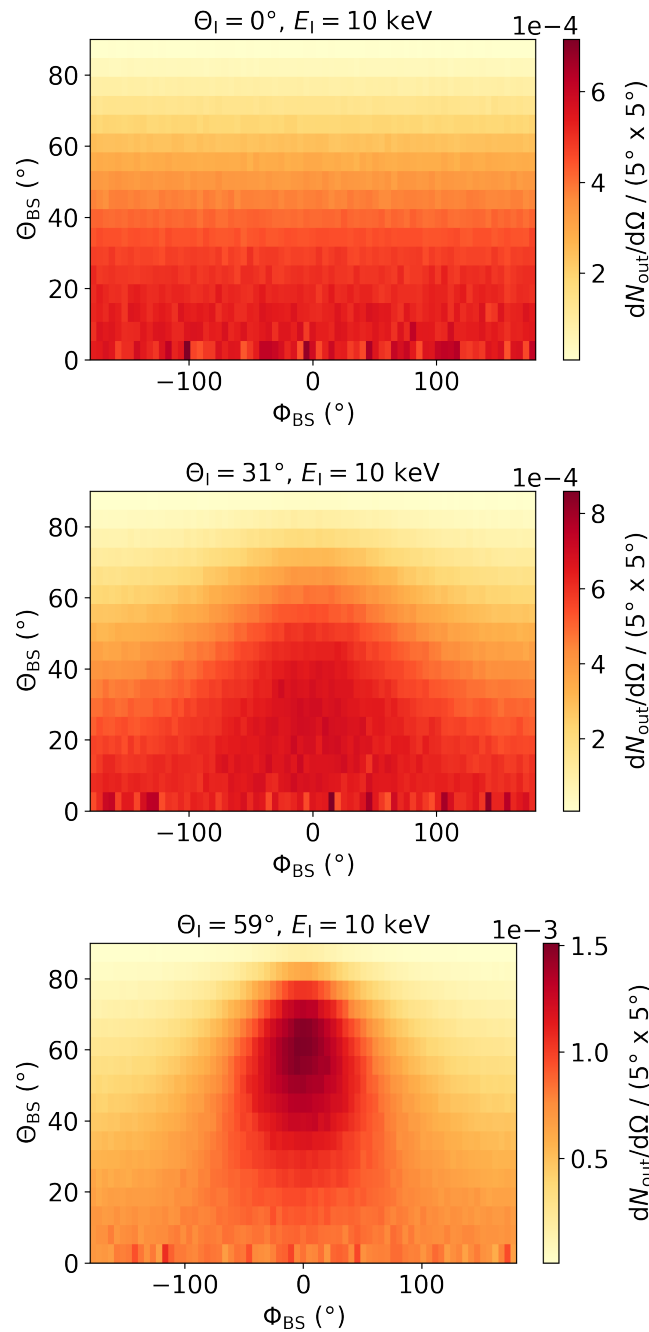


**Figure 6.9: Number of Simulated Backscattered Electrons per Solid Angle.**

The numbers are scaled to the number of initially generated electrons. For higher incident angles, the electrons are increasingly concentrated towards  $\phi_{\text{BS}} = 0^\circ$  and  $\Theta_{\text{BS}} \approx \Theta_I$ . The distributions are symmetric around  $\phi_{\text{BS}} = 0^\circ$ .

Here, the angle  $\Omega$  is defined as:

$$\Omega = \sin \Theta_{\text{BS}} \, d\Theta_{\text{BS}} \, d\phi_{\text{BS}}. \quad (6.7)$$

For  $\Theta_{\text{I}} = 0^\circ$ , the electrons are preferably backscattered to low values of  $\Theta_{\text{BS}}$ . The number of backscattered electrons continuously decreases towards higher  $\Theta_{\text{BS}}$ . The electrons are evenly distributed in  $\phi_{\text{BS}}$  direction. For higher incident angles, the electrons are increasingly concentrated towards  $\phi_{\text{BS}} = 0^\circ$ . Additionally, more electrons are backscattered towards higher  $\Theta_{\text{BS}}$  values with the highest concentration of backscattered electrons at  $\Theta_{\text{BS}} \approx \Theta_{\text{I}}$ . The distributions are symmetric around  $\phi_{\text{BS}} = 0^\circ$ .

### Backscattering Coefficients

For the simulation, several types of backscattering coefficients can be defined depending on the detection mechanism and energy constraints.

The total backscattering coefficient  $\eta_{\text{tot}}$  is defined as the ratio between the total number of backscattered electrons  $N_{\text{out}}$  as detected by the WD (without the simulation of the BSD) and all initially generated electrons  $N_{\text{in}}$ :

$$\eta_{\text{tot}} = \frac{N_{\text{out}}}{N_{\text{in}}}. \quad (6.8)$$

It is therefore the most inclusive coefficient, as it is independent of the modelling of the detector response and includes all backscattered electrons. As a result, it is the maximal coefficient which can be determined and only depends on the detector material. Unfortunately, in the experimental setup, it cannot be determined due to the spatial limitation of the BSD and the detector response of both detectors.

The partial backscattering coefficient  $\eta_{\text{part}}$  is defined as the ratio of the electrons  $N_{\text{BSD}}$  detected by any pixel of the BSD and the electrons  $N_{\text{SOD}}$  detected by the SOD:

$$\eta_{\text{part}} = \frac{N_{\text{BSD}}}{N_{\text{SOD}}}. \quad (6.9)$$

For this coefficient, no CCE was applied for the summation of the energy depositions in the detectors. It should serve as a theoretical upper boundary of detectable backscattering coefficients in the designed detector geometry. Thus, it accounts for the limited spatial coverage of the BSD but neglects the detector response.

The experimental backscattering coefficient  $\eta_{\text{exp}}$  is the ratio of  $N_{\text{BSD}}$  and  $N_{\text{SOD}}$  for electrons with energies  $E$  above the energy thresholds of the respective detector:

$$\eta_{\text{exp}} = \frac{N_{\text{BSD}}(E_{\text{BSD}} > E_{\text{BSD,T}})}{N_{\text{SOD}}(E_{\text{SOD}} > E_{\text{SOD,T}})}. \quad (6.10)$$

Here, the full detector model is applied, i.e. the CCE model as well as the noise model are included. It is comparable to the experimental backscattering coefficient of the measurements which was shown in fig. 5.22.

The coincidence backscattering coefficient  $\eta_{\text{coinc}}$  is defined as:

$$\eta_{\text{coinc}} = \frac{N_{\text{BSD}}(E_{\text{BSD}} > E_{\text{BSD,T}} \ \& \ E_{\text{CC}} > E_{\text{SOD,T}})}{N_{\text{CC}}(E_{\text{CC}} > E_{\text{SOD,T}})}. \quad (6.11)$$

It is comparable to the coincidence backscattering coefficient of the measurements which was shown in 5.32. Here,  $N_{CC}$  denotes the number of detected electrons in the central pixel of the SOD. For the simulated electron beam, which only hits the CC pixel, the relation  $N_{CC} = N_{SOD}$  holds.

In fig. 6.10, the backscattering coefficients defined above for different incident angles at  $E_I = 5 \text{ keV}$  and  $E_I = 10 \text{ keV}$  are compared. The partial backscattering coefficient  $\eta_{\text{part}}$ , which only poses geometrical constraints on the backscattered electrons, is much smaller than  $\eta_{\text{tot}}$ . The number of observable backscattered electrons is reduced by up to a factor of four at  $\Theta_I = 0^\circ$ . The experimentally accessible coefficients  $\eta_{\text{exp}}$  and  $\eta_{\text{coinc}}$  are additionally smaller than  $\eta_{\text{part}}$  due to the introduction of energy thresholds as in the experiment. For example at  $E_I = 10 \text{ keV}$  and  $\Theta_I 0^\circ$  the total simulated backscattering coefficient amounts to close to 20%, but because of geometrical and energy constraints in the experimental setup only an experimental backscattering coefficient of about 4% is observable.

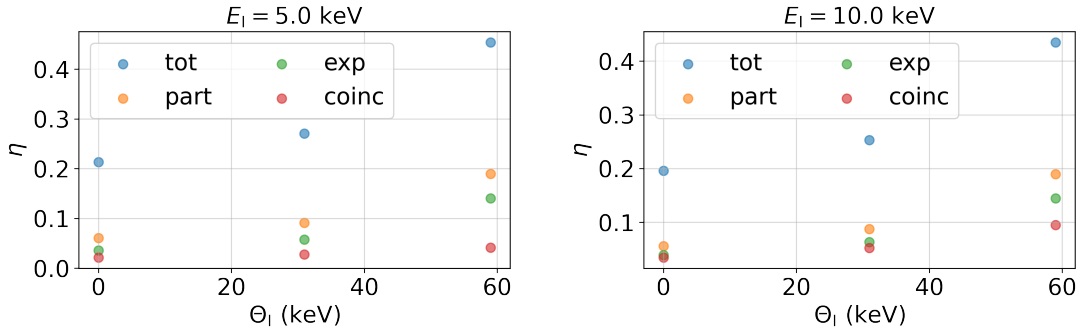


**Figure 6.10: Simulated Backscattering Coefficients as a Function of the Incident Angle.** The coefficients are defined in eq. 6.8 to 6.11. The coefficients show the expected increase for higher  $\Theta_I$ . The experimentally accessible coefficients  $\eta_{\text{exp}}$  and  $\eta_{\text{coinc}}$  are much smaller than the total simulated backscattering coefficient  $\eta_{\text{tot}}$ .

## 6.5 Summary

The experimental setup was implemented in GEANT4 with a few simplifications, and a data processing procedure was developed. A fitting procedure was developed to extract the charge collection efficiency parameters from the experimental electron energy spectrum. A mean dead layer thickness of  $10.7^{+2.8}_{-6.7}$  nm was evaluated, which is in agreement with a design value of 8–10 nm for the silicon-dioxide layer thickness. The mean detection efficiency behind the dead layer is  $85.6^{+4.2}_{-9.1}$  % and the mean effective transition layer thickness is  $75.7^{+25.1}_{-26.2}$  nm. With those parameters, the spectral shape of the energy spectrum measured in the SOD in the experiment was reproduced with the simulated data.

The energy and angular distribution of all backscattered electrons was investigated. Moreover, different experimental backscattering coefficients were extracted from the simulations. The impact of the experiment-specific constraints on e.g. the geometry of the detectors and the energy thresholds of the detectors on the backscattering coefficient was investigated. Although, for example, at  $E_I = 10$  keV and  $\Theta_I = 0^\circ$  the total simulated backscattering coefficient amounts to about 20 %, only a backscattering coefficient of around 4 % is experimentally accessible.

To examine the applicability of the simulation to investigate electron backscattering, its outcome needs to be compared to the experimental results.



# Comparison of Experiment and Simulation

In this chapter, it is discussed how good the experimental results can be reconstructed by GEANT4 simulations. In section 7.1, the uncertainty determination applied for the comparison of experiment and simulation is explained, i.e. which uncertainties are expected to have a relevant influence on the results and how they are taken into account. A comparison of the detected coincidence energy spectra of the SOD and BSD is shown in section 7.2. The angular distribution of backscattered electrons and the backscattering coefficients are compared in section 7.3 and 7.4, respectively.

## 7.1 Uncertainty Estimation

For the comparison of experiment and simulation three main sources of uncertainties have been taken into account:

1. Uncertainty on the CCE model parameters ( $DL$ ,  $p_1$  and  $\lambda$ ): As explained in section 6.3.2, the first fit of the detector model did not converge towards one set of CCE model parameters. The mean values were implemented in the subsequent simulations. A possible variation of the  $DL$ ,  $p_1$  and  $\lambda$  parameter between the minimal and the maximal value of the first fit results was applied for the following uncertainty estimation.
2. Geometrical uncertainties as illustrated in fig. 7.1 ( $d\Theta_I$ ,  $d\Theta_{TO}$ ,  $dx$ ,  $dy$ ,  $dz$ ): The incident angle at the SOD is freely selectable in the experiment. It had to be adjusted by hand. The take-off angle  $\Theta_{TO}$  for the BSD can vary due to some play in the fixation of the holding structure on the cooling plate. Furthermore, a slight angular uncertainty can arise from the gluing procedure, when the SDD chip is glued on the ceramic block. The angles are therefore assumed to be known to a precision of about  $3^\circ$ . The positioning of the BSD in  $x$ -,  $y$ - and  $z$ -direction relative to the SOD is known down to a few mm. For the following analysis, a possible shift of up to 3 mm in every direction was assumed with the exception of a shift in positive  $x$ -direction. Here, only a maximal shift of 2 mm was assumed. Due to the closeness of the BSD to the electron beam, for a larger shift, the BSD chip would block the electrons for the  $\Theta_I = 0^\circ$  configuration.

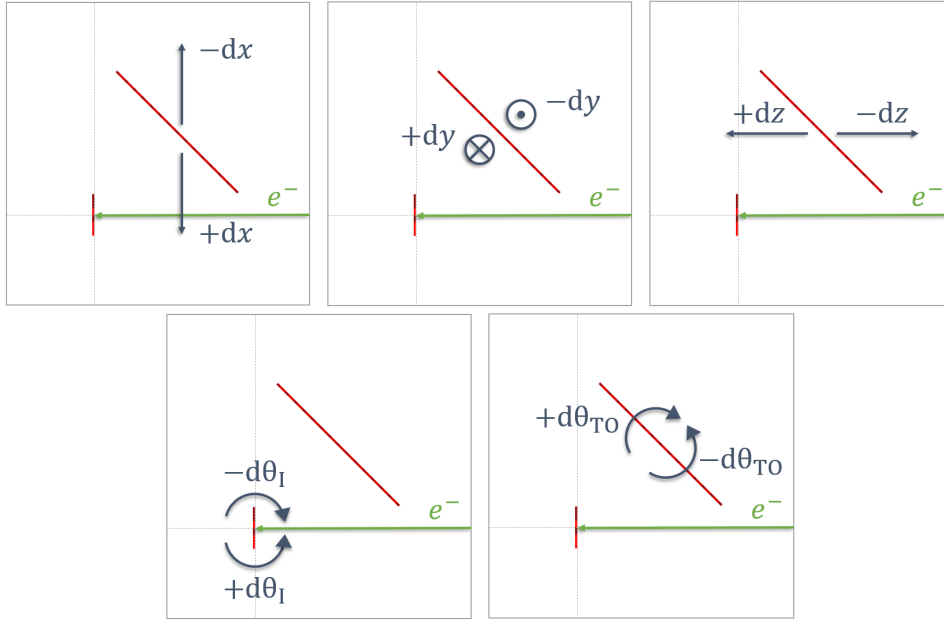


**Figure 7.1: Illustration of the Geometrical Uncertainties.** In red, the SOD and the BSD are pictured in the top view exemplary for a  $\Theta_I = 0^\circ$  configuration. The electron beam is pictured by the green arrow. For each parameter, the direction of variation is indicated.

3. Uncertainty on the number of initial electrons measured in the SOD in the experiment ( $dN_{\text{SOD}}$ ): A total uncertainty of 1.41 % on the measured initial electron number in the SOD is assumed due to charge sharing and pileup as explained in section 5.3. An uncertainty on the number of coincidence events is not considered. Additionally, an uncertainty on the amount of detected backscattered electrons in the BSD is neglected.

A summary of the mentioned parameters and their minimal and maximal value or variation is provided in table 7.1.

**Table 7.1: Uncertainties on Selected Parameters.** For each parameter either the minimal and maximal value or the minimal and maximal variation is listed.

Parameter	Default value	Minimal value	Maximal value
$DL$	10.7 nm	4.0 nm	13.5 nm
$\lambda$	75.7 nm	49.51 nm	100.8 nm
$p_1$	0.865	0.765	0.898
$dx$	0 mm	-3 mm	2 mm
$dy$	0 mm	-3 mm	3 mm
$dz$	0 mm	-3 mm	3 mm
$d\theta_I$	$0^\circ$	$-3^\circ$	$3^\circ$
$d\theta_{\text{TO}}$	$0^\circ$	$-3^\circ$	$3^\circ$
$dN_{\text{SOD}}$	0 %	-1.41 %	1.41 %

The CCE model parameter as well as the geometrical uncertainties are applied on the results of the simulation. For this, two approaches were followed:

1. Monte Carlo approach to estimate the total uncertainty: For each CCE and geometry parameter, a value within the parameter limits was randomly picked. This set of parameter values was then implemented in the simulation. Subsequently, a simulation for each of the nine measurement settings was run. This procedure was performed ten times to obtain in total ten simulations with varied parameters plus one simulation with the default values for each measurement setting. For the data to be comparable with the experiment, a fit of each of the simulated SOD energy spectra has to be carried out as described in subsection 6.3.2 (without step 1). For  $\Theta_I = 0^\circ$  and  $E_I = 7.5 \text{ keV}$  and two of the parameter value sets, the fit did not work properly. For this configuration, those two sets were therefore excluded from the uncertainty analysis.
2. Determination of the parameter with the most influence: Two  $\Theta_I/E_I$  combinations ( $10 \text{ keV}/0^\circ$  and  $5 \text{ keV}/59^\circ$ ) were chosen to determine the parameters which have the highest influence on the results. For each configuration, sixteen simulations were performed, two per parameter as specified in table 7.1 (excluding  $dN_{\text{SOD}}$ ). Respectively, one simulation for the minimal and maximal parameter value was conducted. Each SOD energy spectrum was fitted to the experimental equivalent to determine the remaining parameters as defined in subsection 6.3.2 (without step 1).

## 7.2 Energy Spectra

The electron beam in the simulation has no angular spread and hits only the CC pixel of the SOD. In the experiment, several pixels in the SOD are irradiated. Therefore, to minimise distortions in the energy spectrum measured in the BSD arising from different incident angles at the SOD, only coincidence events between the CC pixel and the BSD were chosen for the comparison of the energy spectra.

The simulated data was not corrected for pileup. In the experiment, coincidence between a pileup event in the SOD and an event in the BSD is possible. Therefore, to make the simulated and the experimental energy spectra comparable, an upper energy limit is applied on the experimental data. The sum of the energy  $E_{\text{SOD}}$  of the coincidence event in the SOD and the energy  $E_{\text{BSD}}$  of the coincidence event in the BSD must be smaller than the initial electron energy plus some factor  $E_{\text{res}}$  accounting for the energy resolutions of both detectors:

$$E_{\text{SOD}} + E_{\text{BSD}} < E_I + E_{\text{res}}. \quad (7.1)$$

Here,  $E_{\text{res}}$  is evaluated through the energy resolutions FWHM (eq. 4.3 and 4.4) of the respective detector at  $E_I$  with:

$$E_{\text{res}} = \sqrt{\text{FWHM}_{\text{SOD}}^2(E_I) + \text{FWHM}_{\text{BSD}}^2(E_I)}. \quad (7.2)$$

The parameter  $c_{\text{el}}$  of equation 4.3 was calculated from the mean FWHM per detector determined during the  $^{55}\text{Fe}$  calibration (sec. 5.3.1) and amounts to  $c_{\text{el}} = 51.2 \text{ eV}$  for the SOD

and  $c_{\text{el}} = 68.9 \text{ eV}$  for the BSD. In addition to the upper energy limit, energy thresholds ( $E_{\text{SOD,T}}$  and  $E_{\text{BSD,T}}$ ) were applied for coincidence events in both detectors as explained in subsection 6.3.1.

Furthermore, the pixels 2 to 12 and 157 to 168 were excluded from the data. In the experiment, those pixels are partly shaded by the PCB board of the SOD. Thus, their contribution to the energy spectra is smaller than in the simulation. Moreover, all pixels with noise or connection issues, which were excluded in the analysis of the experimental data, were excluded in the simulation as well.

In fig. 7.2, the resulting coincidence energy spectra recorded by the CC pixel of the SOD for four different  $E_I/\Theta_I$  configurations are shown. The spectra are in agreement within the total uncertainty, whereby the accordance is better for higher initial energies and smaller incident angles. The total uncertainty is higher for small initial electron energies.

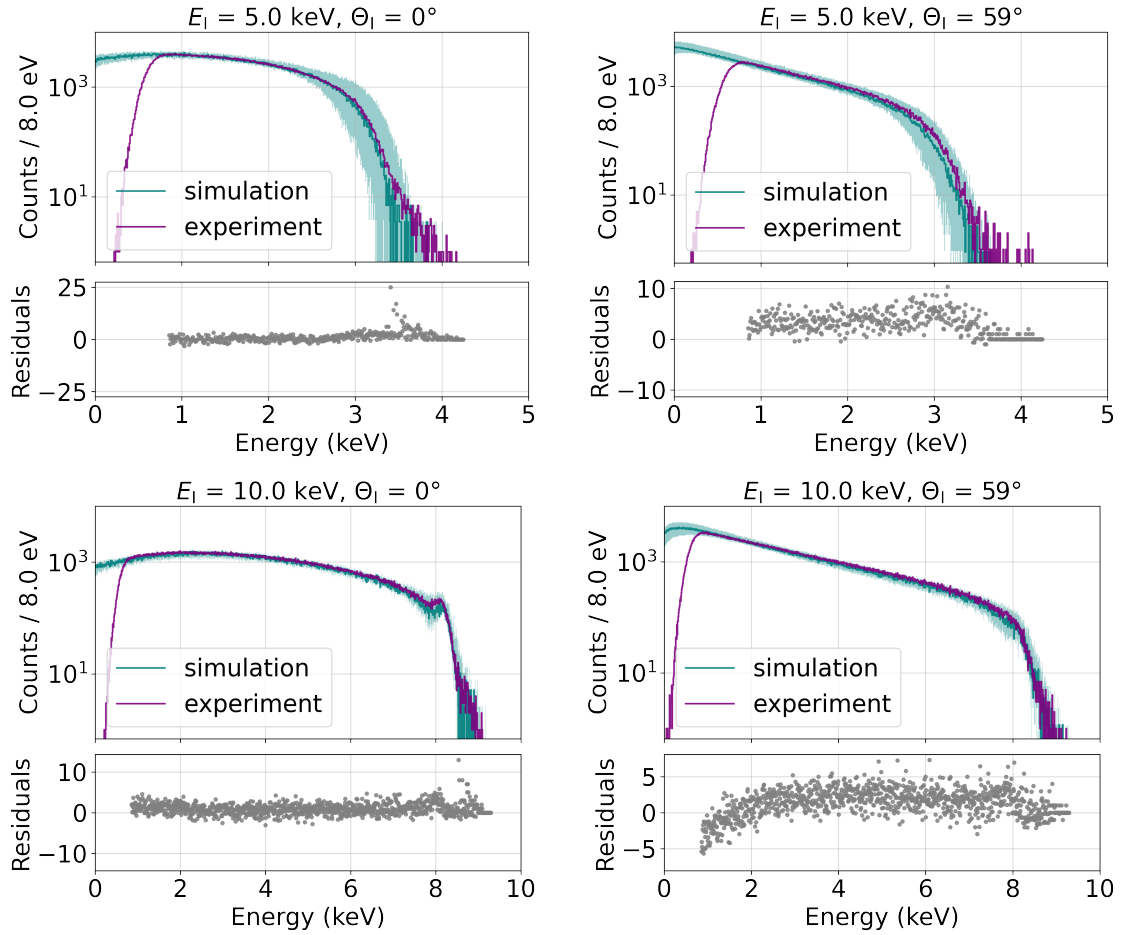


**Figure 7.2: Coincidence Electron Energy Spectra of the CC Pixel for Experiment and Simulation.** The total uncertainty on the simulated spectra is the minimal and maximal value per bin extracted from approach one of the uncertainty estimation (sec. 7.1). The residuals were calculated for energies between  $E_{\text{SOD,T}}$  and  $E_I - (E_{\text{BSD,T}} - E_{\text{res}})$ . The simulated spectrum is in agreement with the experimental one within the uncertainties for every  $E_I/\Theta_I$  configuration.

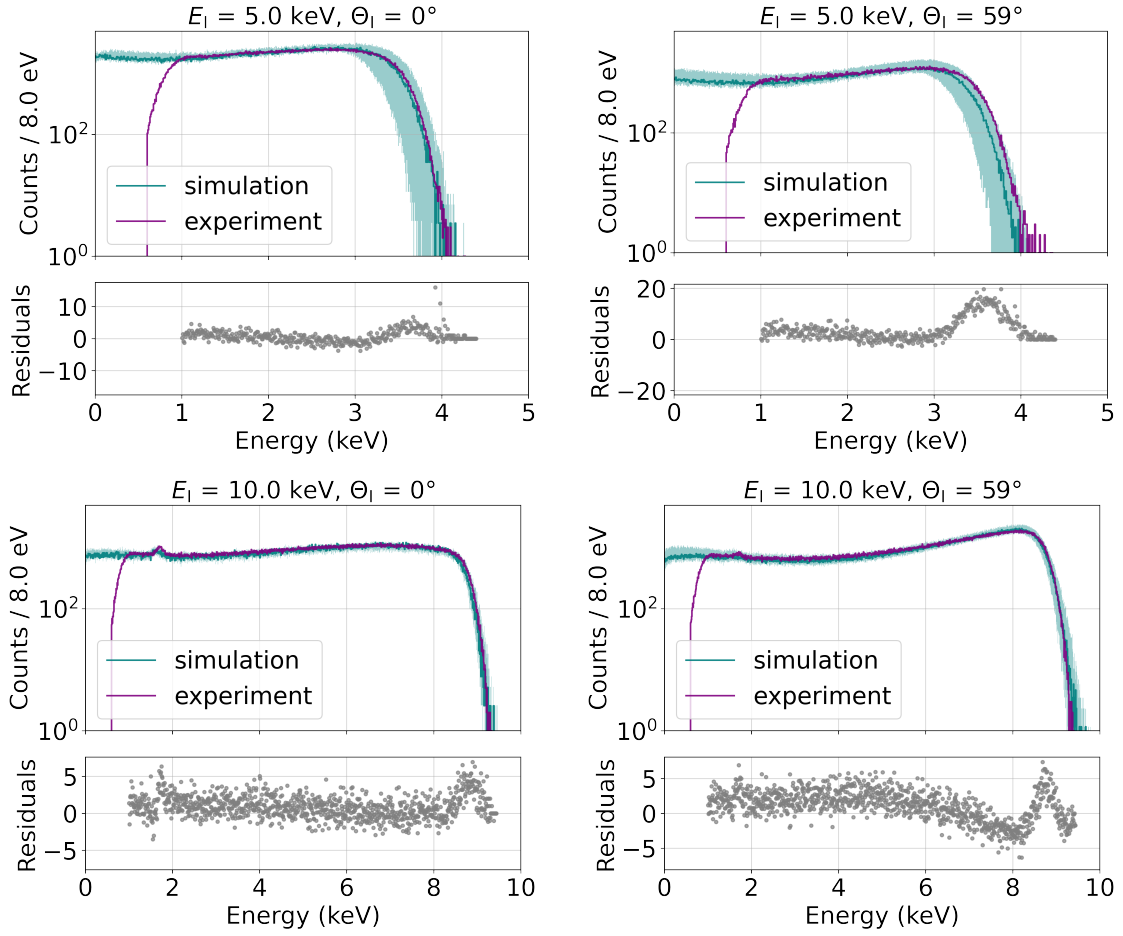


**Figure 7.3: Coincidence Electron Energy Spectra of the BSD for Experiment and Simulation.** The energy spectra of all included pixels of the BSD were combined. The total uncertainty on the simulated spectra is the minimal and maximal value per bin extracted from approach one of the uncertainty estimation (sec. 7.1). The residuals were calculated for energies between  $E_{\text{BSD},T}$  and  $E_I - (E_{\text{SOD},T} - E_{\text{res}})$ . The simulated spectrum is in agreement with the experimental one within the uncertainties for every  $E_I/\Theta_I$  configuration.

The same behaviour is observed for the energy spectra of the backscattered electrons. The energy spectra of the coincidence events detected by the BSD can be seen in fig. 7.3 for all included pixels combined. Slight differences between simulation and experiment can be observed at the photon peak, which is more present in the experiment. In addition, the more the transition layer plays a role, the higher is the mismatch between simulation and experiment at the spectral decline at high energies. Nevertheless, all simulations agree with the experimental results within the uncertainties. For completeness, the comparison of the energy spectra recorded by the CC pixel or the BSD for all remaining  $E_I/\Theta_I$  configurations is attached in appendix A.3.

A good agreement of the energy spectra recorded by the pixel groups introduced in subsection 5.4.2 was achieved. The best spectral agreement was achieved for the pixel groups with small  $\Theta_{\text{BS}}$  as well as for low incident angles.

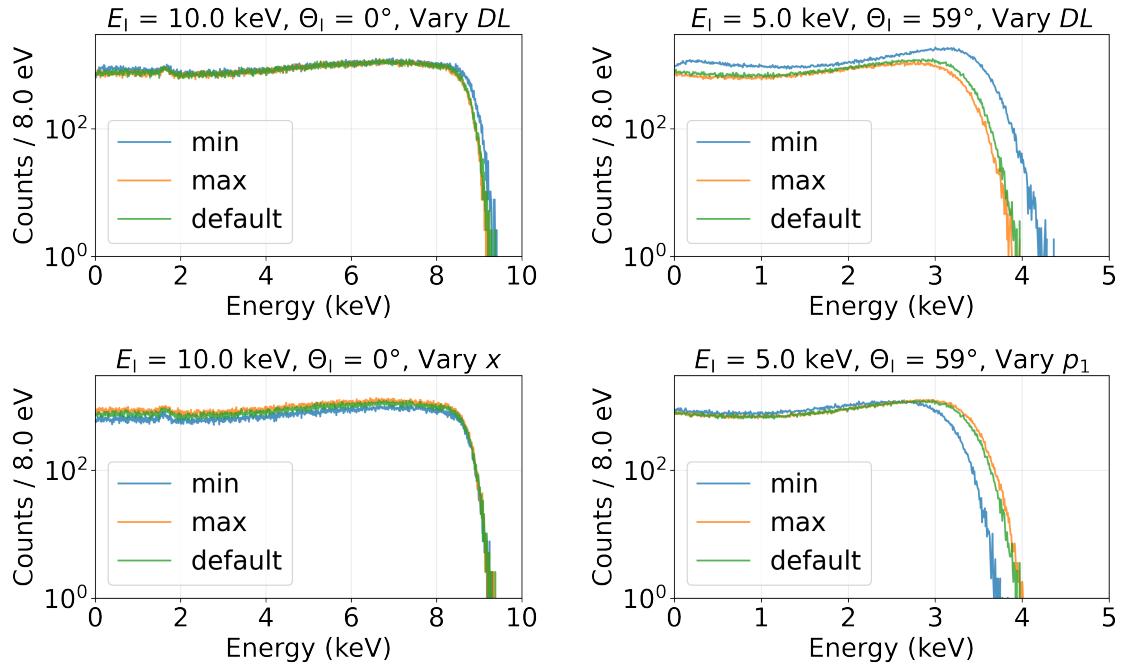


**Figure 7.4: Impact on the Backscattered Electron Energy Spectrum for Variations of the Most Important Parameters.** On the left, the BSD energy spectra for the  $\Theta_I = 0^\circ/E_I = 10\text{ keV}$  configuration, and, on the right, the spectra for the  $\Theta_I = 59^\circ/E_I = 5\text{ keV}$  configuration are shown. In the upper row, the spectra for the variation of the parameter with the most influence is shown. The second row depicts the impact of the respective second most important parameter. The spectra are shown for the default, minimal and maximal parameter value, as defined in table 7.1. A variation of the  $DL$  has an impact on the shape, a shift in  $x$ -direction on the amplitude and a variation of the  $p_1$  parameter on the endpoint of the spectrum.

To determine the parameter with the highest impact on the spectral shape of the energy spectrum of backscattered electrons, the simulations of approach two of the uncertainty estimation were directly compared to the respective default simulation. At  $\Theta_I = 0^\circ$  and  $E_I = 10\text{ keV}$ , the parameters  $DL$  and  $x$  have the most impact on the spectral shape, while at  $\Theta_I = 59^\circ$  and  $E_I = 5\text{ keV}$ , the parameters  $DL$  and  $p_1$  have the highest impact. In contrast, a shift in  $y$ -direction has the smallest effect on the spectral shape. In total, a variation of the parameters has a bigger impact on the observed energy spectra at  $\Theta_I = 59^\circ$  and  $E_I = 5\text{ keV}$ .

In fig. 7.4, the impact of the parameters  $DL$ ,  $p_1$  and  $x$  on the energy spectrum of backscattered electrons in the simulation is shown. The dead layer thickness  $DL$  has both an impact on the spectral shape and the endpoint. For smaller  $DL$  values, the detectable energy deposition in the BSD is higher. The endpoint is shifted to larger energies. As expected, its impact on the spectrum is maximal at high incident angles and small initial electron energies. The second most important transition layer parameter is  $p_1$ . For smaller  $p_1$ , hence worse detector efficiencies after the dead layer, the endpoint of the energy spectrum is shifted towards lower energies. The electrons are predominantly backscattered towards

small  $\Theta_{\text{BS}}$  at  $\Theta_1 = 0^\circ$ . Therefore, if the BSD is shifted in  $x$ -direction towards the electron beam, the amplitude of the energy spectrum is increased. An increase by almost a factor two for a shift of 5 mm is notable. An impact on the endpoint was not observed.

As a result, the CCE has to be precisely modelled to be able to correctly predict the observed energy spectra. Hence, the mismatch of the energy spectrum of backscattered electrons for experiment and simulation at high incident angles and low initial electron energies can be traced back to the already discussed difficulties with the determination of the CCE model parameters.

### 7.3 Angular Distribution

Due to the angular spread of the electron beam in the experiment, the angular distribution of the backscattered electrons is a superposition of backscattering from all SOD pixels and the surrounding materials. In the simulation, only the CC pixel is hit. Therefore, for the comparison of the angular distribution of backscattered electrons between simulation and experiment, only coincidence events are taken into account. In addition, no upper energy limit (cf. eq. 7.1) on the energies of the coincidence events as for the comparison of the energy spectra was considered. Only the energy thresholds  $E_{\text{SOD},T}$  and  $E_{\text{BSD},T}$  were applied.

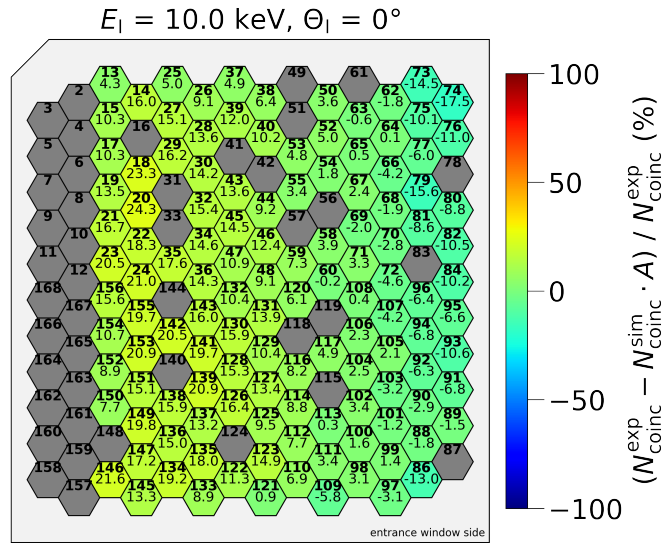


**Figure 7.5: Difference in  $N_{\text{coinc}}$  Per Pixel in the BSD Between Experiment and Simulation.** The number  $N_{\text{coinc}}$  of backscattered electrons with coincidence with the CC pixel is calculated according to eq. 5.4 for the experiment ( $N_{\text{coinc}}^{\text{exp}}$ ) and the simulation ( $N_{\text{coinc}}^{\text{sim}}$ ), respectively. The number of backscattered electrons in the simulation is scaled with the amplitude  $A$  evaluated in subsection 6.3.2. A difference of up to 30% at high  $\Theta_{\text{BS}}$  can be observed.

The number  $N_{\text{coinc}}$  of backscattered electrons per pixel in the BSD with coincidence with

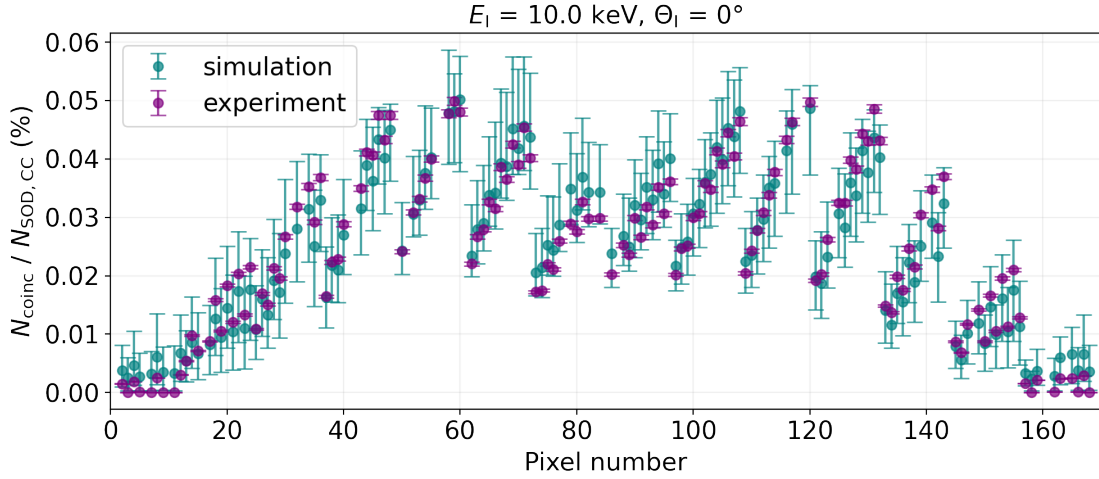


**Figure 7.6: Comparison of  $N_{\text{coinc}}$  in the BSD as a Function of the Pixel Number.** The number of backscattered coincidence electrons are scaled to the number of initial electrons detected in the CC pixel  $N_{\text{SOD,CC}}$ . The uncertainty for the experiment is 1.41 % on  $N_{\text{SOD,CC}}$ . The uncertainty on the simulated rates is the minimal and maximal value extracted from approach one of the uncertainty estimation (sec. 7.1). Almost only the simulated values in the pixels of left two columns of the BSD (pixel 2 to 12 and 157 to 168) do not agree with the experiment.

the CC pixel are compared in fig. 7.5. A variation of  $N_{\text{coinc}}$  per pixel of up to 30 % (neglecting the two leftmost pixel columns) was observed. The  $N_{\text{coinc}}$  values observed in the simulation are higher at small  $\Theta_{\text{BS}}$  and vice versa in comparison to the experiment. The difference of  $N_{\text{coinc}}$  per pixel stays mainly unchanged for all  $E_{\text{I}}/\Theta_{\text{I}}$  configurations. Nonetheless,  $N_{\text{coinc}}$  in the simulation agrees with the values measured in the experiment within the uncertainties which can be seen in fig. 7.6 exemplary for  $E_{\text{I}} = 10 \text{ keV}$  and  $\Theta_{\text{I}} = 0^\circ$ .

To estimate the parameters which have the highest influence on the detected angular distribution of the backscattered electrons, the simulations of approach two of the uncertainty estimation (sec. 7.1) are compared to the respective default simulation. At  $\Theta_{\text{I}} = 0^\circ$  and  $E_{\text{I}} = 10 \text{ keV}$ , a shift in  $x$ -,  $y$ - or  $z$ -direction has the most impact on the detected angular distribution. In addition, the transition layer parameters, especially  $DL$  and  $p_1$ , have a high impact on the detected angular distribution for  $\Theta_{\text{I}} = 59^\circ$  and  $E_{\text{I}} = 5 \text{ keV}$ .

In fig. 7.7, the impact of the parameters  $x$ ,  $z$  and  $DL$  on the angular distribution is shown. A shift in  $x$ -direction of about 5 mm leads to a variation in the number of coincidence events of up to over 100 % for  $\Theta_{\text{I}} = 0^\circ$  and  $E_{\text{I}} = 10 \text{ keV}$ . With exception for the pixel columns closest to the initial electron beam,  $N_{\text{coinc}}$  increases for a shift in positive  $x$ -direction.

An increase of the  $DL$  value leads to an overall reduction of detected backscattered electrons for  $\Theta_{\text{I}} = 59^\circ$  and  $E_{\text{I}} = 5 \text{ keV}$ , especially at high  $\Theta_{\text{BS}}$ . A decrease of  $N_{\text{coinc}}$  of up to about 60 % can be observed.

For  $\Theta_{\text{I}} = 0^\circ$  and  $E_{\text{I}} = 10 \text{ keV}$ , a shift of the BSD in positive  $z$ -direction, thus closer to the SOD, increases  $N_{\text{coinc}}$  for low  $\Theta_{\text{BS}}$  up to about 60 % and reduces it at high  $\Theta_{\text{BS}}$  up to

about 85 %. At  $\Theta_I = 59^\circ$  and  $E_I = 5$  keV, a similar behaviour is observable. Here, a shift of the BSD in positive  $z$ -direction does not bring the BSD closer to the SOD (see fig. 5.8). However, the electrons are predominantly backscattered to high  $\Theta_{BS}$ . As a result, a shift in positive  $z$ -direction shifts the detected angular distribution of backscattered electrons more to the right side of the BSD.

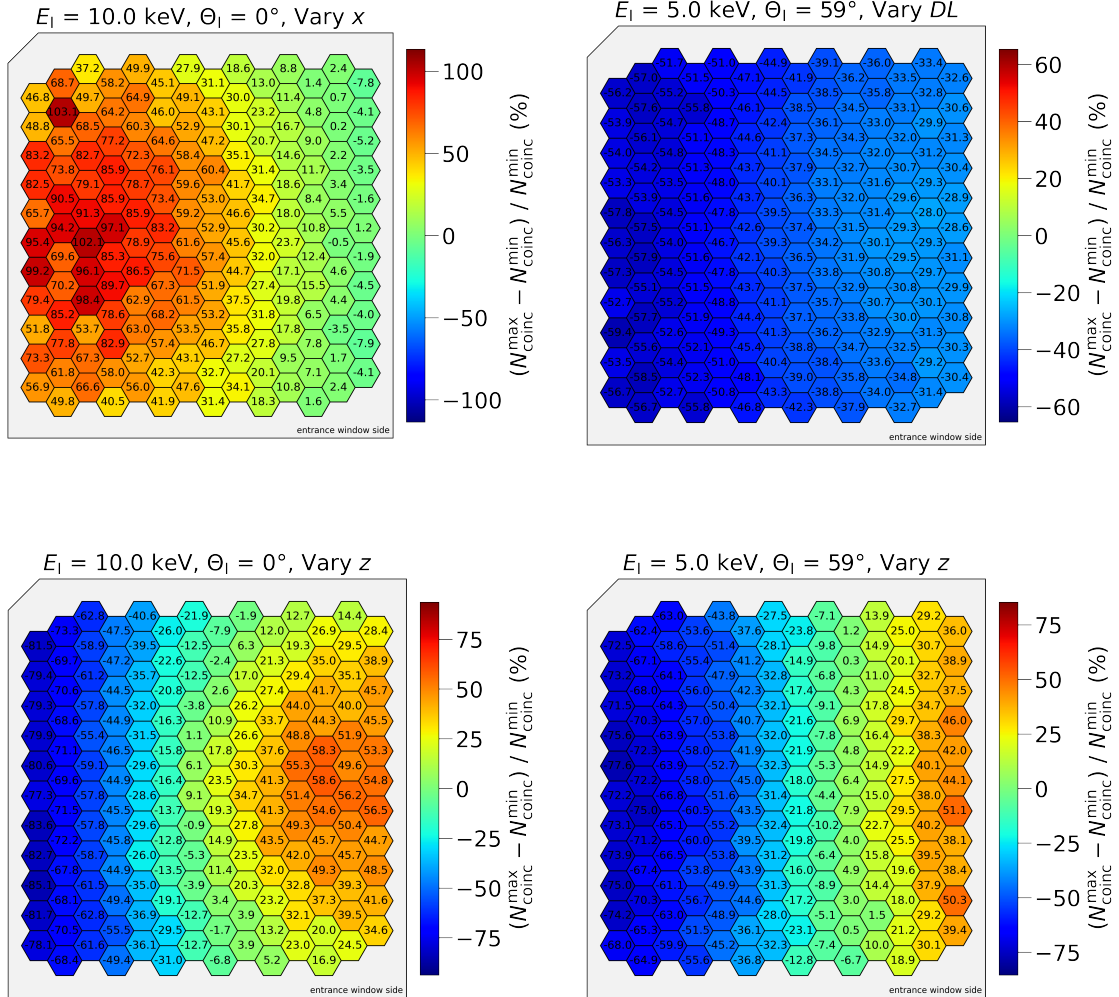


**Figure 7.7: Difference of the Angular Distribution for Variations of the Most Important Parameters.** The difference between the number  $N_{\text{coinc}}^{\text{max}}$  of coincidence events in the simulation with the maximal parameter value and the number  $N_{\text{coinc}}^{\text{min}}$  of coincidence events in the simulation with the minimal parameter value was calculated for each pixel. On the left, the difference in  $N_{\text{coinc}}$  relative to  $N_{\text{coinc}}^{\text{min}}$  for the  $\Theta_I = 0^\circ/E_I = 10$  keV configuration, and, on the right, the difference for the  $\Theta_I = 59^\circ/E_I = 5$  keV configuration is shown. The upper row depicts the variation in  $x$ -direction and the  $DL$  parameter. The second row compares the variation in  $z$ -direction. Variations of up to 100 % are observable for a shift in positive  $x$ -direction. A thicker dead layer decreases the observed electron number over the whole BSD up to 60 %. A shift in  $z$ -direction leads to variations of up to 85 %.

In total, small variations in the geometrical parameters lead to very high variations in the observed number of coincidence events per pixel. This relativises the mismatch between simulation and experiment of up to 30%. Furthermore, high emphasis on the correct geometrical alignment of the BSD relative to the SOD should be put in future experiments.

## 7.4 Backscattering Coefficients

In terms of the backscattering coefficient not only coincidence events can be compared, but also the total detected electron numbers on the detectors. The coefficients are calculated according to eq. 5.3 and 5.5 for the experiment and eq. 6.10 and 6.11 for the simulation. For the comparison, the pixels 2 to 12 and 157 to 168 were excluded from the data. Within the uncertainties, the coefficients match for all incident angles and initial electron energies which can be seen in fig. 7.8.

The parameter with the most influence is determined by directly comparing the backscattering coefficient of the simulations with the minimal and maximal parameter value (uncertainty estimation approach two) with the default simulation. For each parameter, the deviation  $\Delta\eta$  was therefore calculated as:

$$\Delta\eta_{s,p} = \frac{\eta_{s,p} - \eta_{s,\text{default}}}{\eta_{s,\text{default}}} \quad (7.3)$$

with  $s \in \{\text{exp, coinc}\}$  and  $p \in \{\text{min, max}\}$ . Here, min and max stands for the simulations with the minimal or maximal parameter value, respectively. In table 7.1, the deviations for all coefficients and parameters at the chosen  $\Theta_I/E_I$  settings are summarised. The parameters causing the largest deviations are marked in red.

Especially a shift in  $x$ -direction has a high impact on the amount of detected backscattered electrons in the BSD. Furthermore, a variation of the incident angle has a high impact, which can be derived from the behaviour of the backscattering coefficient for increasing incident angles in general. As a result, a more precise way to define  $\Theta_I$  at the SOD and the  $x$ -position of the BSD relative to the SOD in the experiment should be headed for in future measurements. At  $E_I = 10 \text{ keV}$  and  $\Theta_I = 0^\circ$ ,  $\Theta_{BS}$  and the  $z$ -position of the BSD have a medium influence on the measured backscattering coefficients. For  $E_I = 5 \text{ keV}$  and  $\Theta_I = 59^\circ$ , the large impact of the  $DL$  parameter stands out for the observation of  $\eta_{\text{coinc}}$ . The  $\lambda$  parameter and the  $y$ -position of the BSD have in all cases the smallest effect on the backscattering coefficients.

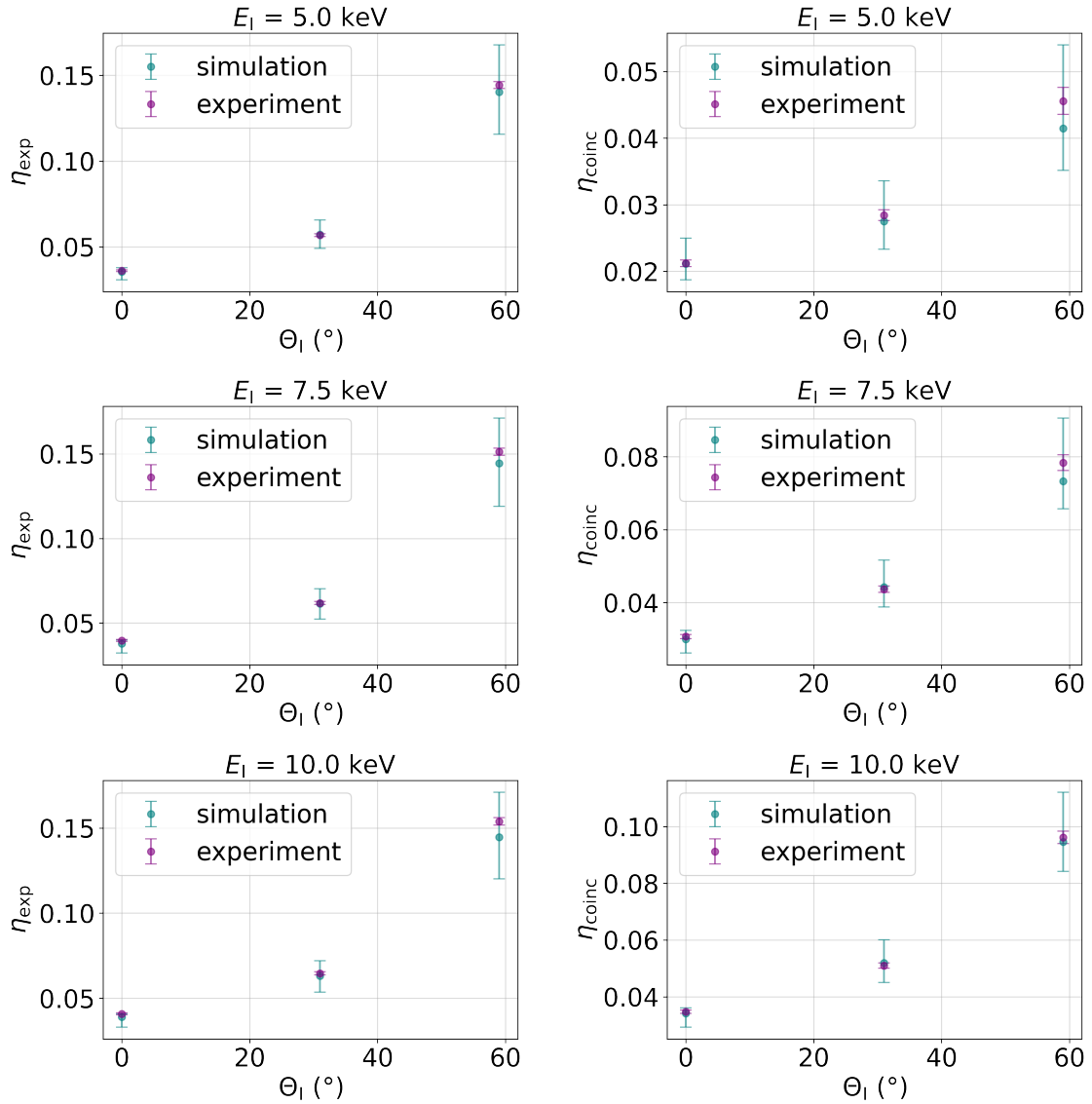


**Figure 7.8: Comparison of the Backscattering Coefficients as a Function of the Incident Angle.** An uncertainty on the rate at the CC pixel of 1.41% was applied for the experiment. For the simulation, the errors are the minimal and maximal value of  $\eta_{\text{exp}}$  derived from the simulations of approach one of the uncertainty estimation.

**Table 7.2: Relative Deviation of the Backscattering Coefficients for Variation of one Parameter.** For each CCE and geometrical parameter, the relative deviation of the backscattering coefficient for minimal and maximal variation of the parameter compared to the respective default simulation is listed. The impact on the experimental and the coincidence backscattering coefficient is shown. The largest deviations are marked in red.

(a) Deviations @  $E_I = 10 \text{ keV}$  and  $\Theta_I = 0^\circ$

Parameter	$\Delta\eta_{\text{exp,min}}$ (%)	$\Delta\eta_{\text{exp,max}}$ (%)	$\Delta\eta_{\text{coinc,min}}$ (%)	$\Delta\eta_{\text{coinc,max}}$ (%)
$DL$	2.2	-0.7	4.3	-1.3
$\lambda$	0.3	0.1	0.9	0.3
$p_1$	-0.6	0.2	-1.2	0.3
$\Theta_I$	-7.3	6.9	-7.6	6.9
$\Theta_{\text{TO}}$	-5.2	4.9	-5.8	5.4
$x$	-14.6	10.2	-15.1	10.5
$y$	-2.0	-0.7	-2.1	-0.8
$z$	-7.1	5.8	-6.6	5.2

(b) Deviations @  $E_I = 5 \text{ keV}$  and  $\Theta_I = 59^\circ$

Parameter	$\Delta\eta_{\text{exp,min}}$ (%)	$\Delta\eta_{\text{exp,max}}$ (%)	$\Delta\eta_{\text{coinc,min}}$ (%)	$\Delta\eta_{\text{coinc,max}}$ (%)
$DL$	-0.1	-0.1	35.8	-11.1
$\lambda$	-0.0	0.0	0.0	-0.8
$p_1$	-0.0	0.0	-14.3	3.0
$\Theta_I$	-10.4	10.3	-8.2	6.7
$\Theta_{\text{TO}}$	1.2	-1.9	-4.3	3.6
$x$	-13.9	10.3	-11.3	8.2
$y$	-1.8	-0.6	-2.0	-0.6
$z$	-2.4	-1.0	5.7	-8.9

## 7.5 Summary

The energy spectra of the CC pixel and the BSD for coincidence events, the angular distribution of coincidence events and the backscattering coefficients for all detectable events and for coincidence events were compared. In total, a good agreement of the simulated data with the experimental data within the uncertainties was achieved. This validates the GEANT4 simulation toolkit to be suitable for investigations of electron backscattering on silicon materials.

A detailed uncertainty investigation showed a high impact of the dead layer thickness parameter on the detected backscattered electron energy spectra and the angular distribution, especially at high azimuthal backscattering angles, as well as on the coincidence backscattering coefficients. The impact is maximal for low initial energies and high incident angles. The second most important CCE parameter turned out to be  $p_1$ , which has a high impact on the measured endpoint energy in the backscattered electron energy spectrum.

Of major importance in the measurement setup turned out to be the  $x$ -position of the BSD relative to the SOD. A shift of 5 mm can double the observed number of backscattered coincidence electrons detected in a pixel of the BSD. In the measured backscattered electron energy spectrum, this shift leads to an increase of the amplitude by almost a factor of two over the entire energy range. For the measured backscattering coefficients, the shift leads to a variation of up to 15%. The second most important geometrical parameter is the  $z$ -position of the BSD relative to the SOD. It highly impacts the measured angular distribution as well as the measured backscattering coefficients.



# Conclusion and Outlook

A multi-pixel Silicon Drift Detector system (TRISTAN) is currently being developed to upgrade the KATRIN experiment in order to enable a keV-scale sterile neutrino search. One of the key requirements for a sterile neutrino signature in a tritium beta-decay spectrum is a precise understanding of the detector response to electrons. Electrons that are scattered back from the detector have a strong impact on the measured energy spectrum. To accurately model the detector response to electrons in the KATRIN beamline, the relations between the energies and angles of the initial electrons and the backscattered electrons have to be precisely determined.

One major goal of this thesis was the design of an experimental test facility to study the effect of detector backscattering. The relations between the energy and angle of incoming and backscattered electrons were successfully probed with two TRISTAN silicon drift detector devices. One 7-pixel detector was used as a scatterer, whereas the other detector, a 166-pixel detector array, served as a detector for the backscattered electrons.

Based on a coincidence analysis, the signature of backscattered electrons in the energy spectrum of the scatterer was extracted. Additionally, the backscattering detection efficiency was estimated, which allows the extraction of the backscattering coefficient which is often stated in literature. A backscattering coefficient of about 17 % for an initial electron energy of 10 keV and an incident angle of  $0^\circ$  was evaluated. This is in good agreement with literature values of around 17–21 % for silicon materials. In general, the backscattering coefficient strongly increases for larger incident angles.

The second major goal was the implementation of the experimental setup in the simulation toolkit GEANT4. In a first step, a fitting procedure was developed to extract the charge collection efficiency parameters from the experimental electron energy spectrum. Given these detector properties, it was then possible to compare the simulated backscattering characteristics to the data. In particular, the energy and angle-dependence of the backscattering coefficient was compared and a good agreement was demonstrated. This result is of high relevance for the final modelling of the full tritium spectrum and its uncertainty estimation.

A detailed uncertainty investigation showed that a small variation in the dead layer thickness parameter has a high impact on the detected electron energy spectra, especially at low initial energies and high incident angles. In future works, the charge collection efficiency model should be validated by a more detailed investigation of different TRISTAN silicon drift detectors with electrons. Furthermore, different charge collection efficiency models should be compared to evaluate the most suitable model for the given doping profiles of

the detectors.

In addition, the uncertainty study showed that the relative positioning of the detectors in the experiment has a high impact on the results. A shift of the backscattering detector of 5 mm in  $x$ -direction can lead to a doubling of the observed number of backscattered electrons per pixel. Therefore, a precise way to measure the experimental geometry after the mounting of the detectors in the vacuum chamber should be developed for future measurements with the developed experimental setup.

In conclusion, by measuring with two detectors and a coincidence analysis, a method has been developed that allowed for the first time to measure the backscattering properties of the TRISTAN detector. The experimental results offer the opportunity to verify already existing as well as future simulations of electron backscattering for the modelling of the TRISTAN detector response. The GEANT4 simulation toolkit was validated to be suitable for backscattering investigations of silicon detectors. As a result, this thesis lays the foundation for an experimentally validated model of backscattering, which is needed for sensitivity studies and the upcoming analysis of the tritium spectra that will be measured with the TRISTAN detector.

# Appendix

## A.1 Geant4 Physics List Comparison

The choice of the GEANT4 physics list influences the spectral shape of the electron energy spectra. In fig. A.1, the energy spectrum of the central pixel of the SOD is shown. For the `G4EmStandardPhysics` (Standard) and `G4EmLowEPPPhysics` (LowE) list, less low-energetic electrons are observed. For the `G4EmLivermorePhysics` (Livermore), Standard and LowE list, the silicon escape peak is not observed. At high energies, only the `G4EmStandardPhysicsSS` (StandardSS) list detects electrons continuously up to the initial electron energy. For the Livermore, `G4EmPenelopePhysics` (Penelope) and LowE list, the spectrum has a gap between the initial electron energy  $E_I$  and  $E_I - 100$  eV. For the Standard list, the spectrum has an even larger gap between  $E_I$  and  $E_I - 1$  keV.

In fig. A.2, the energy spectra of the backscattered electrons are shown. At low energies, only for the StandardSS list electrons down to 0 keV are observed. For the Livermore, Penelope and LowE list, no electrons with energies below 100 eV are recorded. With the Standard list, barely any backscattered electrons with energies below 1 keV are detected. Photons which escaped the silicon bulk of the SOD are only observed for the StandardSS and Penelope list. At high energies, only for the StandardSS, Livermore and Penelope list, a peak at the initial electron energy arising from elastic backscattering/reflection can be seen. In contrast, for the Standard and LowE list, the energy spectrum shows a reduced amount of counts at high energies.

In total, the difference of the physics lists mostly affects energy regions which are not accessible in the experiment. The DAQ system introduces an energy threshold of about 0.8 keV in the SOD and 1 keV in the BSD in the experiment. The electronic noise alters the backscattered electron energy spectrum at high energies and the transition layer effect concerns high the low-energetic side of the main peak in the initial electron energy spectrum. Nevertheless, since only the Penelope and StandardSS physics lists are producing a silicon escape peak in the SOD energy spectrum, one of the two lists should be chosen.

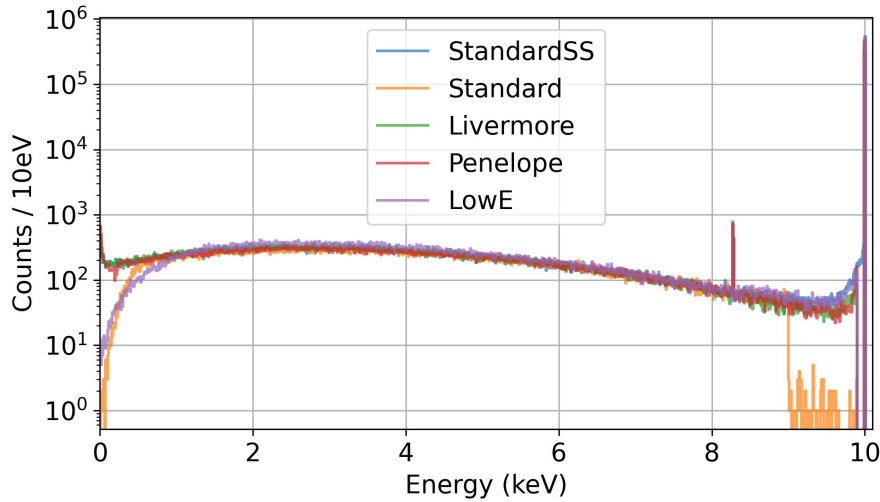


**Figure A.1: Comparison of the Simulated Energy Spectra of the SOD for Different G4 Physics Lists.** The energy of each event is the sum of all energy depositions inside a silicon bulk. No silicon dioxide layer, transition layer model or noise model is applied. The physics lists produce similar results except for energies close to 0 keV and  $E_I$ . The silicon escape peak is not observed for the Livermore, Standard and LowE physics list.

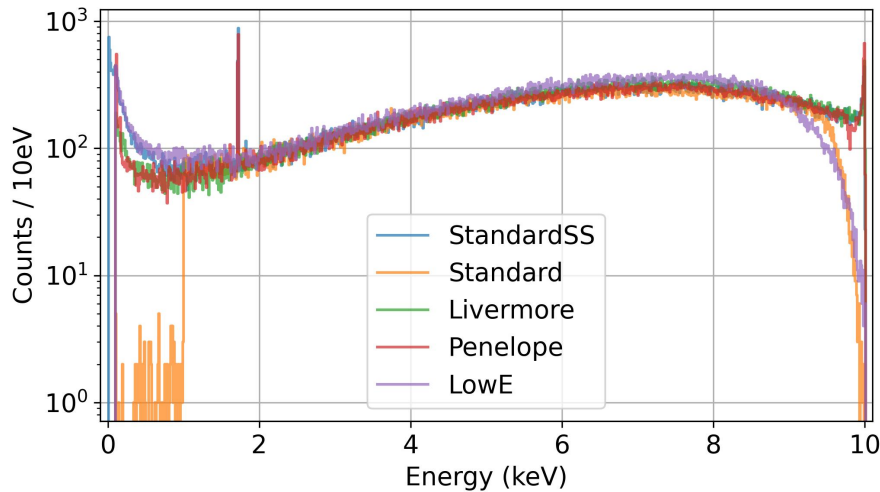


**Figure A.2: Comparison of the Simulated Energy Spectra of Backscattered Electrons for Different G4 Physics Lists.** The energy of backscattered electrons is recorded when they leave the simulated world sphere. The highest variation between the physics lists is observable for energies close to 0 keV and  $E_I$ . A photon peak at 1.74 keV is only visible for the StandardSS and Penelope physics list.

## A.2 Heuristic Detector Model - Additional Fit Results

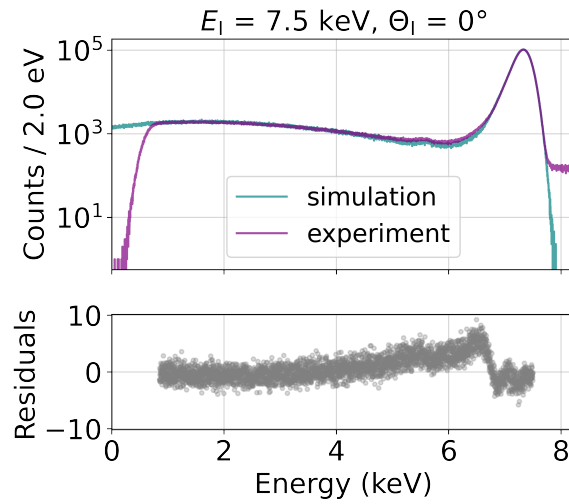


**Figure A.3:** Comparison of Simulated and Measured Energy Spectra of the CC Pixel - Part 2. The simulated fitted energy spectra are compared to the experimental energy spectra for  $E_I = 7.5 \text{ keV}$  and  $\Theta_I = 0^\circ$ . The residuals are calculated for energies between  $E_{\text{SOD,T}}$  and  $E_I + 0.2 \text{ eV}$ .

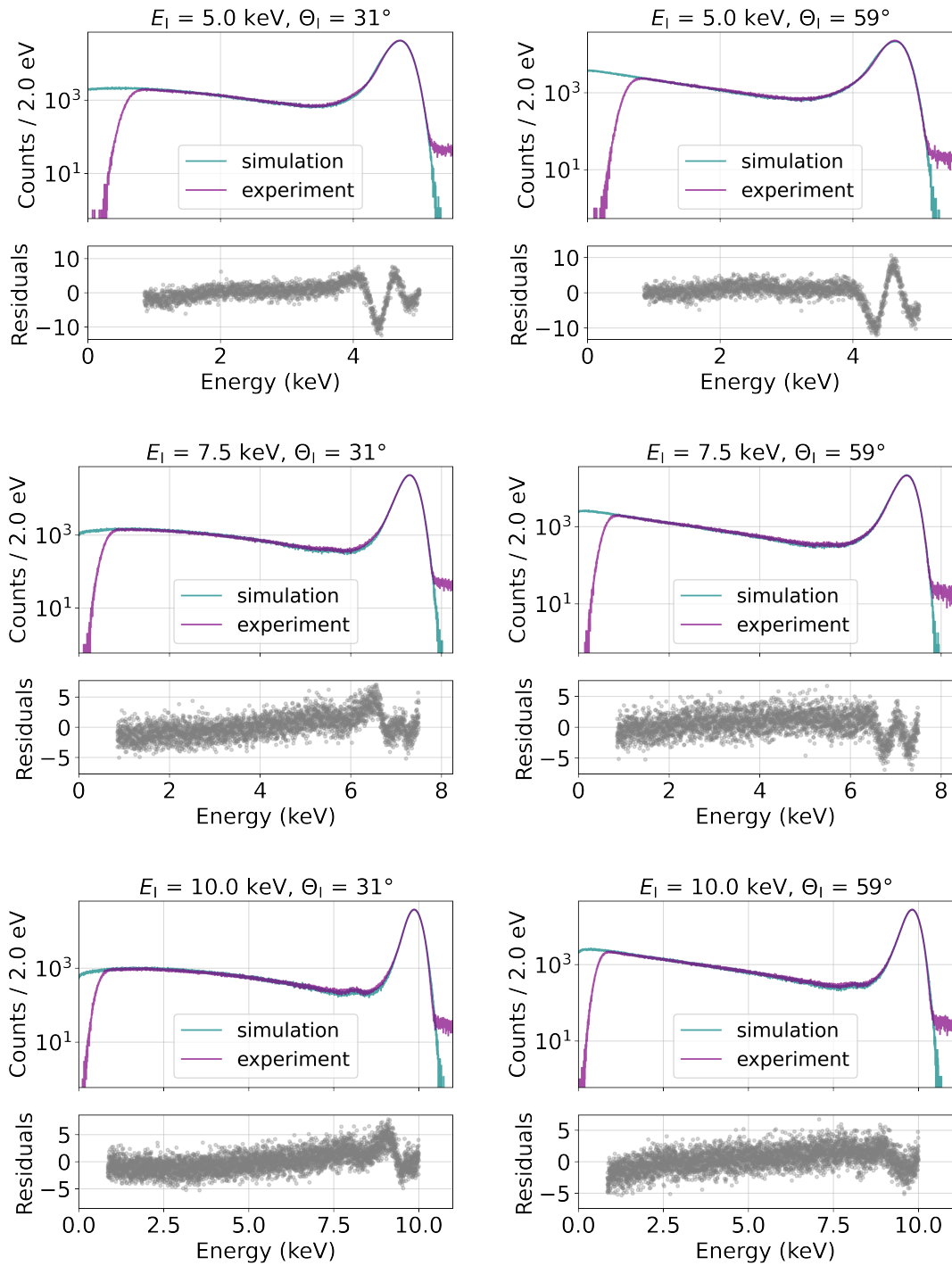


**Figure A.4: Comparison of Simulated and Measured Energy Spectra of the CC Pixel - Part 3.** The simulated fitted energy spectra are compared to the experimental energy spectra for  $\Theta_I = 31^\circ$  and  $\Theta_I = 59^\circ$  for all three initial electron energies. The residuals are calculated for energies between  $E_{\text{SOD,T}}$  and  $E_I + 0.2 \text{ eV}$ .

### A.3 Comparison of Experiment and Simulation - Additional Results

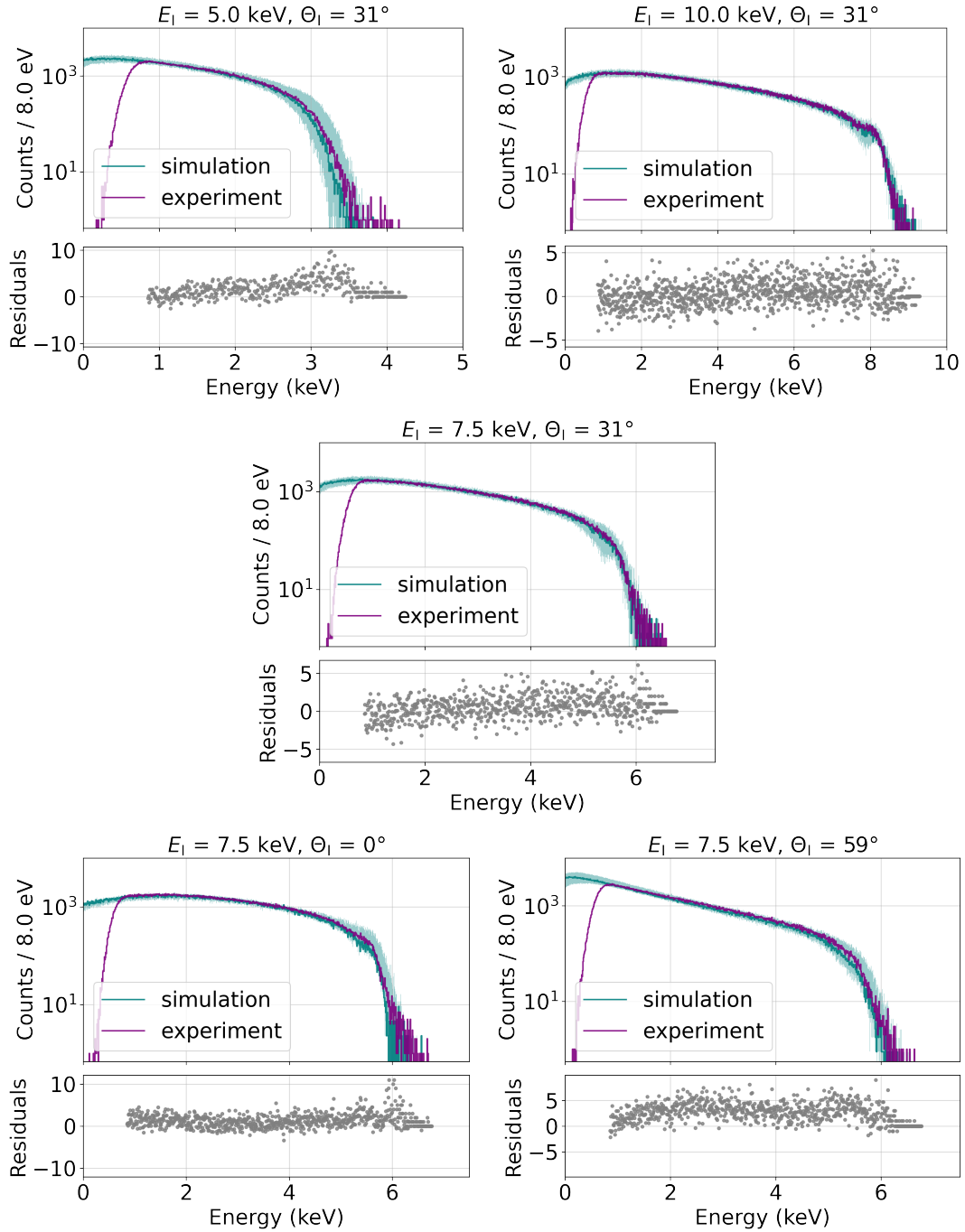


**Figure A.5: Coincidence Electron Energy Spectra of the CC Pixel for Experiment and Simulation - Part 2.** The residuals are calculated for energies between  $E_{\text{SOD,T}}$  and  $E_I - (E_{\text{BSD,T}} - E_{\text{res}})$ . The total uncertainty on the simulated spectra is the minimal and maximal value per bin extracted from approach one of the uncertainty estimation (sec. 7.1).

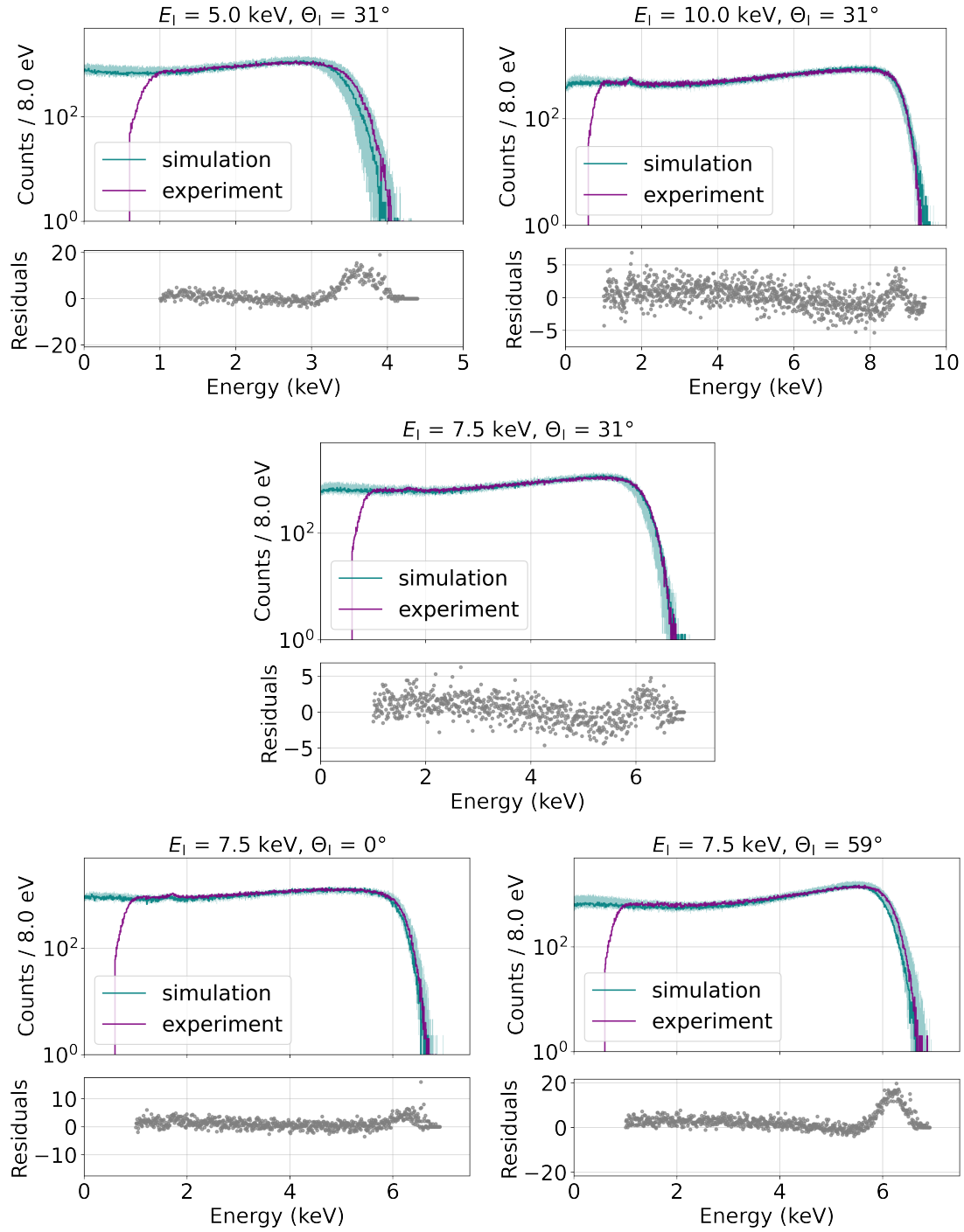


**Figure A.6: Coincidence Electron Energy Spectra of the BSD for Experiment and Simulation - Part 2.** The residuals are calculated for energies between  $E_{\text{BSD},T}$  and  $E_I - (E_{\text{SOD},T} - E_{\text{res}})$ . The total uncertainty on the simulated spectra is the minimal and maximal value per bin extracted from approach one of the uncertainty estimation (sec. 7.1).

# List of Figures

2.1	Standard Model of Particle Physics . . . . .	4
2.2	Fermion Mass Ordering . . . . .	7
2.3	Neutrino Mass Signature in the Tritium $\beta$ -Decay Spectrum . . . . .	8
2.4	Sterile Neutrino Two-Body Decay. . . . .	10
3.1	Schematic of the KATRIN Experiment . . . . .	11
3.2	MAC-E Filter Principle . . . . .	13
4.1	Sterile Neutrino Signature in the Tritium $\beta$ -Decay Spectrum . . . . .	15
4.2	TRISTAN Detector Design . . . . .	17
4.3	SDD Working Scheme . . . . .	18
4.4	Response of the TRISTAN Detector to Electrons . . . . .	19
4.5	Definition of the Incident Angle $\Theta_I$ . . . . .	22
4.6	Backscattering and Backreflection in the KATRIN Beamline . . . . .	24
5.1	In-Vacuum Setup . . . . .	26
5.2	Electron Gun Design . . . . .	27
5.3	PCB Board with the Seven-Pixel Prototype Detector . . . . .	28
5.4	166-Pixel Detector Module . . . . .	29
5.5	Readout-Chain for One Pixel . . . . .	30
5.6	Waveform Samples for First and Second Stage Amplification . . . . .	31
5.7	Trapezoidal Filter Principle . . . . .	32
5.8	SOD and BSD Positioning for Different Incident Angles . . . . .	33
5.9	Pixel Nomenclature of the SOD and BSD . . . . .	33
5.10	Fe-55 Source Positioning . . . . .	35
5.11	Fe-55 Spectra for One Exemplary Pixel per Detector . . . . .	35
5.12	Energy Resolution of Both Detectors at 5.9 keV . . . . .	36
5.13	Amount of Coincidence Events in the SOD as a Function of the Time Window . . . . .	37
5.14	Spectral Effect of Charge Sharing . . . . .	38
5.15	Energy Thresholds for Pileup Considerations . . . . .	39

5.16	Relative Number of Counts in the SOD for Different Incident Angles at $E_I = 10$ keV . . . . .	40
5.17	Amount of Backscattering Coincidence Events as a Function of the Time Window. . . . .	41
5.18	Electron Energy Spectra Comparing Different Measurement Settings . . . . .	43
5.19	Definition of the Backscattering Angles . . . . .	44
5.20	Backscattering Angles for Each Pixel of the BSD . . . . .	44
5.21	Number of Backscattered Electrons in the BSD for Different Measurement Settings . . . . .	45
5.22	Experimental Backscattering Coefficient as Function of the Incident Angle . . . . .	46
5.23	2D-Histogram for Identified Backscattering Coincidence Events . . . . .	47
5.24	Electron Energy Spectra of the CC Pixel Comparing All and Coincidence Events . . . . .	48
5.25	Backscattering Detection Efficiency as a Function of the Incident Angle . . . . .	49
5.26	Backscattered Electron Energy Spectra Comparing All Events and Coincidence Events . . . . .	50
5.27	Relative Number of Counts in the CC Pixel as a Function of the Incident Angle at $E_I = 10$ keV . . . . .	50
5.28	BSD Pixel Grouping by $\Theta_{BS}$ . . . . .	51
5.29	Backscattered Electron Energy Spectra for Pixel Group 0 and 5 Comparing Different Measurement Settings . . . . .	52
5.30	Number of Backscattered Electrons with Coincidence with the CC Pixel and Difference to $N_{BSD}$ for Different $\Theta_I$ . . . . .	54
5.31	Number of Backscattered Electrons with Coincidence with the CC Pixel and Difference to $N_{BSD}$ for Different $E_I$ . . . . .	55
5.32	Coincidence Backscattering Coefficient as a Function of the Incident Angle . . . . .	56
6.1	Simulation Setup . . . . .	60
6.2	Detector Segmentation for a CCE Model Fit . . . . .	64
6.3	Mean Charge Collection Efficiency . . . . .	66
6.4	Fit Parameter Results . . . . .	67
6.5	Comparison of Simulated and Measured Energy Spectra of the CC Pixel . . . . .	68
6.6	Fit Performance in Terms of $\chi_{red}^2$ . . . . .	68
6.7	Simulated Energy Spectra of the CC Pixel . . . . .	70
6.8	Simulated Energy Spectra of the Backscattered Electrons . . . . .	71
6.9	Number of Simulated Backscattered Electrons per Solid Angle . . . . .	72
6.10	Simulated Backscattering Coefficients as a Function of the Incident Angle . . . . .	74

7.1	Illustration of the Geometrical Uncertainties . . . . .	78
7.2	Coincidence Electron Energy Spectra of the CC Pixel for Experiment and Simulation . . . . .	80
7.3	Coincidence Electron Energy Spectra of the BSD for Experiment and Simulation . . . . .	81
7.4	Impact on the Backscattered Electron Energy Spectrum for Variations of the Most Important Parameters . . . . .	82
7.5	Difference in $N_{\text{coinc}}$ Per Pixel in the BSD Between Experiment and Simulation	83
7.6	Comparison of $N_{\text{coinc}}$ in the BSD as a Function of the Pixel Number . . . . .	84
7.7	Difference of the Angular Distribution for Variations of the Most Important Parameters . . . . .	85
7.8	Comparison of the Backscattering Coefficients as a Function of the Incident Angle . . . . .	87
A.1	Comparison of the Simulated Energy Spectra of the SOD for Different G4 Physics Lists . . . . .	94
A.2	Comparison of the Simulated Energy Spectra of Backscattered Electrons for Different G4 Physics Lists . . . . .	94
A.3	Comparison of Simulated and Measured Energy Spectra of the CC Pixel - Part 2 . . . . .	95
A.4	Comparison of Simulated and Measured Energy Spectra of the CC Pixel - Part 3 . . . . .	96
A.5	Coincidence Electron Energy Spectra of the CC Pixel for Experiment and Simulation - Part 2 . . . . .	97
A.6	Coincidence Electron Energy Spectra of the BSD for Experiment and Simulation - Part 2 . . . . .	98



# List of Tables

5.1	Overview of the Measurement Settings . . . . .	32
5.2	Pileup Thresholds for the Chosen Initial Electron Energies . . . . .	39
6.1	Fit Parameter Start Values and Bounds . . . . .	65
7.1	Uncertainties on Selected Parameters . . . . .	78
7.2	Relative Deviation of the Backscattering Coefficients for Variation of one Parameter . . . . .	88



# Bibliography

- [1] G. Ecker. “James Chadwick: ahead of his time”. In: *History and Philosophy of Physics* (July 2020). DOI: 10.48550/arXiv.2007.06926.
- [2] W. Pauli. *Pauli letter collection: letter to Lise Meitner*. Dec. 1930. URL: <http://cds.cern.ch/record/83282>.
- [3] C.L. Cowan Jr. et al. “Detection of the Free Neutrino: a Confirmation”. In: *Science* 124.3212 (July 1956), pp. 103–104. DOI: 10.1126/science.124.3212.103.
- [4] G. Danby et al. “Observation of High-Energy Neutrino Reactions and the Existence of Two Kinds of Neutrinos”. In: *Phys. Rev. Lett.* 9.36 (July 1962). DOI: 10.1103/PhysRevLett.9.36.
- [5] S.N. Gninenko; D.S. Gorbunov and M.E. Shaposhnikov. “Search for GeV-Scale Sterile Neutrinos Responsible for Active Neutrino Oscillations and Baryon Asymmetry of the Universe”. In: *Advances in High Energy Physics* 2012.718259 (Dec. 2012). DOI: 10.1155/2012/718259.
- [6] DONUT Collaboration; K. Kodama et al. “Observation of tau neutrino interactions”. In: *Phys. Lett. B* 504 (Apr. 2001). DOI: 10.1016/S0370-2693(01)00307-0.
- [7] The ALEPH Collaboration et al. “Precision electroweak measurements on the Z resonance”. In: *Physics Reports* 427 (May 2006). DOI: 10.1016/j.physrep.2005.12.006.
- [8] M. Goldhaber; L. Grodzins and A. W. Sunyar. “Helicity of Neutrinos”. In: *Phys. Rev.* 109.1015 (Feb. 1958). DOI: 10.1103/PhysRev.109.1015.
- [9] B.T. Cleveland et al. “Measurement of the Solar Electron Neutrino Flux with the Homestake Chlorine Detector”. In: *The Astrophysical Journal* 496.1 (Apr. 1998). DOI: 10.1086/305343.
- [10] M. Cribier et al. “Results of the whole GALLEX experiment”. In: *Nuclear Physics B - Proceedings Supplements* 70 (Jan. 1999). DOI: 10.1016/S0920-5632(98)00438-1.
- [11] V.N. Gavrin et al. “Measurement of the solar neutrino capture rate in SAGE”. In: *Nuclear Physics B - Proceedings Supplements* 118 (Apr. 2003). DOI: 10.1016/S0920-5632(03)01302-1.
- [12] C. Arpesella et al. (Borexino Collaboration). “Direct Measurement of the  $^7\text{Be}$  Solar Neutrino Flux with 192 Days of Borexino Data”. In: *Phys. Rev. Lett.* 101.091302 (Aug. 2008). DOI: 10.1103/PhysRevLett.101.091302.
- [13] N. Barros et al. “Final results from SNO”. In: *Nuclear Physics B - Proceedings Supplements* 237-238 (May 2013). DOI: 10.1016/j.nuclphysbps.2013.04.069.

- [14] C. Giunti. “Theory of Neutrino Oscillation”. In: *Particle Physics in Laboratory, Space and Universe* (2005), pp. 35–44. DOI: 10.1142/9789812702074\_0005.
- [15] J.K. Ahn et al. (RENO Collaboration). “Observation of Reactor Electron Antineutrinos Disappearance in the RENO Experiment”. In: *Phys. Rev. Lett.* 108.191802 (May 2012). DOI: 10.1103/PhysRevLett.108.191802.
- [16] F.P. An et al. “Observation of Electron-Antineutrino Disappearance at Daya Bay”. In: *Phys. Rev. Lett.* 108.171803 (Apr. 2012). DOI: 10.1103/PhysRevLett.108.171803.
- [17] K. Abe et al. (T2K Collaboration). “Observation of Electron Neutrino Appearance in a Muon Neutrino Beam”. In: *Phys. Rev. Lett.* 112.061802 (Feb. 2014). DOI: 10.1103/PhysRevLett.112.061802.
- [18] P. Adamson et al. (MINOS Collaboration). “Measurement of Neutrino and Antineutrino Oscillations Using Beam and Atmospheric Data in MINOS”. In: *Phys. Rev. Lett.* 110.251801 (June 2013). DOI: 10.1103/PhysRevLett.110.251801.
- [19] M. Tanabashi et al. (Particle Data Group). “Review of Particle Physics”. In: *Phys. Rev. D* 98.030001 (Aug. 2018). DOI: 10.1103/PhysRevD.98.030001.
- [20] F.A. Edzards. “Characterization of Point Contact Germanium Detectors and Development of Signal Readout Electronics for LEGEND”. PhD Thesis. Technical University of Munich, 2021.
- [21] N. Aghanim et al. (Planck Collaboration). “Planck 2018 results. VI. Cosmological parameters”. In: *Astronomy and Astrophysics* 641 (July 2018). DOI: 10.48550/arXiv.1807.06209.
- [22] S. Abe et al. (KamLAND-Zen Collaboration). “Search for the Majorana Nature of Neutrinos in the Inverted Mass Ordering Region with KamLAND-Zen”. In: *High Energy Physics - Experiment* (Mar. 2022). DOI: 10.48550/arXiv.2203.02139.
- [23] J. Engel and J. Menéndez. “Status and future of nuclear matrix elements for neutrinoless double-beta decay: a review”. In: *Rep. Prog. Phys.* 80.046301 (Mar. 2017). DOI: 10.1088/1361-6633/aa5bc5.
- [24] The KATRIN Collaboration. “Direct neutrino-mass measurement with sub-electronvolt sensitivity”. In: *Nature Physics* 18 (Feb. 2022), pp. 160–166. DOI: 10.1038/s41567-021-01463-1.
- [25] A. Ashtari Esfahani et al. (Project 8 Collaboration). “The Project 8 Neutrino Mass Experiment”. In: *Nuclear Experiment* (Mar. 2022). DOI: 10.48550/arXiv.2203.07349.
- [26] R. Adhikari et al. “A White Paper on keV Sterile Neutrino Dark Matter”. In: *Journal of Cosmology and Astroparticle Physics* 2017 (Jan. 2017). DOI: 10.1088/1475-7516/2017/01/025.
- [27] L. Schlüter. “Neutrino-Mass Analysis with sub-eV Sensitivity and Search for Light Sterile Neutrinos with the KATRIN Experiment”. PhD Thesis. Technical University of Munich, 2022.

- [28] R.N. Mohapatra and G. Senjanović. “Neutrino Mass and Spontaneous Parity Non-conservation”. In: *Phys. Rev. Lett.* 44.912 (Apr. 1980). DOI: 10.1103/PhysRevLett.44.912.
- [29] V. Domcke et al. “MeV-scale Seesaw and Leptogenesis”. In: *High Energy Physics* (Apr. 2021). DOI: 10.48550/arXiv.2009.11678.
- [30] A. Boyarsky; D. Iakubovskiy and O. Ruchayskiy. “Next decade of sterile neutrino studies”. In: *Physics of the Dark Universe* 1 (Nov. 2012). DOI: 10.1016/j.dark.2012.11.001.
- [31] J.P. Conlon et al. “Consistency of Hitomi, XMM-Newton and Chandra 3.5 keV data from Perseus”. In: *Phys. Rev. D* 96 (123009 Dec. 2017). DOI: 10.1103/PhysRevD.96.123009.
- [32] N. Cappelluti et al. “Searching for the 3.5 keV Line in the Deep Fields with Chandra: The 10 Ms Observations”. In: *The Astrophysical Journal* 854.179 (Feb. 2018). DOI: 10.3847/1538-4357/aaa68.
- [33] E. Bulbul et al. “Searching for the 3.5 keV Line in the Stacked Suzaku Observations of Galaxy Clusters”. In: *The Astrophysical Journal* 831.55 (Oct. 2016). DOI: 10.3847/0004-637X/831/1/55.
- [34] S. Bhargava et al. “The XMM Cluster Survey: new evidence for the 3.5 keV feature in clusters is inconsistent with a dark matter origin”. In: *Monthly Notices of the Royal Astronomical Society* 497 (Sept. 2020). DOI: 10.1093/mnras/staa1829.
- [35] S. Mertens et al. “A novel detector system for KATRIN to search for keV-scale sterile neutrinos”. In: *J. Phys. G: Nucl. Part. Phys.* 46.065203 (May 2019). DOI: 10.1088/1361-6471/ab12fe.
- [36] J.N. Abdurashitov et al. “Measurement of the solar neutrino capture rate with gallium metal. III. Results for the 2002–2007 data-taking period”. In: *Phys. Rev. C* 80 (015807 July 2009). DOI: 10.1103/PhysRevC.80.015807.
- [37] S. Gariazzo et al. “Light sterile neutrinos”. In: *J. Phys. G: Nucl. Part. Phys.* 43 (033001 Jan. 2016). DOI: 10.1088/0954-3899/43/3/033001.
- [38] G. Mention et al. “Reactor antineutrino anomaly”. In: *Phys. Rev. D* 83.073006 (Apr. 2011). DOI: 10.1103/PhysRevD.83.073006.
- [39] V. Kopeikin; M. Skorokhvatov and O. Titov. “Reevaluating reactor antineutrino spectra with new measurements of the ratio between  $^{235}\text{U}$  and  $^{239}\text{Pu}$   $\beta$  spectra”. In: *Phys. Rev. D* 104.L071301 (Oct. 2021). DOI: 10.1103/PhysRevD.104.L071301.
- [40] Ch. Kraus et al. “Final Results from phase II of the Mainz Neutrino Mass Search in Tritium  $\beta$  Decay”. In: *The European Physical Journal C - Particles and Fields* 40 (Apr. 2005). DOI: 10.1140/epjc/s2005-02139-7.
- [41] V.N. Aseev et al. “Upper limit on the electron antineutrino mass from the Troitsk experiment”. In: *Phys. Rev. D* 84.112003 (Dec. 2011). DOI: 10.1103/PhysRevD.84.112003.
- [42] KATRIN Collaboration. *Katrin design report 2004*. Technical report. Forschungszentrum Karlsruhe, 2005. URL: <http://bibliothek.fzk.de/zb/berichte/FZKA7090.pdf>.

- [43] M. Aker et al. “First operation of the KATRIN experiment with tritium”. In: *The European Physical Journal C* 80.264 (Mar. 2020). DOI: 10.1140/epjc/s10052-020-7718-z.
- [44] M. Aker et al. (KATRIN Collaboration). “Improved Upper Limit on the Neutrino Mass from a Direct Kinematic Method by KATRIN”. In: *Phys. Rev. Lett.* 123.221802 (Nov. 2019). DOI: 10.1103/PhysRevLett.123.221802.
- [45] K. Hugenberg. “Design of the electrode system of the KATRIN main spectrometer”. Diploma Thesis. WWU Münster, 2008. URL: [https://www.uni-muenster.de/Physik.KP/AGWeinheimer/theses/Diplom\\_%20Karen\\_Hugenberg.pdf](https://www.uni-muenster.de/Physik.KP/AGWeinheimer/theses/Diplom_%20Karen_Hugenberg.pdf).
- [46] F.M. Fränkle et al. “Penning discharge in the KATRIN pre-spectrometer”. In: *Journal of Instrumentation* 9.P07028 (July 2014). DOI: 10.1088/1748-0221/9/07/P07028.
- [47] J.F. Amsbaugh et al. “Focal-plane detector system for the KATRIN experiment”. In: *Nucl. Inst. Meth. A* 778 (Apr. 2015). DOI: 10.1016/j.nima.2014.12.116.
- [48] M. Aker et al. (KATRIN collaboration). “Search for keV-scale Sterile Neutrinos with first KATRIN Data”. In: *Nuclear Experiment* (July 2022). DOI: 10.48550/arXiv.2207.06337.
- [49] T.B. Brunst. “First generation prototype detectors for the TRISTAN project”. PhD Thesis. Technical University of Munich, 2020.
- [50] TRISTAN group. *Conceptual Design Report: KATRIN with TRISTAN modules*. URL: [https://www.katrin.kit.edu/downloads/TRISTAN\\_\\_Technical\\_Design\\_Report%20\(10\).pdf](https://www.katrin.kit.edu/downloads/TRISTAN__Technical_Design_Report%20(10).pdf).
- [51] M. Gugiatti. “Development of a Large-matrix SDD-based Radiation Detector for Beta-decay Spectroscopy in Neutrino Physics”. PhD Thesis. Politecnico Milano, 2022.
- [52] K. Dolde. “Detector and read-out development to search for sterile neutrinos with KATRIN”. Master’s Thesis. Karlsruhe Institute of Technology, 2016.
- [53] J. Kholdkov. “Measurement of ADC Nonlinearities and Development of a Bias Board for the TRISTAN Detector”. Master’s Thesis. Technical University of Munich, 2021.
- [54] M. Korzeczek. “Sterile neutrino search with KATRIN - modeling and design-criteria of a novel detector system”. PhD Thesis. Karlsruhe Institute of Technology, 2020. URL: <https://publikationen.bibliothek.kit.edu/1000120634>.
- [55] D.B. Siegmann. “Characterization of the first TRISTAN 166-pixel detector module”. In preparation. PhD Thesis. Technical University of Munich, 2023.
- [56] C. Bruch. “Characterisation of a 166-Pixel TRISTAN Detector Module in the KATRIN Monitor Spectrometer”. Master’s Thesis. Technical University of Munich, 2023.
- [57] D.B. Siegmann. “Investigation of the Detector Response to Electrons of the TRISTAN Prototype Detectors”. Master’s Thesis. Technical University of Munich, 2019.
- [58] K. Urban. “Application of a TRISTAN Silicon Drift Detector as Forward Beam Monitor in KATRIN”. Master’s Thesis. Technical University of Munich, 2019.

- [59] M.N. Mazziotta. “Electron–hole pair creation energy and Fano factor temperature dependence in silicon”. In: *Nucl. Instrum. Meth. A* 584 (Jan. 2008). DOI: 10.1016/j.nima.2007.10.043.
- [60] P. Lechner et al. “Silicon drift detectors for high count rate X-ray spectroscopy at room temperature”. In: *Nucl. Instrum. Meth. A* 458 (Feb. 2001). DOI: 10.1016/S0168-9002(00)00872-X.
- [61] M. Gugiatti et. al. “Characterization of a Silicon Drift Detector for High-Resolution Electron Spectroscopy”. In: *Nucl. Instrum. Meth. A* 979.164474 (Nov. 2020). DOI: 10.1016/j.nima.2020.164474.
- [62] Oxford Instruments. The Business of Science., ed. *Silicon Drift Detectors Explained*. 2012. URL: [https://www.exvil.lt/wp-content/uploads/2012/04/SDD\\_Explained.pdf](https://www.exvil.lt/wp-content/uploads/2012/04/SDD_Explained.pdf).
- [63] A. Nava et al. “A Geant4-based model for the TRISTAN detector”. In: *Journal of Physics: Conference Series* 2156.012177 (2021). DOI: 110.1088/1742-6596/2156/1/012177.
- [64] S. Mertens et al. “Characterization of silicon drift detectors with electrons for the TRISTAN project”. In: *J. Phys. G: Nucl. Part. Phys.* 48.015008 (Dec. 2020). DOI: 10.1088/1361-6471/abc2dc.
- [65] A. Thompson et al. *X-Ray Data Booklet. Center for X-ray Optics and Advanced Light Source*. 2009. URL: <https://xdb.lbl.gov/>.
- [66] C. Forstner. “Pulse Shape Analysis with the TRISTAN Silicon Drift Detector”. Bachelor’s Thesis. Technical University of Munich, 2020.
- [67] A. Nava. *Report presented at the TRISTAN Workshop 2022 at the KIT*.
- [68] D.C. Joy. “A database on electron-solid interactions”. In: *Scanning - The journal of scanning microscopies* 17 (Oct. 1995). DOI: 10.1002/sca.4950170501.
- [69] H. Drescher; R. Reimer and H. Seidel. “Rückstreuoeffizient und Sekundarelektro-nen-Ausbeute von 10-100 keV-Elektronen und Beziehungen zur Raster-Elektronen- Mikroskopie”. In: *Zeitschrift für Angewandte Physik* 29 (1970), p. 331.
- [70] B. Lesiak J. Zemek; P. Jiricek and A. Jablonski. “Elastic electron backscattering from silicon surfaces: effect of charge-carrier concentration”. In: *Surface and Interface Analysis* 36 (Aug. 2004). DOI: 10.1002/sia.1770.
- [71] P. Renschler. “KESS - A new Monte Carlo simulation code for low-energy electron interactions in silicon detectors”. PhD Thesis. Karlsruhe Institute of Technology, 2011.
- [72] H.B. Michaelson. “The work function of the elements and its periodicity”. In: *Journal of Applied Physics* 48 (1977). DOI: 10.1063/1.323539.
- [73] M. Descher. “High rate systematic effects for keV sterile neutrino searches at KA-TRIN”. Master’s Thesis. Institute of Experimental Particle Physics, 2019.

- [74] P. Trigilio et al. “ETTORE: a 12-Channel Front-End ASIC for SDDs with Integrated JFET”. In: *IEEE Nuclear Science Symposium and Medical Imaging Conference Proceedings (NSS/MIC), Sydney, NSW, Australia* (2018). DOI: 10.1109/NSSMIC.2018.8824675.
- [75] CAEN - Electronic Instrumentation. *CoMPASS User Manual UM5960 rev.18 - Multiparametric DAQ Software for Physics Applications*. Sept. 2022. URL: <https://seltokphotonics.com/upload/iblock/28b/28bd53047bcb1dc23f8fe78548ec7021.pdf>.
- [76] D. Spreng. “Energy Calibration of the TRISTAN Silicon Drift Detectors”. Bachelor’s Thesis. Technical University of Munich, 2020.
- [77] G. Audi et al. “The Nubase evaluation of nuclear and decay properties”. In: *Nucl. Phys. A* 729 (Dec. 2003). DOI: 10.1016/j.nuclphysa.2003.11.001.
- [78] S.Y.F. Chu; L.P. Ekström and R.B. Firestone. *The Lund/LBNL Nuclear Data Search*. Feb. 1999. URL: <http://nucleardata.nuclear.lu.se/toi/index.asp>.
- [79] C. Forstner. “Characterization of a TRISTAN Silicon Drift Detector Array with a Laser System”. In preparation. Master’s Thesis. Technical University of Munich, 2023.
- [80] *Geant4 - A simulation toolkit, Guide for Physics Lists*. URL: <https://geant4-userdoc.web.cern.ch/UsersGuides/PhysicsListGuide/html/index.html>.